INAUGURAL – DISSERTATION

zur
Erlangung der Doktorwürde

der
Naturwissenschaftlich-Mathematischen
Gesamtfakultät

der
Ruprecht-Karls-Universität
Heidelberg

vorgelegt von

Dipl.–Phys. Christopher Borgmann
aus Münster

Tag der mündlichen Prüfung: 7. November 2012

Mass Measurements of Exotic Ions in the Heavy Mass Region for Nuclear Structure Studies at ISOLTRAP

Gutachter:	Prof. Dr. Klaus Blaum
	PD Dr. Yuri Litvinov

Zusammenfassung

Die Masse charakterisiert jedes Nuklid wie ein Fingerabdruck, da sie die Summe aller Wechselwirkungen innerhalb des Kerns repräsentiert. Der Vergleich von experimentellen Daten mit theoretischen Berechnungen liefert daher wichtige Hinweise, wie gut die Wechselwirkung der Nukleonen bereits verstanden ist. Mit Hilfe von Bindungsenergiedifferenzen wie der Zwei-Neutronen-Separationsenergie ($S_{2\mathrm{n}}$) können wertvolle Informationen über die Kernstruktur abgeleitet werden.

Die vorliegende Arbeit trägt zu der oben erwähnten Diskussion bei, indem neue hochpräzise Massenmessungen im schweren Massenbereich zur Verfügung gestellt werden. Aufgrund der großen Anzahl an Nukleonen ist eine theoretische Beschreibung hier besonders kompliziert. Die Messungen wurden am Penning-Fallen-Massenspektrometer Isoltrap durchgeführt, welches sich am Isotopenseparator Isolde am Cern befindet. Zur Massenbestimmung wurde die resonante Anregung der Zyklotronfrequenz von in einer Penning-Falle gespeicherten Ionen über den Flugzeiteffekt nachgewiesen.

Während die neuen Massendaten für $^{122-124}$Ag den bereits bekannten Linienverlauf der $S_{2\mathrm{n}}$ Energien in dieser Region fortsetzen und die neuen Massendaten für ^{207,208}Fr ihn präzisieren, wurde mit Hilfe der neuen Massenwerte für $^{184,186,190,193-195}$Tl ein neuer interessanter gerade-ungerade Effekt beobachtet. Der Vergleich der experimentellen Daten mit theoretischen Modellen zeigt weiterhin starke Probleme der theoretischen Berechnungen, den vorhandenen Paarungseffekt korrekt wiederzugeben. Diese Phänomene sind speziell für die Diskussion der Koexistenz verschiedener Kernformen in der Region um das doppelt-magische ^{208}Pb von Interesse.

Abstract

The mass is a unique fingerprint of each nucleus as it reflects the sum of all interactions within it. Comparing experimental mass values with theoretical calculations provides an important benchmark of how well the role of these interactions is already understood. By investigating differences of experimental binding energies, such as two-neutron separation energies ($S_{2\mathrm{n}}$), valuable indications for nuclear-structure studies are provided.

The present thesis contributes to these studies providing new high-precision mass measurements especially in the heavy-mass region. Here, nuclear theory is heavily challenged due to the large number of nucleons. The data have been obtained at the Penning-trap mass spectrometer Isoltrap located at the radioactive-ion-beam facility Isolde at Cern. For the determination of the masses, the time-of-flight ion-cyclotron-resonance technique has been applied.

While the new mass data for $^{122-124}$Ag continue existing trends in the $S_{2\mathrm{n}}$ energies, the new mass values for ^{207,208}Fr render them more precisely. In the case of the mass values for $^{184,186,190,193-195}$Tl a new interesting odd-even effect has been revealed. The comparison of the measured mass values with theoretical models furthermore demonstrates significant problems in reproducing the strength of the pairing correctly. This is of special interest for the discussion about shape coexistence in the region around the doubly-magic ^{208}Pb.

Contents

List of Figures

List of Tables

List of Abbreviations

GUI	Graphical User Interface
AME	Atomic Mass Evaluation
CMF	Computer Management Framework, a management tool for Windows computers at CERN
FPGA	Field Programmable Gate Array, an integrated circuit which can be configured after manufacturing
GPIB	General Purpose Interface Bus, a communication bus specification
GPS	General Purpose Separator, a mass separator at ISOLDE
HRS	High Resolution Separator, a mass separator at ISOLDE
OPC	Object Linking and Embedding for Process Control, an industrial communication standard
PCI	Peripheral Component Interconnect, a computer bus
PROFIBUS	Process Field Bus, a field bus standard
PSB	Proton Synchrotron Booster, an accelerator at CERN
RILIS	Resonant Ionization Laser Ion Source, an ion source used at ISOLDE
SVN	Subversion, a versioning and revision control system
TCP/IP	Transmission Control Protocol / Internet Protocol, a basic communication protocol for networks
USB	Universal Serial Bus, a communication bus specification
VADIS	Versatile Arc Discharge Ion Source, an ion source used at ISOLDE
VME	Versa Module Eurocard, a computer bus standard
XML	Extensible Markup Language, a markup language for a document to be read by both, humans and machines
Ethernet	A group of network technologies for a local area network
RS232	A communication interface specification
RS485	A communication bus specification

1 Introduction

What is the world made of? How did it come into existence? Humans have been coping with these questions since the beginning of mankind: Already the prehistoric cave paintings show us that humans were wondering about the world around them. Later on, the Greeks claimed that the world is composed of four elements: water, earth, wind and fire. Democritus subsequently replaced this idea by the concept of atoms (from the Greek word *atomos* meaning “impartible”) as the fundamental constituents of matter. However, after a long period, the hints for a substructure of the atoms got more solid. Finally, at the beginning of the 20th century, RUTHERFORD and his colleagues finally demonstrated that atoms were almost empty by scattering α particles from a gold foil [1, 2], which led to the conclusion that most of the mass of the atom is concentrated in the center: The nucleus was discovered!

Nevertheless, the more detailed character of the nucleus was still unclear. RUTHERFORD assumed in his calculations the nucleus to be point-like, which served as a first approximation. A more elaborate picture of the nuclear structure evolved after the discovery of the neutron by CHADWICK in 1932 [3] and its identification as one constituent of the nucleus. Two further important steps forward in the explanation of the inner structure of the nucleus were made by WEIZSÄCKER: In 1935, he published the first mass formula based on the assumption that the nucleus is composed of protons and neutrons [4] and in 1936 he characterized isomeric states (long-lived excited states of the nucleus) for the first time [5]. However, there was another step missing to discover the next challenge: Comparing the properties of different nuclei all over the chart of nuclides, characteristic deviations for nuclei with certain numbers (thereafter called “magic numbers”) of nucleons were exposed [6]: They turned out to be extraordinary strongly bound, an observation which could not be explained in the framework of the existing knowledge. This puzzling mystery was finally unraveled in 1949 when GOEPPERT-MEYER and JENSEN successfully transferred a *shell model* analogous to the periodic chart of elements in atomic physics to the nucleus [7, 8]. With this important step, the basic description of the nucleus was achieved.

As usual, it is the little things that cause big problems and thus, as of today with 60 years having passed, there is still a lack of a solid theory with predictive power, especially for heavier nuclei. Two main problems can be identified: First, nuclear theory is facing severe mathematical problems, as in most cases perturbation theory cannot be applied due to the nature of the interaction within the nucleus. In addition, for the use of statistical methods the number of nucleons is usually too small [10]. Second, it is known from experiments that properties of nuclei change a lot going not only from light to heavy ones, but also outwards from the line of stability in the nuclear chart (see Fig. 1.1). On the one hand, this makes extrapolations and predictions quite difficult for theory. On the other hand, to look on the bright side, it provides the chance to deduce new information from this change of properties. To allow this deduction, experimental

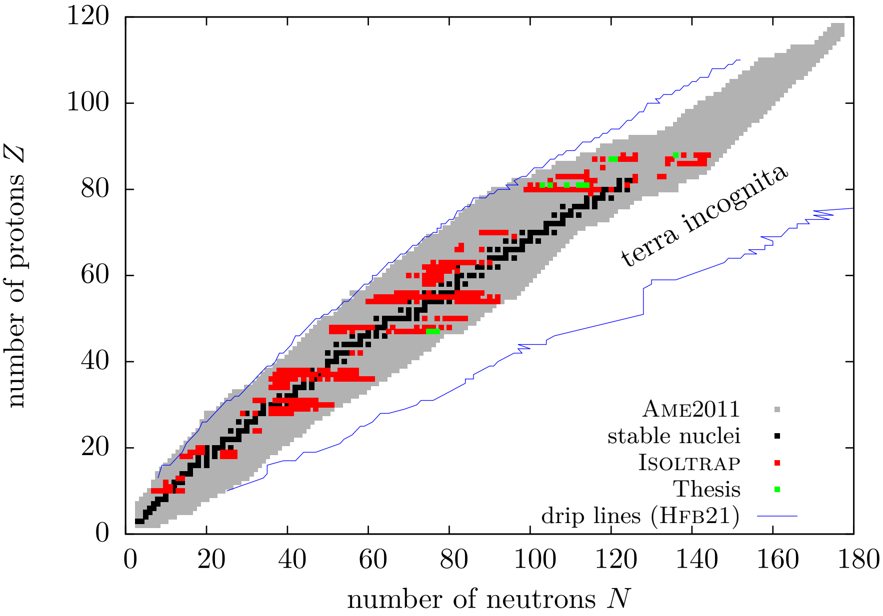

Figure 1.1: *(Color) The* Nuclear Chart *based on nuclei which are included in the* Atomic Mass Evaluation 2011 *(*AME2011*) [9]. Stable nuclides are indicated in black, nuclides, whose masses haven been measured at* ISOLTRAP *in red and nuclides, whose masses have been measured in the context of this thesis in green. The blue lines denote the calculated limit of bound nuclei and are referred to as* drip lines.

data on nuclei away from stability are essential.

A great variety of properties can be studied: half-lives, transitions and decay properties [11] as well as radii, spins and moments [12, 13], shapes [14, 15] and of course nuclear masses [16, 17]. In the context of this thesis, the property of the nuclei chosen for investigation is the mass.

Nuclear masses are of great importance for the discussion of nuclear structure and an indispensable ingredient for the improvement of mass models. Despite their contribution to nuclear-structure discussions, mass models are nowadays of particular interest in astrophysics. Here, they are used for the prediction of nuclear masses which are out of reach for the current measurement techniques (the "terra incognita", see Fig. 1.1). As pointed out earlier, due to a drastic change of properties compared to light nuclei, heavy nuclei are of particular interest. These nuclei in particular were chosen for investigation within this work. In comparing them to different mass models one can reveal how well the properties of these nuclei are already understood and give hints where to improve theory. The relevance of nuclear mass values is, however, not just limited to nuclear-structure studies and tests of mass models: They are also important input parameters for atomic physics, chemistry and tests of the standard model [17].

In order to determine nuclear masses as well as the other properties effectively, it is crucial to have access to a great variety of different radioactive nuclides. Therefore, two different techniques have been developed: the *In-Flight* (IF) technique [18, 19] and the *Isotope Separation Online* (ISOL) technique [20].[1] For the IF technique, heavy primary particles are accelerated and directed onto a thin target of heavy elements. The resulting high-energetic particles recoil out of the target and are then separated in-flight. Afterwards, they can be transferred e. g. to storage rings for the actual measurements (see Ref. [22]). Using the ISOL technique, light particles are accelerated and directed onto a thick target. Here, particles diffuse out of the target, are then ionized and accelerated. While the IF technique is especially suitable for the production of heavy, short-lived nuclei with high kinetic energy (several hundred keV/u), the ISOL technique yields low energy (several tens of keV in total) light and heavy radioactive ion beams with a high ion-optical quality. Consequently, the choice of method depends on the application. Therefore, a closer look on the application within this thesis, mass measurements, is necessary.

Mass measurements of nuclei can be performed in numerous ways, i. e. by measuring the *time of flight* [23], the *bending in a magnetic field* due to the LORENTZ force [24] or the *revolution frequency* in storage rings [25]. The highest precision to date can be achieved with the use of PENNING *trap mass spectrometry.* In order to reach the precision necessary for the nuclides of interest in the context of this thesis, the latter one is the method of choice. As its name already suggests, PENNING trap mass spectrometry requires trapping of the nuclides. Consequently, a low-energy beam with low emittance and small energy spread is favorable, which points towards the use of the ISOL technique[2]. Hence, the measurements performed in the context of this work were ideally suited to be carried out at the ISOLTRAP experiment [27] based at the ISOLDE facility at CERN [28].

In the next chapter, an overview of the theoretical foundations of PENNING traps is given. An introduction to nuclear-structure theory as well as an overview of mass models is presented in Chapter 3. The experimental setup is described in Chapter 4, followed by a more detailed description of the control system in Chapter 5, which has been enhanced in the context of this thesis. In Chapter 6, details on the data-analysis and evaluation procedure are presented together with the experimental results. The physical interpretation is given in Chapter 7. The thesis concludes with a summary of the results and an outlook for the future.

---

[1] If one is interested mostly in neutron-rich fission products, a nuclear research reactor can be used as well, see e. g. Ref. [21].

[2] Nonetheless, PENNING trap mass spectrometry is also possible using the IF technique. This is done i. e. at SHIPTRAP [26].

2 The Basics of Penning Traps

The quantity which can currently be measured with highest precision is frequency [29]. Therefore, if one is interested in high-precision mass measurements, it is obvious to trace back mass measurements to frequency measurements. This can be achieved using so-called PENNING *traps* [30], which have been developed by DEHMELT [31] and are based on an idea of Frans Michael PENNING [32].

As PENNING trap theory has already been widely discussed, the following chapter is intended as a summary of selected aspects needed for further reading of this thesis. For more details, e. g. the discussion of non-ideal PENNING traps, the reader is referred to the referenced literature, especially to Refs. [30, 33] and the references therein.

In a PENNING trap, a charged particle is stored using a superposition of static magnetic and electric fields. In order to perform mass measurements using a PENNING trap, the mass-dependent eigenfrequencies of the stored particle are determined. Further applications of PENNING traps are aimed at the reduction of the energy and the phase-space volume of the trapped particle (*cooling*) or the selective removal of unwanted species (*cleaning*). Currently, two main types of PENNING traps are in use: The (historically) first type of PENNING traps is based on electrodes with hyperbolic shapes (see Fig. 2.1 a) whereas the second type uses cylindrically shaped electrodes (see Fig. 2.1 b).

2.1 Trapping of Charged Particles in a Penning Trap

In order to trap a charged particle, magnetic and electric fields can be used. Using the LORENTZ force, the equation of motion for a particle with charge q and mass m moving in a magnetic and electric field becomes

$$m\ddot{\vec{r}} = q(\vec{E} + \dot{\vec{r}} \times \vec{B}). \tag{2.1}$$

A homogeneous magnetic field $\vec{B} = B\vec{e_z}$ alone already confines the particle radially. As a result, it is moving on an orbit transverse to the magnetic field lines with the cyclotron frequency ω_c

$$\omega_\mathrm{c} = \frac{q}{m} \cdot B. \tag{2.2}$$

To confine the particle in three dimensions, an electric field has to be used in addition. For convenience, the resulting force should be harmonic [34]. Furthermore, as the radial confinement is already provided by the magnetic field, the force should be isotropic with respect to radial displacement. Solving the LAPLACE equation $\Delta V = 0$ with these constraints, the electric potential $V(z, \rho)$

$$V(z, \rho) = \frac{U_0}{2d^2}\left(z^2 - \frac{1}{2}\rho^2\right) \tag{2.3}$$

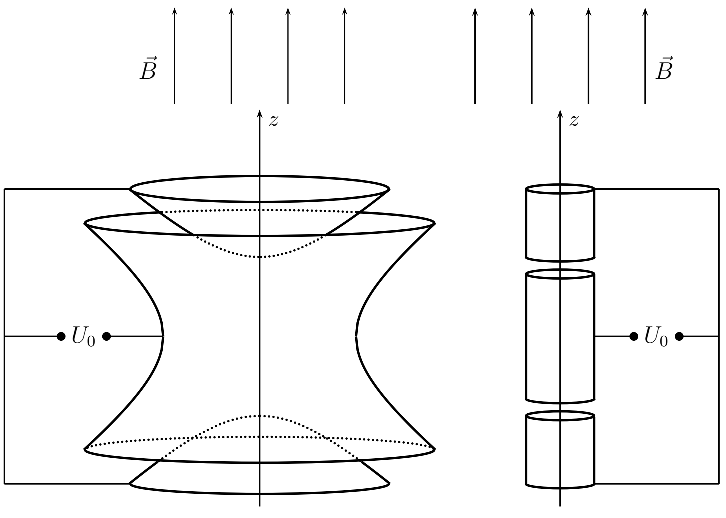

(a) **(b)**

Figure 2.1: *Schematic drawing of a hyperbolic (a) and a cylindrical (b)* PENNING *trap. A* PENNING *trap consists, apart from the required static magnetic field, of a central ring electrode, upper and lower endcaps and correction electrodes (not shown here) to compensate field imperfections. The ring electrode is usually split multiple times to allow excitations (see Section 2.2). In order to inject the particles into or eject them from the hyperbolic trap, the endcaps contain holes in z-direction.*

is obtained. Here, z and ρ denote the cylindrical coordinates and U_0 the electric potential difference between the ring and the endcaps of the PENNING trap. For normalization reasons, a parameter d is introduced and stands for the characteristic dimension of the individual trap used. Solving consequently Eq. (2.1) for this case (see e. g. Ref. [30]), one gets three independent motions with the eigenfrequencies

$$\omega_z = \sqrt{\frac{qU_0}{md^2}} \tag{2.4}$$

$$\omega_\pm = \frac{1}{2}\left(\omega_c \pm \sqrt{\omega_c^2 - 2\omega_z^2}\right). \tag{2.5}$$

In Eqs. (2.4) and (2.5), ω_z is referred to as the *axial frequency*, ω_+ as the *reduced cyclotron frequency* and ω_- as the *magnetron frequency*. In order to obtain physically meaningful results, the root in Eq. (2.5) needs to be positive. This leads to the trapping conditions

$$\frac{|q|}{m}B^2 > \frac{2|U_0|}{d^2} \qquad \text{and} \qquad qU_0 > 0. \tag{2.6}$$

Looking at the eigenfrequencies again, one can clearly see that they are connected to each other by the following relations, some of which are important for the time-of-flight ion-cyclotron-resonance (TOF-ICR) technique discussed later (see Section 2.4):

$$\omega_\mathrm{c} = \omega_+ + \omega_- \tag{2.7}$$

$$\omega_z^2 = 2\,\omega_+\,\omega_- \tag{2.8}$$

$$\omega_\mathrm{c}^2 = \omega_+^2 + \omega_z^2 + \omega_-^2. \tag{2.9}$$

Additionally, one can derive an order of the frequencies, which is in case of PENNING traps used for high-precision mass spectrometry usually

$$\omega_\mathrm{c} \gtrsim \omega_+ \gg \omega_z \gg \omega_-. \tag{2.10}$$

This relation is especially important for the experimental determination of eigenfrequencies (see Section 2.4).

Another important information can be extracted from a TAYLOR expansion of the magnetron frequency ω_- (Eq. (2.5)), giving

$$\omega_- \approx \frac{U_0}{2d^2B}, \tag{2.11}$$

which leads to the result that the magnetron motion is in first order independent of the mass of the particle. This is of particular interest for the removal of contaminations discussed later (see Section 2.3).

In addition (or as an alternative) to the classical ansatz chosen above, the trapped particle can be fully described using quantum mechanics. In particular, this is convenient when investigating the energy of the captured particle. By solving the SCHRÖDINGER equation in case of a particle without spin [30], the three energy eigenvalues E_z and $E_\pm$ corresponding to the different eigenmotions are obtained[1]. The energy E of the whole system is consequently the sum

$$E = E_z + E_+ + E_- = \hbar\omega_z\left(k + \frac{1}{2}\right) + \hbar\omega_+\left(n + \frac{1}{2}\right) - \hbar\omega_-\left(l + \frac{1}{2}\right), \tag{2.12}$$

where k, n, l are the corresponding quantum numbers. It is important to state that the magnetron term has a negative sign, as one can see from Eq. (2.12). Thus, the magnetron motion is unbound.

2.2 Manipulation of Charged Particles in a Penning Trap

Depending on the technique used for mass determination, changing the energy and thus the motion of the trapped particle is either convenient (in order to improve the signal-to-noise ratio) or necessary. Furthermore, selective cleaning or cooling of a particle can only be achieved by making use of such a manipulation. Excitations at the frequency of an eigenmotion or at a sum of them are one possibility to perform this task. For a manipulation of the magnetron or cyclotron motion, a radio-frequency (rf) field is applied to the split ring electrode. For a manipulation of the axial motion, the rf field is

---

[1] To account for a particle with a non-zero spin, a corresponding eigenvalue has to be added. For a particle with spin 1/2, this can be found in Ref. [30] as well.

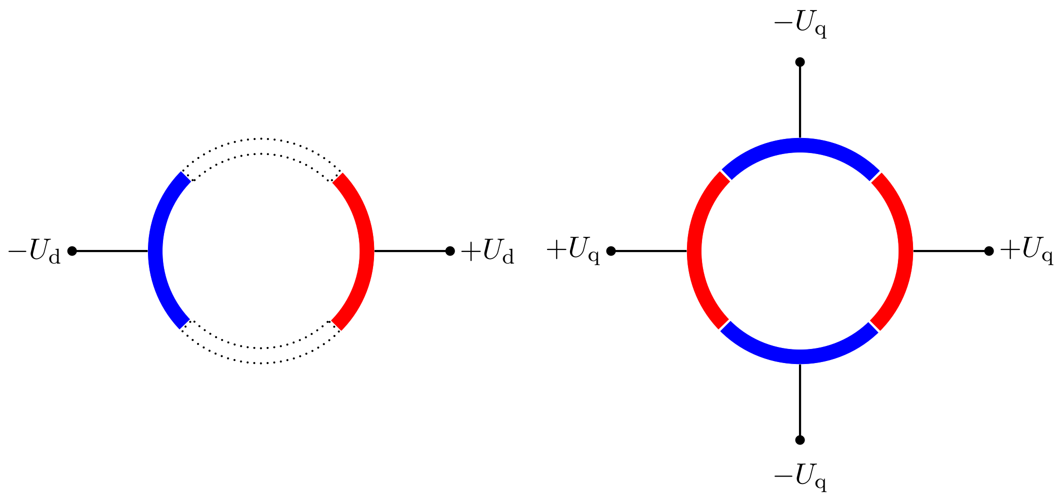

(a) **(b)**

Figure 2.2: *(Color) Schematic view (top) of a dipole (a) and a quadrupole (b) excitation.*

applied to the endcaps of the Penning trap. Thus, the quantum number of the trapped particle can be changed. Most used are *dipole* and *quadrupole* excitations, which are explained in more detail below.[2]

2.2.1 Dipole Excitation

A dipole excitation at the frequency of an eigenmotion can be used to manipulate the corresponding eigenmotion. In order to achieve this, an rf field with an amplitude U_d, a frequency ω_rf and a phase ϕ_rf is applied to two opposing segments of the ring electrode (see Fig. 2.2 a). In case of an excitation in x-direction, the field E_x is then described by

$$\vec{E}_x(t) = \frac{U_\mathrm{d}}{a} \cos\left(\omega_\mathrm{rf} t - \phi_\mathrm{rf}\right) \hat{e}_x, \tag{2.13}$$

with a being a factor depending on the trap geometry.

As thus the radius of the motion can be increased, this excitation is in general used for the removal of unwanted particles (see Section 2.3).

2.2.2 Quadrupole Excitation

Using a quadrupole excitation at the sum frequency of two eigenmotions, these two motions are coupled and energy is transferred from one to the other. The rf field is applied to two opposing electrodes with the same phase and to the perpendicular

---

[2] Recently, octupole excitations have been investigated as well, but as they were not used for the measurements presented in this thesis, the interested reader is referred to Ref. [35] and the references therein.

electrodes with a phase shift of 180°, respectively (see Fig. 2.2 b). It is described by

$$\vec{E}_x(t) = \frac{2U_\mathrm{q}}{a^2} \cos\left(\omega_\mathrm{rf} t - \phi_\mathrm{rf}\right) y\, \hat{e}_x \tag{2.14}$$

$$\vec{E}_y(t) = -\frac{2U_\mathrm{q}}{a^2} \cos\left(\omega_\mathrm{rf} t - \phi_\mathrm{rf}\right) x\, \hat{e}_y. \tag{2.15}$$

Quadrupole excitation is used for cooling and cleaning processes in a Penning trap (see Section 2.3) and for the determination of the eigenfrequencies of the stored particles (see Section 2.4).

2.3 Ion Cooling and Cleaning in a Penning Trap

As introduced in the beginning of Section 2, cooling in a Penning trap aims at reducing the phase-space volume of the trapped particle ensemble whereas cleaning means the removal of unwanted species. Both aspects are especially important when dealing with radioactive ions.

In the context of this work the technique used for these purposes is the *mass-selective buffer-gas cooling* [36], which will be described hence in greater detail: As the name already suggests, the Penning trap is filled with a buffer gas. In this buffer gas, the trapped particles are moderated by colliding with the gas molecules. Due to its high ionization energy, usually a noble gas (typically helium) is used. The force acting on a particle in the buffer gas can be described by

$$\vec{F} = -\delta m \vec{v}, \tag{2.16}$$

with m being the mass and $\vec{v}$ the velocity of the particle to be cooled. The damping coefficient δ is in this case [37]

$$\delta = \frac{q}{m} \frac{1}{K_\mathrm{ion}} \frac{p/p_\mathrm{N}}{T/T_\mathrm{N}}. \tag{2.17}$$

Here, K_ion represents the mobility of the ions, p/p_N the buffer-gas pressure relative to the normal pressure and T/T_N the temperature relative to normal temperature.

A motion with the initial amplitude ρ_0 is damped according to

$$\rho(t) = \rho_0\, \mathrm{e}^{-\alpha t}. \tag{2.18}$$

The axial motion in a Penning trap is damped with $\alpha = \delta$. Hence, it is cooled by simply waiting until the desired amount of energy has been dissipated. For the cyclotron (+) and magnetron (−) motion, α is equal to

$$\alpha_\pm = \pm\delta \frac{\omega_\pm}{\omega_+ - \omega_-}. \tag{2.19}$$

So with time, the cyclotron motion is damped away, but the magnetron motion increases in radius (see Fig. 2.3 a). With $\omega_+ \gg \omega_-$ (see Eq. (2.10)) it follows that $|\alpha_+| \gg |\alpha_-|$ as well. Thus, the decrease of the cyclotron radius is much faster than the increase in magnetron radius.

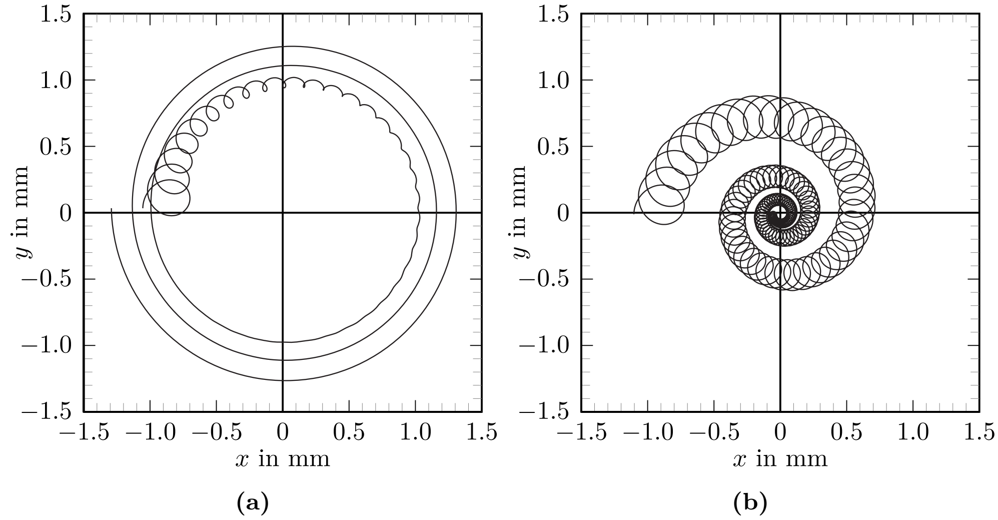

Figure 2.3: *Simulated ion trajectories in a buffer gas atmosphere transverse to the magnetic field. In (a), a fast decrease of the (smaller) cyclotron radius and a slow increase of the (larger) magnetron radius due to collisions with the buffer gas is visible. In (b), a quadrupole excitation is applied to convert the magnetron motion into cyclotron motion. The magnetron as well as the cyclotron motion decrease and the particles are centered (taken from [17]).*

In order to turn this feature into a cooling process for both motions, one uses as a first step a dipole excitation at the magnetron frequency, which is nearly mass independent according to Eq. (2.11). Consequently, all particles are excited to a larger magnetron radius. This radius has to be larger than the exit hole in the endcap of the trap electrodes. In a second step, a quadrupole excitation at the cyclotron frequency ν_c of the desired particles is applied. For the particles in resonance, this couples the magnetron and cyclotron motion, which leads to a conversion of the magnetron energy into reduced cyclotron energy. Thus, the magnetron radius of these particles decreases and, as the cyclotron motion is being damped away quickly in the buffer gas, the particles are effectively re-centered (see Fig. 2.3 b).[3] Non-resonantly excited particles stay on the larger magnetron radius, which increases even further due to the collisions with the buffer gas. Upon axial ejection from the trap, the non-centered particles are blocked as they hit the endcap electrode. Thus, cleaning is achieved. This whole process takes on the order of some tens to some hundred milliseconds depending on the mass resolution aimed for.

If the mass of the unwanted species in the trap is well known, one can also apply a dipole excitation at the reduced cyclotron frequency: By consequently increasing the radius of the reduced cyclotron motion, one can drive the particles out of the trap center and make them hit the trap electrodes. However, due to the mass dependence of the reduced cyclotron frequency, a separate rf excitation is needed for each species to be removed.

---

[3] One has to ensure by using a suitable amplitude for the quadrupole excitation that the conversion of the two motions is faster than the increase of the magnetron radius due to the collision with the buffer gas. Otherwise no re-centering is possible.

2.4 Determination of the Cyclotron Frequency

In the context of this thesis, the time-of-flight ion-cyclotron-resonance (TOF-ICR) detection technique [38] (see Fig. 2.4 a) is used for the determination of the mass of the captured ions in the trap and hence is described in more detail.

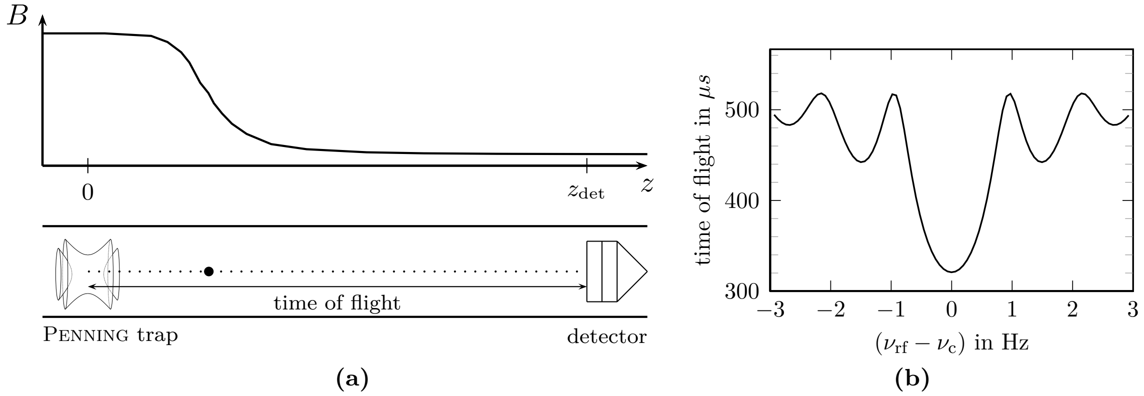

Figure 2.4: *The time-of-flight ion-cyclotron-resonance technique (a) and a simulated time-of-flight resonance (b).*

Assuming a particle captured in a PENNING trap with the axial motion damped away and thus only motions in the radial plane left, the mean magnetic moment of this particle is calculated as [21]

$$\vec{\mu} = -\mu\,\vec{e_z} = -\frac{q}{2}(\rho_+^2\omega_+ + \rho_-^2\omega_-)\,\vec{e_z}. \tag{2.20}$$

Furthermore, the energy of the particle due to its magnetic moment in the magnetic field is calculated as

$$E = -\vec{\mu}\cdot\vec{B} \tag{2.21}$$

If the particle is now ejected out of the trap (and thus out of the magnetic field) towards a detector (see Fig. 2.4 a), it experiences a force F in z-direction due to the magnetic field gradient according to

$$\vec{F} = -\vec{\nabla}E = -\mu\frac{\partial B}{\partial z}\vec{e_z}. \tag{2.22}$$

This force causes a change of the time of flight towards the detector depending on the magnetic moment of the particle. As one can see in Eq. (2.20), the magnetic moment itself is dependent on the amplitudes of the radial eigenmotions. The time of flight towards the detector is smaller the more energy is stored in these motions, as the radial energy is converted to axial energy in the magnetic field gradient. However, assuming the same radii for both motions ($\rho_+ = \rho_-$), the energy stored in the cyclotron motion is much larger because of $\omega_+ \gg \omega_-$.

The TOF-ICR method makes use of this principle for the determination of the cyclotron frequency: By using first a dipole excitation at the magnetron frequency to increase the magnetron radius and then a quadrupole excitation at the cyclotron frequency, the energy from the magnetron motion can be converted to the cyclotron motion (see Fig. 2.5). In case of a resonant excitation on ν_{c}, this energy transfer is more efficient and thus, the time of flight to the detector is minimal. The typical line shape of

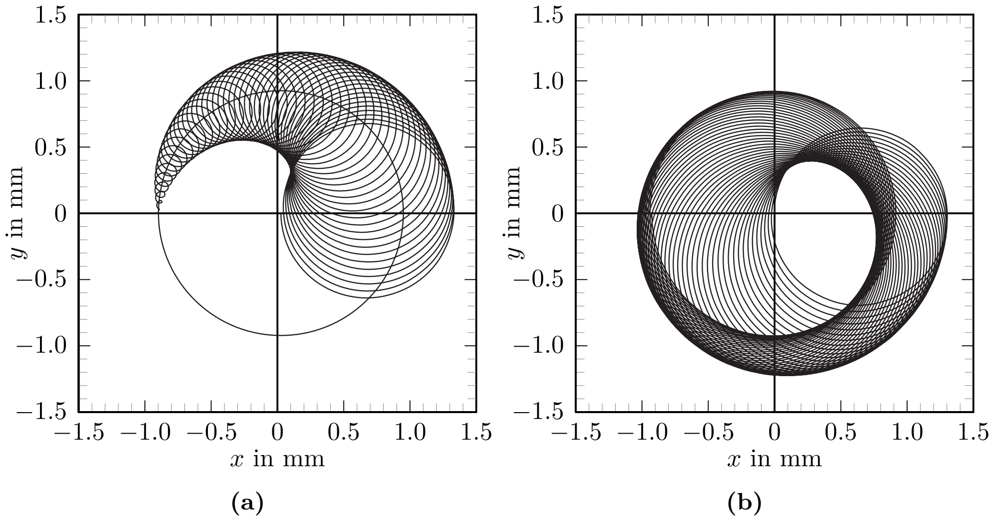

Figure 2.5: *Simulated ion trajectories transverse to the magnetic field with an applied quadrupole excitation at* $\nu_{rf} = \nu_c$. *A pure magnetron motion is converted into a pure cyclotron motion. (a) shows the first half of the conversion and (b) the second half. The initial radius of the magnetron motion is the same as the final radius of the cyclotron motion (taken from Ref. [17]).*

the recorded times of flight depending on the excitation frequency ν_{rf} (usually called "a TOF resonance") can be seen in Fig. 2.4 b. It is based on the Fourier transformation of the rectangular excitation signal profile with the width of the resonance being inversely proportional to the excitation time.

The time of flight from the trap center $z = 0$ to the detector at $z = z_{\mathrm{det}}$ depending on the excitation frequency ω_{rf} can be calculated by

$$T(\omega_{\mathrm{rf}}) = \int_0^{z_{\mathrm{det}}} \sqrt{\frac{m}{2(E_0 - qU(z) - \mu(\omega_{\mathrm{rf}})[B(z) - B(0)])}} \mathrm{d}z, \tag{2.23}$$

with E_0 being the kinetic energy of the particle at the trap center and $U(z)$, $B(z)$ the electric and magnetic fields along the z-axis, respectively [38]. This calculation of the time of flight allows a detailed fit to the recorded data points. Thus, the cyclotron frequency of the particle can be determined allowing in turn via Eq. (2.2) the calculation of its mass (see Section 6.1 for more details).

3 Nuclear Structure and Mass Models

After the discovery of the nucleus by RUTHERFORD and his colleagues [1, 2], the hunt for a description of the nuclear structure started. As α particles had been observed to be emitted from some nuclei, first ideas assumed them to be the constituents of the nucleus [39]. Based on this idea, GAMOW suggested to characterize the nucleus as a liquid drop [39, 40], making it composed of an incompressible fluid with homogeneous density and strong surface tensions. After the discovery of the neutron in 1932, which changed the picture of the nucleus completely, the first breakthrough in the description of the nucleus could be reached: WEIZSÄCKER transferred the liquid-drop model to a nucleus being composed of protons and neutrons and consequently managed to provide for the first time a promising reproduction of nuclear binding energies and thus mass values [4]. The first usable mass formula was born!

Already at this time, evidences for a shell structure of the nucleus in analogy to the shell model in atomic physics were discussed [41, 42]. The origin of this discussion was the fact that nuclei with an even number of protons or neutrons turned out to be bound more strongly. This was then called the *pairing effect*. Consequently, a shell structure based on two protons or neutrons in each shell (according to the PAULI principle) was suggested. In the liquid-drop mass formula, however, this assumed shell structure was only interpolated based on the binding energies of nuclei with even numbers of protons and neutrons. In 1948, GOEPPERT-MAYER summarized all experimental evidences for closed shells at the magic numbers 20, 50, 82 and 126 so far [6], thus triggering a new discussion about a possible shell structure of the nucleus.

The next breakthrough in nuclear structure came shortly after, when she and JENSEN succeeded in deriving a shell model for the nucleus. The basic assumptions of this shell model are a single-particle potential with "a shape somewhat between that of a square well and a three-dimensional isotropic oscillator" [44] in which the particle moves independently, and a strong spin-orbit coupling [7, 8]: With the orbital angular momentum l, the spin s and the total angular momentum $j = l \pm s = l \pm 1/2$, the energy of the $j = l + 1/2$ level is significantly decreased due to the strong spin-orbit coupling (see Fig. 3.1). With the spin-orbit coupling proportional to l, a shell gap, defined as two consecutive levels with a large difference in energy, appears after each first occurrence of a higher l.

Within this model, referred to as *Independent Particle Model* (IPM), not only the observed magic number could be reproduced and hence explained, but also the pairing effect and many observations of nuclei regarding spins, magnetic moments and isomers [44]. However, as no nucleon-nucleon interaction is included in this model, discrepancies occur. Consequently, they have to be either added "on top", which is done in up-to-date shell-model calculations as *residual interactions*, or incorporated from the beginning into the single-particle potential, which is part of the mean-field approaches discussed in the context of (microscopic) mass models in Section 3.4.2.

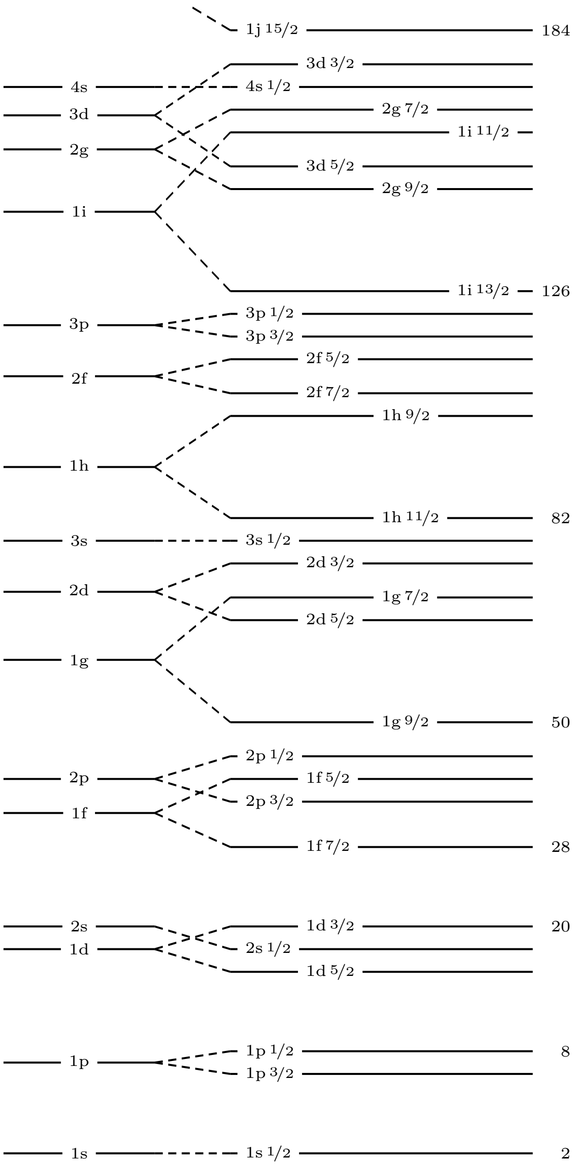

Figure 3.1: *Shell-model level scheme. The first column shows the single-particle potential levels, the second the levels resulting from strong spin-orbit coupling. The magic numbers at each shell gap are given in the last column. Adapted from Ref. [43].*

3.1 Binding Energies

In order to understand the structure of the nucleus, different parameters can be studied. One of these is the binding energy, as it represents the sum of all interactions within the nucleus. According to EINSTEIN's famous equation [45]

$$E = m \cdot c^2 \tag{3.1}$$

the binding energy which is released during the formation of the nucleus results in a mass of the nucleus m_{nucl}, which is less than the sum of the masses of its constituents. This effect is called *mass defect.* The binding energy B of a nucleus with mass m_{nucl} can be calculated in terms of the mass as

$$B(N, Z) = \left[N \cdot m_{\mathrm{n}} + Z \cdot m_{\mathrm{p}} - m_{\mathrm{nucl}}(N, Z)\right] c^2, \tag{3.2}$$

with N being the number of neutrons, Z the number of protons and m_{p} and m_{n} the mass of the proton and of the neutron, respectively. Consequently, the mass allows studying the systematic behavior of the binding energy as a function of different numbers of nucleons. Useful quantities for this study are e. g. the binding energy of the last neutron S_{n} (*neutron separation energy*) or of the last two neutrons $S_{2\mathrm{n}}$ (*two-neutron separation energy*) defined as

$$S_{\mathrm{n}} = B(N, Z) - B(N-1, Z) \tag{3.3}$$

$$S_{2\mathrm{n}} = B(N, Z) - B(N-2, Z). \tag{3.4}$$

The proton separation energies can be used as well and are calculated likewise.

One example of these energies is shown in Fig. 3.2 for cadmium isotopes. For both energies, a sudden drop occurs around $N = 50$ and $N = 82$, marking a shell closure. For the two-neutron separation energy, one sees a smooth decrease (Fig. 3.2 b), whereas in case of the (one-)neutron separation energy, an odd-even staggering due to the pairing effect is visible (see Fig. 3.2 a and Section 3.2). Furthermore, one can see that the pairing effect is roughly half as big as the drop due to the shell closure. Hence, both effects are on the same order of magnitude.

From these separation energies, characteristics of the nuclear mass surface can become visible. This allows assumptions concerning the underlying structure of the nucleus, like the appearing of shell closures (resulting in a sudden drop as visible in Fig. 3.2) or deformations (which would be visible as a bump). However, with binding energies always representing the complete interaction, one has to be careful as the sum of different effects may compensate one another leaving no visible effect.

Making use of the separation energies, the limits of bound nuclei can be determined as well [16]. If one adds a further nucleon to gain a nucleus beyond this limit, the nucleon "drips" out again, giving rise to the name *drip line* for a plot of these nuclei in the nuclear chart (see Fig. 1.1). In case of the one-nucleon separation energies, the drip line is defined by $S_{\mathrm{n,p}} = 0$. For the two-nucleon separation energies, it is defined in analogy by $S_{2\mathrm{n},2\mathrm{p}} = 0$. The drip line can be calculated for both types of nucleons, neutrons and protons, each based on the one-nucleon or two-nucleon separation energies. In case of choosing the one-nucleon separation energies as a starting point, the pairing effect

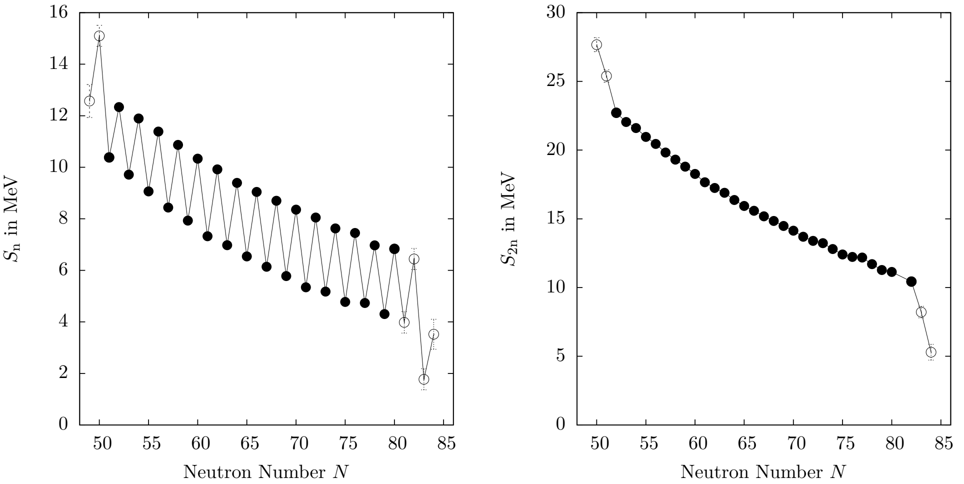

(a) **(b)**

Figure 3.2: *One- (a) and two-neutron separation energies (b) of the cadmium chain from* $N = 50$ *to* 82*. In case of* S_n *and* S_{2n} *values, open circles denote values already included in the* Atomic Mass Evaluation 2003 *(*AME2003*) [46] and closed circles denote values including recent mass measurements [46–50]. Taken from Ref. [51].*

already visible in Fig. 3.2 a shows up. Hence, in Fig. 1.1 the drip line was calculated using the two-nucleon separation energies.

3.2 Pairing Effect

Already in 1932 HEISENBERG observed that nuclei with an even number of neutrons or protons are particularly stable [41, 42]. This phenomena is explained by means of the PAULI exclusion principle in combination with the strong interaction: Due to the attractive force, two nucleons are most bound when their spatial wave functions are identical. However, due to the symmetry of the spatial wave function with respect to an exchange of the two particles in this case, their spin wave functions have to be antisymmetric. Therefore, pairs of nucleons with minimal spin are preferred. This is different to atomic physics, where, due to the repulsive electric force between the electrons in the atom, asymmetric spatial wave functions and hence a maximum spin configuration are favored.

As there are two types of nucleons, three different types of pairing can occur: First, pairing between neutrons, second pairing between protons, and third pairing between an unpaired proton and an unpaired neutron. However, the pairing between proton and neutron is different to the other two cases as the nucleons are in general not in the same orbits. The contribution of the pairing effect to the binding energy can be quantified using the *neutron paring gap* Δ_N, the *proton paring gap* Δ_Z and the proton-neutron interaction energy δ. Throughout the nuclear chart, a quite smooth behavior of the pairing gap energies is seen [52]. Defining therefore a *smooth mass surface* using the masses of the even-even nuclei as $M_0(N, Z)$

$$M_{\text{even-even}}(N, Z) = M_0(N, Z), \tag{3.5}$$

the masses of the odd-even and odd-odd nuclei can be approximated via the pairing gaps

$$M_{\text{even-odd}}(N, Z) = M_0(N, Z) + \Delta_{\text{Z}} \tag{3.6}$$

$$M_{\text{odd-even}}(N, Z) = M_0(N, Z) + \Delta_{\text{N}} \tag{3.7}$$

$$M_{\text{odd-odd}}(N, Z) = M_0(N, Z) + \Delta_{\text{Z}} + \Delta_{\text{N}} - \delta. \tag{3.8}$$

Nevertheless, one has to note that the strength of all these pairing effects is not constant but decreases with increasing mass number A. Furthermore, especially for small nucleon numbers ($A < 16$), close to the $N = Z$ line, and around the shell closures this smooth behavior of the mass surface is no longer present and hence especially interesting for investigation.

3.3 Isomerism and Shape Coexistence

In several cases, it is possible to measure two different mass values belonging without doubt to one nucleus. This phenomena was first discovered by Otto HAHN in 1921 [53], but the nature of these experimental findings had not been understood until WEIZSÄCKER interpreted them in 1936 as metastable excited states of the same nucleus [5]. These states were then called *isomers*.

The name is taken from chemistry, where isomers consist of the same particles, but form a different shape. However, there is an important difference: In chemistry, the binding energies of two isomers are basically the same. In contrast, the excitation energies of nuclear isomers have been observed to span a huge range from several eV (like in case of ^{229}Th) up to several MeV (like ^{147}Gd) [54].

Half-lives of isomers differ on an even larger scale: While there is no strict definition how long the half-life of nuclear state has to be in order to qualify as an isomer, 1 ns is usually regarded as a lower limit [55]. On the other side of the scale, one finds isomers with half-lives $> 10^{15}$ years, namely ^{180}Ta (with the ground-state being surprisingly rather short-lived with 8.1 h) [54].

Looking at their distribution over the nuclear chart, long-lived ($t_{1/2} > 1\,\text{ms}$) and highly-excited ($E_{\text{exc}} > 1\,\text{MeV}$) isomers are found largely around the magic numbers. However, a large number of even longer-lived isomers ($t_{1/2} > 1\,\text{hour}$) is seen in the region around $N = 108$ and $Z = 72$ [55].

Different from de-excitations of metastable states in atomic physics, which can happen quickly by collisions with other atoms, nuclear isomers usually de-excite via spontaneous emission as there are in general no collisions of nuclei. Different types of isomers have been observed, especially *shape isomers*, where the excited states differ simply in the shape of the nucleus, and *spin isomers*, where ground-state and isomer differ in spin. The decay of the most-common spin isomers usually happens via electromagnetic processes, but other examples are known as well. A very fascinating aspect of isomer research is the vision of a γ-ray laser [55].

In the case that two states of a nucleus differ in shape, but not much in energy and the half-life of the excited state is not long enough to be qualified as "metastable", this phenomena is referred to as *shape coexistence* [15].

3.4 Mass Models

At present, mass models describing nuclear masses serve two main purposes: First, they are aimed at understanding the influences of the different terms of the interaction within the nucleus. Therefore, the measured mass values are reproduced as well as possible and then compared again to the experimental values or to other, different mass models. From the differences one can extract valuable information on the missing effects in the nuclear interaction. Second, mass models are made in order to predict masses of nuclei for which no experimental values are available as they are not naturally occurring and cannot be produced at radioactive beam facilities so far. This is especially the case for neutron-rich nuclei far away from stability (the "terra incognita" as already mentioned before, see Fig. 1.1). However, these nuclei are of particular interest for the explanation of nuclear synthesis: Only the synthesis of nuclides up to the region of ^{62}Ni can be explained by fusion in a star as up to these nuclides the binding energy per nucleon increases (see Fig. 3.3). For heavier nuclides other concepts like the *rapid-* or *slow-neutron-capture process* (r-process or s-process respectively) as well as the *proton-capture process* (p-process) are necessary [56–58]. The explanation of the natural abundances of elements via these processes as well as the identification of their place of occurrence (e. g. in supernova explosions) relies heavily on predicted masses.

Different approaches have been chosen to describe the mass of nuclei: The starting point was the semi-empirical liquid-drop mass model derived by WEIZSÄCKER, which is a so-called *macroscopic mass model*, as it focuses on macroscopic aspects of the nucleus like surface tension [4]. In order to achieve a more fundamental description, the detailed forces within the nucleus have to be taken into account using quantum mechanics. This approach led to the development of *microscopic mass models.* However, as the computing power required for these models has not been sufficient for calculations on heavy nuclei, a combination of both approaches, a macroscopic treatment with microscopic corrections was developed: the *macroscopic-microscopic-* or *mic-mac mass models.*[1]

In order to compare the different mass models with respect to the reproducibility of the measured masses, one makes use of the root-mean-square (rms) deviation

$$\sigma_{\mathrm{rms}} = \sqrt{\frac{1}{n}\sum_{i=1}^{n}\left(m_i^{\mathrm{exp}} - m_i^{\mathrm{theo}}\right)^2}, \tag{3.9}$$

with m_i^{exp} representing the experimentally determined mass, m_i^{theo} the mass predicted by the corresponding model and n the number of mass values included.

---

[1] For a more detailed discussion of mass models going beyond the information given in this thesis, the interested reader is referred to Ref. [16] and the references therein.

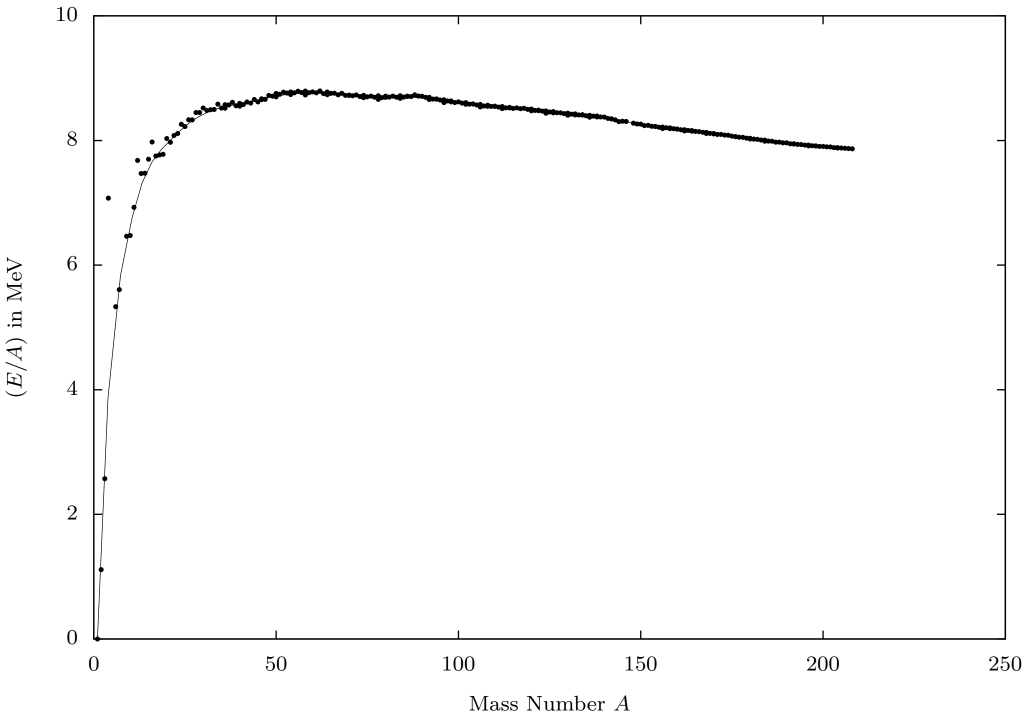

Figure 3.3: *Plot of the binding energy (E) per nucleon versus number of nucleons A for stable nuclides included in* NUBASE2003 *[54]. The nuclide with the largest binding energy per nucleon is* ^{62}*Ni. The synthesis of elements up to this region can be explained by fusion in a star. For heavier nuclides, other concepts are needed. These concepts rely on mass values which cannot be measured and thus need to be extracted from mass models. The line is intended to guide the eye.*

3.4.1 Macroscopic Mass Models

For the justification of using macroscopic models and not directly focusing on microscopic models, one can quote WEIZSÄCKER [4] when proposing the liquid-drop mass formula:

> „Da die Ruhenergien [...][von Protonen und Neutronen] groß sind gegen die Bindungsenergien der Kerne, sollte man ihre Bewegung im Kern in erster Näherung nach der unrelativistischen Quantenmechanik beschreiben können. Wenn die Kräfte zwischen den Elementarteilchen bekannt wären, müßte es also im Prinzip möglich sein, die Bindungsenergien, d. h. die Massendefekte aller Atomkerne zu berechnen. Da die Versuche, diese Kräfte direkt theoretisch zu bestimmen, noch nicht zu eindeutigen Ergebnissen geführt haben, sind wir vorläufig auf den umgekehrten Weg angewiesen: auf die Ableitung der Kernkräfte aus den empirisch bekannten Massendefekten.“

> “As the rest energy of [...] [protons and neutrons] is large if compared to the binding energies of the nuclei, it should be possible to calculate their movement within the nucleus by using non-relativistic quantum mechanics in first approximation. If the forces between the elementary particles were known, it should be possible, in principle, to calculate the binding energies, i. e. the mass defects of all nuclei. However, as the efforts to determine these forces theoretically have not yet led to clear results, we have to use the reversed way for the moment: the derivation of the nuclear forces from the empirical known mass defects.”[2]

Unfortunately, almost 80 years later, the basic statement is still true: It is still not possible to calculate binding energies *ab initio* [16]. Thus, the semi-empirical mass formula developed by WEIZSÄCKER is still one important starting point for the calculation of binding energies. It was slightly modified later-on to its present form [16, 59, 60]

$$E = a_{\mathrm{vol}}A - a_{\mathrm{sf}}A^{2/3} - \frac{3e^2}{5r_0}\frac{Z^2}{4\pi\epsilon_0}A^{-1/3} + (a_{\mathrm{sym}}A + a_{\mathrm{ss}}A^{2/3})I^2, \tag{3.10}$$

with $I = (N - Z)/A$ being the *charge-asymmetry parameter*. The first term takes into account the increase of binding energy with increasing nucleon number (volume) and the second term the decrease due to the nucleons at the surface being less bound (surface tension), both accounting for the short-range nuclear force. The third term represents the repulsive influence of the infinite-range COULOMB force. The forth term is a correction term to the volume and surface term: It takes into account that both terms are dependent on the neutron-proton composition of the nucleus. WEIZSÄCKER also described a possibility of taking into account pairing effects by interpolation [4]. However, as this is already a microscopic correction, it is omitted in Eq. (3.10).

In order to draw any predictions from this formula, its variable parameters a_{vol}, a_{sf}, a_{sym}, a_{ss} and r_0 need to be fixed. This is done by fitting them against a collection

---

[2] The language of the original publication is German. The English translation was done by the author of this thesis.

of known masses. A resulting set of fit parameters can be found in Tab. 3.1. The initial parameters for this fit were taken from Ref. [16] and had been based on the 1768 measured mass values with $N, Z \geq 8$ included in the AME1995 [61]. The final set of parameters shown in Tab. 3.1 has been obtained by re-fitting them against the 2149 measured nuclides with $N, Z \geq 8$ included in the AME2003 [46][3]. As a fit routine, a nonlinear least-squares MARQUARDT-LEVENBERG algorithm included in the program GNUPLOT [62] has been used.

Table 3.1: *Set of fit parameters obtained for the liquid-drop model as described by Eq. (3.10) using a nonlinear least-squares* MARQUARDT-LEVENBERG *algorithm. The parameters have been re-fitted against the 2149 measured nuclides with $N, Z \geq 8$ included in the* AME2003 *[46]. As a starting point for the fit, the parameters obtained in Ref. [16] using* AME1995 *data were chosen.*

parameter	value
a_{vol}	15.67 MeV
a_{sf}	17.60 MeV
a_{sym}	−26.27 MeV
a_{ss}	17.10 MeV
r_0	1.227 fm

With a resulting rms deviation of $\sigma_{\mathrm{rms}} = 2.89\,\mathrm{MeV}$ (a compilation of the σ_{rms} for different mass models can be found in Tab. 3.2), the liquid-drop model is surpassed by the more complex and up-to-date models discussed later. Nevertheless, taking into account its date of origin, its simplicity and the fact that it only makes use of five fit parameters, this is a remarkable achievement.

Table 3.2: *σ_{rms} for different mass models with respect to the AME2003 [46]. The models chosen provide a complete mass table and were fitted against the nuclides included in the* AME*2003. The total number of parameters is denoted by n.*

Modell	n	σ_{rms} in MeV
liquid drop	7	2.894
HFB-19	30	0.583
HFB-20	30	0.583
HFB-21	30	0.577
D1M	14	0.798
FRDM-2012	38	0.570

3.4.2 Microscopic Mass Models

In order to explain the forces within the nucleus and not only describe the resulting nuclear masses, the development of microscopic models is essential. In addition, clear deviations between the masses calculated using the liquid-drop mass formula and the

---

[3] Re-fitting the parameters against the 2294 nuclides with $N, Z \geq 8$ included in the AME2011 [9] yields parameters which agrees within their respective uncertainties with the values shown in Tab. 3.1.

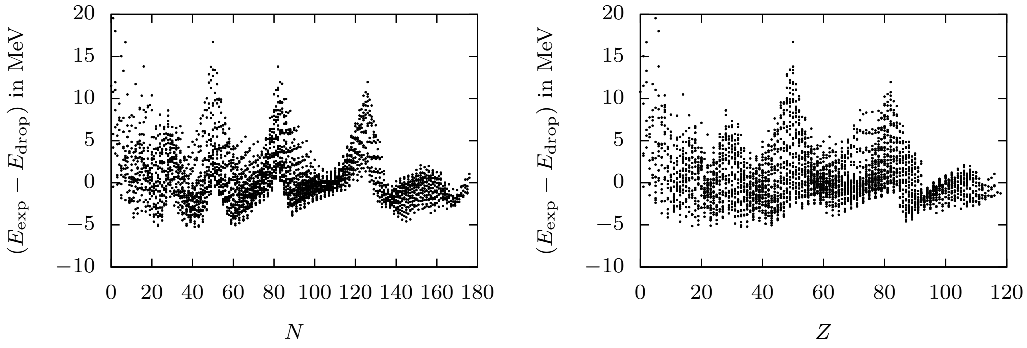

(a) **(b)**

Figure 3.4: *Differences between the binding energies predicted by the liquid-drop model (Eq. (3.10)) and the experimental values [46]. (a) shows the differences depending on the neutron number N and (b) depending on the proton number Z. Clear deviations for the numbers 28, 50, 82 and 126 are visible, thus motivating the development of microscopic mass models.*

experimental values for the nuclide numbers 28, 50, 82 and 126 (see Fig. 3.4) demonstrate the need for models taking into account shell effects for an improved reproduction of nuclear masses.

As already mentioned before, the first attempt in this field was the Ipm. For the single-particle potential, the use of a harmonic potential is convenient as the resulting Schrödinger equation can be solved analytically. Nevertheless, a more precise description is provided using a Woods-Saxon potential [63], which is composed of a spin-independent central potential, a potential taking into account spin-orbit interactions and the Coulomb potential [64]. Making use of the Ipm, the occurrence of the observed magic numbers can be explained and hence many spectroscopic observations. However, the calculation of useful mass values is not possible with such a model, since all many-body interactions are neglected. This deficiency lead to the search for a microscopic model based on *realistic interactions* to calculate masses. Unfortunately, these models are still limited to light nuclei. This gave rise to the development of microscopic models based on *effective forces*, which take two- and three-body interactions into account, but average them to a mean field. They are thus referred to as *mean-field calculations* [65].

Realistic Interactions

The first, basic ingredient for a microscopic model based on realistic interactions is the non-relativistic static Schrödinger equation

$$H\Psi = E\Psi. \tag{3.11}$$

As a second ingredient, the interaction between the nucleons has to be used. As a derivation *ab initio* from *Quantum Chromodynamics* (Qcd) is still not possible, these interactions have to be fitted to experimental data [66, 67].

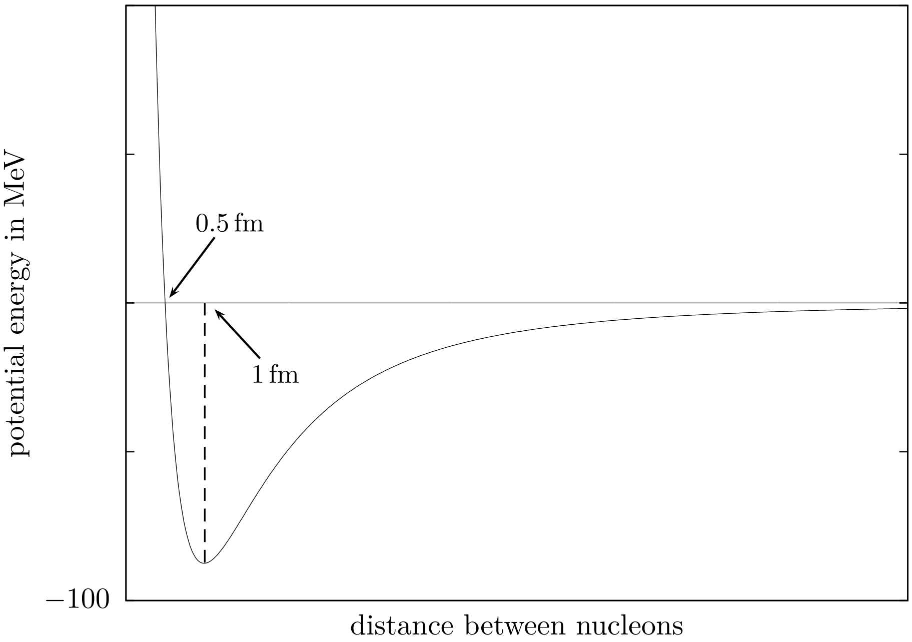

Figure 3.5: *The schematic nucleon-nucleon potential. The potential is around 1 fm (indicated by a dashed line) strongly attractive and starts becoming repulsive for distances smaller than 0.5 fm due to the hard core. The potential depth is slightly smaller than 100 MeV.*

The major part of the interaction between the nucleons comes from the nucleon-nucleon interaction V_{ij}, which is shown in Fig. 3.5. It is fitted to nucleon-nucleon scattering data and to properties of the simplest known two-nucleon system, the deuteron. One example for this kind of interaction is the *Argonne V18* [68, 69]. Nevertheless, the sole use of two-nucleon ($2N$) interactions leads only to systematic underbound nuclei [68]. Consequently, a three-nucleon ($3N$) interaction V_{ijk} like the *Illinois-7* is added in addition [70]. In contrast to the $2N$ interaction, the $3N$ interaction cannot be fitted to scattering data because of its small effect relative to the $2N$ interaction and too few data available. Thus, it has to be derived phenomenologically by comparing the calculated results with experimental data [70, 71].

Including the kinetic energy as well as the $2N$ and $3N$ interactions, the HAMILTONIAN results in

$$H = \sum_{i=1}^{A} \frac{p_i^2}{2m_i} + \sum_{i<j}^{A} V_{ij} + \sum_{i<j<k}^{A} V_{ijk}. \tag{3.12}$$

Solving the SCHRÖDINGER equation in this case turns out to be quite difficult: Due to the short-range repulsion of the nucleon-nucleon force (see Fig. 3.5), perturbation theory is rather difficult and the massive increase of complexity with growing mass number A requires a substantial amount of computing power [16]. This currently limits the applicability of this method to light nuclei with $A \leq 12$. However, within these limits, nuclear energies and levels can be reproduced quite well [70].

In addition to the non-relativistic approach discussed above, there are also relativistic approaches such as the *CD-Bonn* model treating the nucleons as DIRAC spinors [72, 73].

However, $3N$ forces are not yet included in this model giving rise to discrepancies similar (but smaller) to the ones already mentioned for the non-relativistic approach. In addition, the calculation are limited as well to light nuclei.

Mean-Field Calculations

With the nuclear many-body problem being somewhat difficult to solve ab initio as mentioned above, and thus presently unsuitable for the calculation of masses of heavier nuclei, one tends to modify the independent particle model to include many-body interactions as well.

Therefore, one averages the many-body interactions to a *mean field* [65, 74]. Using an effective two-body interaction[4] V_{ij}^{eff}, the HAMILTONIAN changes to

$$H^{\text{eff}} = \sum_{i=1}^{A} \frac{p_i^2}{2m_i} + \sum_{i<j}^{A} V_{ij}^{\text{eff}}. \tag{3.13}$$

The interaction most frequently used as an ansatz for V_{ij}^{eff} is the so-called SKYRME *force* [75]. A more recent alternative to the SKYRME force is the GOGNY *force* [76]: In contrast to the infinite-range SKYRME force, the GOGNY force has a finite range, which makes it more realistic on the one hand, but on the other hand way more difficult to calculate. Both forces have in common that they use a number of parameters, which have to be fitted to experimental data.

As a consequence of now using an effective interaction and treating the nucleons as independent particles, the many-body wave function Ψ has to be approximated by a product Φ of A single-particle wave functions ϕ_i. Hereby, one has to bear in mind, that nucleons are fermions. Consequently, the resulting wave function has to be antisymmetric with respect to the exchange of two particles according to the PAULI principle. This is ensured by using the SLATER determinant

$$\Psi \to \Phi = \det\{\phi_i\}. \tag{3.14}$$

For solving the resulting SCHRÖDINGER equation the RITZ *variational principle* is used, which is in turn based on the HAMILTONIAN *principle*. Hence, the ground-state energy E_0 is approximated by variation of Φ with

$$\langle \Phi | H^{\text{eff}} | \Phi \rangle \geq E_0 \quad \forall \quad \Phi. \tag{3.15}$$

In this approach, the SCHRÖDINGER equation is re-formulated by means of a functional derivative δ to

$$\frac{\delta}{\delta\Phi} \langle \Phi | H^{\text{eff}} | \Phi \rangle = 0. \tag{3.16}$$

For actually solving Eq. (3.16), the HARTREE-FOCK *method* is used: Substituting the SLATER determinant (3.14) into Eq. (3.16), the so-called *HF equations*

$$h_i(\phi_i)\,\phi_i = e_i \phi_i \tag{3.17}$$

---

[4] For simplicity, from here on only a two-body interaction is taken into consideration.

are derived. Here, h_i denotes the single-particle HAMILTONIAN including the *mean field* averaged from the effective interaction V_{ij}^{eff} and e_i the single-particle energy. These equations have to be solved iteratively for two reasons: First, the HF equations are highly non-linear, which makes in general an analytical solution impossible. Second, as one can see from Eq. (3.17), h_i depends explicitly on ϕ_i. This dependence results from the fact, that the averaged mean field relies on the particles themselves. To start the iterative process, one selects an ansatz for ϕ_i, calculates h_i and solves the resulting SCHRÖDINGER equation. This yields an improved ϕ_i. Then the procedure is started anew until the change from one step to the next become smaller than a pre-defined ε

$$\delta\langle\Phi|H^{\mathrm{eff}}|\Phi\rangle < \varepsilon, \tag{3.18}$$

which acts as a *termination condition*. Hence, a *self-consistent* solution is obtained.

Taking the HF method and one of the effective interactions, no pairing effects are accounted for. In order to do so, the HF-BCS formalism was developed. The BCS method (taken from superconductivity theory and named after BARDEEN, COOPER and SCHRIEFFER) is applied after each HF step. However, this is only the simplest implementation, as the pairing corrections are not taken into account during the variation of the ϕ_i. As an improvement, this is implemented in the HARTREE-FOCK-BOGOLYUBOV (HFB) model. Here, no longer particles, but quasi-particles are used, thus including pairing interactions between like nucleons from the beginning [74].

As the whole procedure of HFB leads to an underestimation of the binding energies for nuclei around $N = Z$ of roughly 2 MeV, a phenomenological so-called WIGNER *term* scaling exponentially with $-|N - Z|$ was introduced to correct for this [77, 78].

The most popular HFB models based on the SKYRME force are labeled HFBx with x representing the version. The most recent versions are HFB19–21 [79], which were published in 2010. The forces used with the three models are based on three different many-body interactions and thus differ slightly. In 2009, the first mass model based on the GOGNY force, called D1M, was published [80]. It is important to note that for this mass model, unlike for the HFBx mass models, no WIGNER correction is included. A comparison with respect to σ_{rms} for different mass models is shown in Tab. 3.2.

3.4.3 Mic-Mac Mass Models

A kind of quasi-standard in the field of mic-mac models is the *finite-range droplet model* (FRDM) [81, 82]. This model is based on the liquid-drop model described in Eq. (3.10) with several strong enhancements. These enhancements can be split into two parts, one on the macroscopic part of Eq. (3.10) and second, the introduction of shell corrections.

There are three different modifications of the macroscopic part: The first one is the change from the “drop model” to a “droplet model”, the second one adds finite-range surface effects and the third one is the introduction of an exponential compressibility term.

For explaining the changes when passing to the droplet model [83], it is convenient to write Eq. (3.10) as follows:

$$E_{\mathrm{mac}} = E_{\mathrm{vol}} + E_{\mathrm{sf}} + E_{\mathrm{Coul}}. \tag{3.19}$$

Each of the three summands is now modified: The volume term is modified in such a way that the incompressibility is now no longer infinite but finite. Thus, the nucleus will be squeezed by the surface tension and expanded by the COULOMB force. Mathematically, this results in the introduction of two new variables: The first one is a dilatational variable ϵ and the second one a variable describing the asymmetry between the neutron and proton density δ. These variables are used for the modifications of the surface term as well, which results here in a separate treatment of the neutron and the proton surface. The variables ϵ and δ are determined by a variational method minimizing the total macroscopic energy E_{mac}, which results also in modifications of the COULOMB term. Thus, a new macroscopic mass formula is obtained. However, within this concept, the nucleus can only have a spherical shape. In order to account for deformations, deformation factors B_i are introduced [84] which are multiplied to the different terms.

The second modification after passing to the droplet model takes into account that the nucleon-nucleon interaction is short-range and therefore has an effect on the surface energy. This modification is thus called "finite range" modification [85].

Finally, as a third modification, a phenomenological compressibility term was introduced, which corrects for the overestimation of the central density [86].

In order to perform shell corrections, a single-particle SCHRÖDINGER equation with a single-particle field U has to be solved. The single-particle field in the case of the FRDM is written as

$$U = V_0 + V_{\text{so}} + V_{\text{coul}}, \tag{3.20}$$

with V_0 being the spin-independent part, the second term V_{so} the spin-orbit interaction and the third term V_{coul} the COULOMB interaction. With this as a starting point, the variational HF method is applied similarly to the description in Section 3.4.2. In addition, corrections for the pairing interaction, an adapted WIGNER term, and a charge asymmetry term $c_a(Z - N)$ are applied.

Finally, the free parameters included in the macroscopic and microscopic part are fitted to experimental data. The resulting σ_{rms} for a fit of the latest FRDM to the AME2003 data can be found in Tab. 3.2 [82].

4 Experimental Setup

The measurements presented in this work were carried out at the ISOLTRAP experiment [27] located at the radioactive ion beam facility ISOLDE [28]. ISOLDE is based at the European Organization for Nuclear Research CERN in Geneva, Switzerland.

4.1 ISOLDE

The ISOLDE facility at CERN (see Fig. 4.1) provides a rich variety of radioactive ion beams for experiments in many different fields of physics, such as nuclear structure investigations, nuclear astrophysics, solid-state physics as well as biophysics and nuclear medicine [28, 87]. Half-lives of the produced nuclei range from infinity (stable) down to a few milliseconds. ISOLDE is based on the so-called *Isotope Separation Online* (ISOL) technique: A thick target is bombarded with light high-energetic particles which induce fission, spallation and fragmentation. The resulting particles diffuse to an ion source, where they are ionized and afterwards accelerated and mass separated.

In the case of ISOLDE, the high-energy particles are usually protons which have been accelerated to 1.4 GeV by the *Proton Synchrotron Booster* (PSB). The proton beam leaving the PSB is pulsed at a low repetition rate around 1 Hz and consists of about 10^{13} protons per pulse. The resulting mean current on the target is consequently around $2\,\mu$A. In addition to high-energy protons, neutrons can be used at ISOLDE as well. This is of particular interest if one is interested in neutron-rich fission products. The neutrons are produced by directing the proton beam instead of on the target itself on an attached high-Z metal neutron converter [88]. The neutrons resulting from spallation in the converter favor the production of neutron-rich isotopes when interacting with the target. The time structure of the produced radioactive beam varies strongly with the half-life of the contained nuclides and their release time from the target [89]. By combining different types of targets and ion sources a large variety of nuclei — ranging from very light ones like helium to heavy ones like radium — can be produced[1].

The most frequently used target material is uranium carbide (UC_x) [91], as many of the nuclides lighter than uranium can thereby be provided[2]. However, especially if aiming to produce lighter nuclei, it can be favorable to enhance their production rate by use of lighter target materials e. g. calcium oxide.

In order to ionize the produced beam, three different types of ionization techniques are available: hot surface, plasma and laser ionization. With a hot-surface ion source, mainly alkali and alkaline earth elements are ionized making use of their low ionization potential. Nuclides with a higher ionization potential, e. g. noble gases, can be ionized

---

[1] For more information on available radioactive ion beams at ISOLDE, see Ref. [90].

[2] It is important to point out that the ISOL technique based on UC_x is an extraordinary feature opening the rare possibility of PENNING-trap mass measurements in the heavy-mass region. This precious feature enabled the present measurements.

in a plasma ion source such as the *Versatile Arc Discharge Ion Source* (Vadis) [92]. However, both ion sources have the disadvantage that they are not selective to a specific element, potentially providing a beam highly contaminated with unwanted species. This issue is addressed by the *Resonant Ionization Laser Ion Source* (Rilis) [93, 94]: Here the neutral atoms are ionized with use of laser excitation via 2–3 atomic levels up to auto-ionizing states or directly to the continuum. With this technique, distinct elements or, depending on the specific case, even isotopes and isomers can be selected. In addition, the beam composition can be easily manipulated by blocking or unblocking the laser beam. Unfortunately, even when using laser ionization, one has to deal with contaminations due to additional surface ionization. Thanks to the advantage of selectivity, Rilis is meanwhile the most commonly used ion source at Isolde [91]. However, excitation schemes are not available for all elements. Consequently, the choice of the ion source depends on the desired element.

After ionization, the ions are accelerated up to 60 keV for transport purposes. In order to separate them by their charge-to-mass (q/m) ratio, two magnetic separators, the *General Purpose Separator* (Gps) with a mass resolving power $m/\Delta m \approx 500 - 800$ or the *High Resolution Separator* (Hrs) with a resolving power $m/\Delta m \approx 2000 - 6000$ [95], can be used.

Following the mass separation, the beam is distributed to the different experiments. The beam distribution system comprises only electrostatic ion-optical elements to ensure a mass-independent beam transfer. This allows a quick change of the ion of interest during a measurement campaign as only the magnetic separators have to be adjusted.

4.2 ISOLTRAP

The mass spectrometer Isoltrap is dedicated to mass measurements of short-lived nuclides with half-lives ranging down to some tens of milliseconds and intensities down to a few tens of ions per second [27]. Depending on half-lives, intensities and available beam time, a relative precision of down to 10^{-8} and in some cases even better can be reached. Isoltrap consists of four traps of different type (see Fig. 4.2), with three traps dedicated to beam preparation and one trap to mass measurements. For the detection of the ions, several *multi-channel plate* (Mcp) detectors [97] are implemented along the beam line. They are used for beam diagnostics as well as for the actual determination of the cyclotron frequency. In addition to the online beam from Isolde, Isoltrap uses two offline ion sources, one alkali ion source, producing mainly ^{133}Cs, ^{85}Rb and ^{39}K, and one laser ablation source for the production of carbon clusters [98] or other nuclides suitable for laser ablation [99].

4.2.1 Beam Preparation

In order to perform the actual mass measurement, the beam delivered by Isolde (or one of the offline ion sources) has to be prepared with respect to its time structure, emittance, and composition.

The first step in this preparation process is a buffer-gas-filled radio-frequency (Rfq) trap [100], which is referred to as *buncher*. The purpose of the buncher is to stop, accumulate and cool the up to 60 keV beam. In order to stop and accumulate the

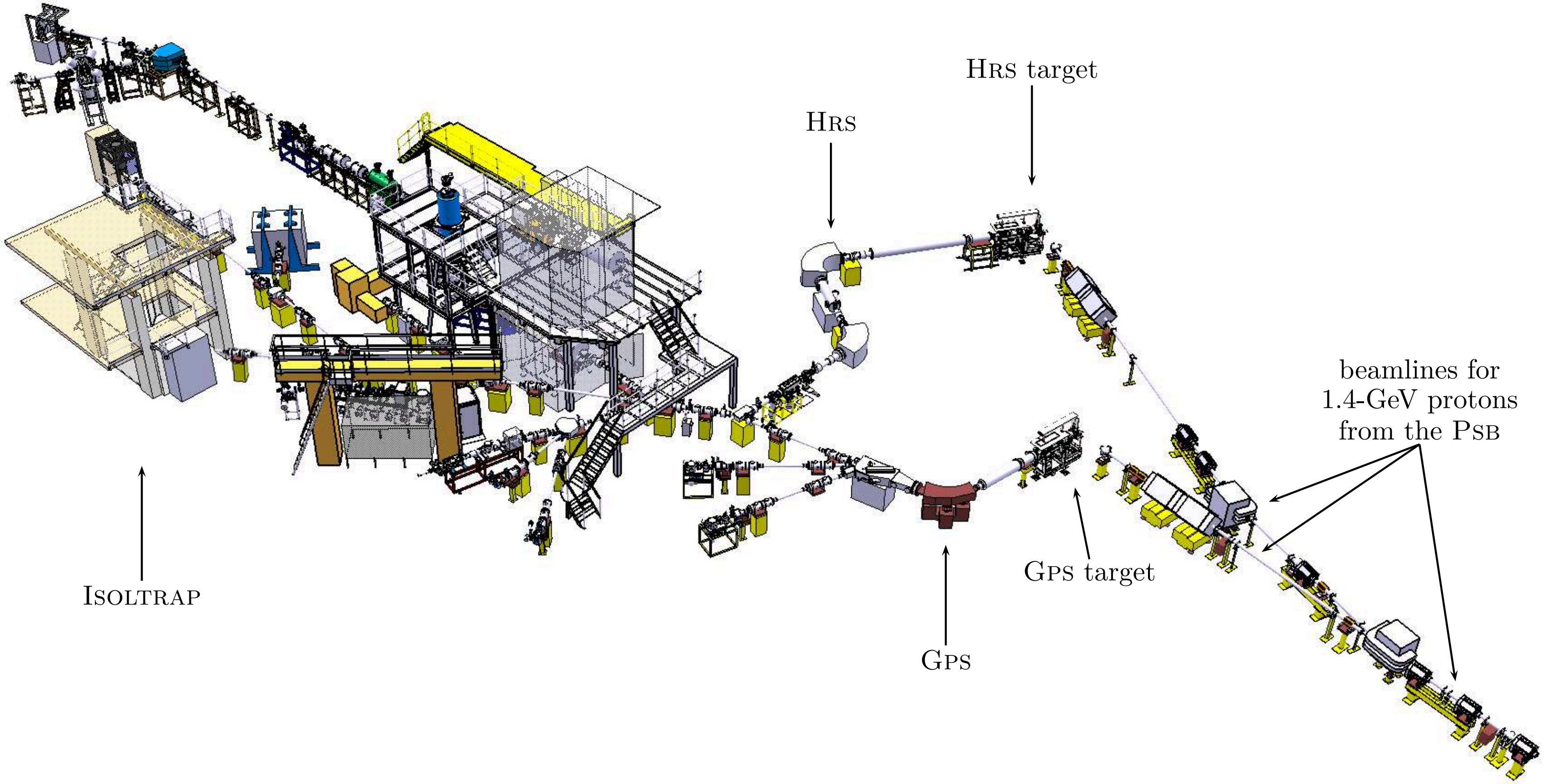

Figure 4.1: *(Color) Overview of* Isolde. *The radioactive ion beam is produced by first directing a* 1.4*-GeV proton beam coming from the Proton Synchrotron Booster (*Psb*) to one of the two targets. The nuclides consequently resulting from fission, fusion and fragmentation are then ionized, mass separated using the* General Purpose Separator *(*Gps*) or the* High Resolution Separator *(*Hrs*) and distributed to the different experiments.* Isoltrap *is located at the end of the central beamline. Adapted from Ref. [96].*

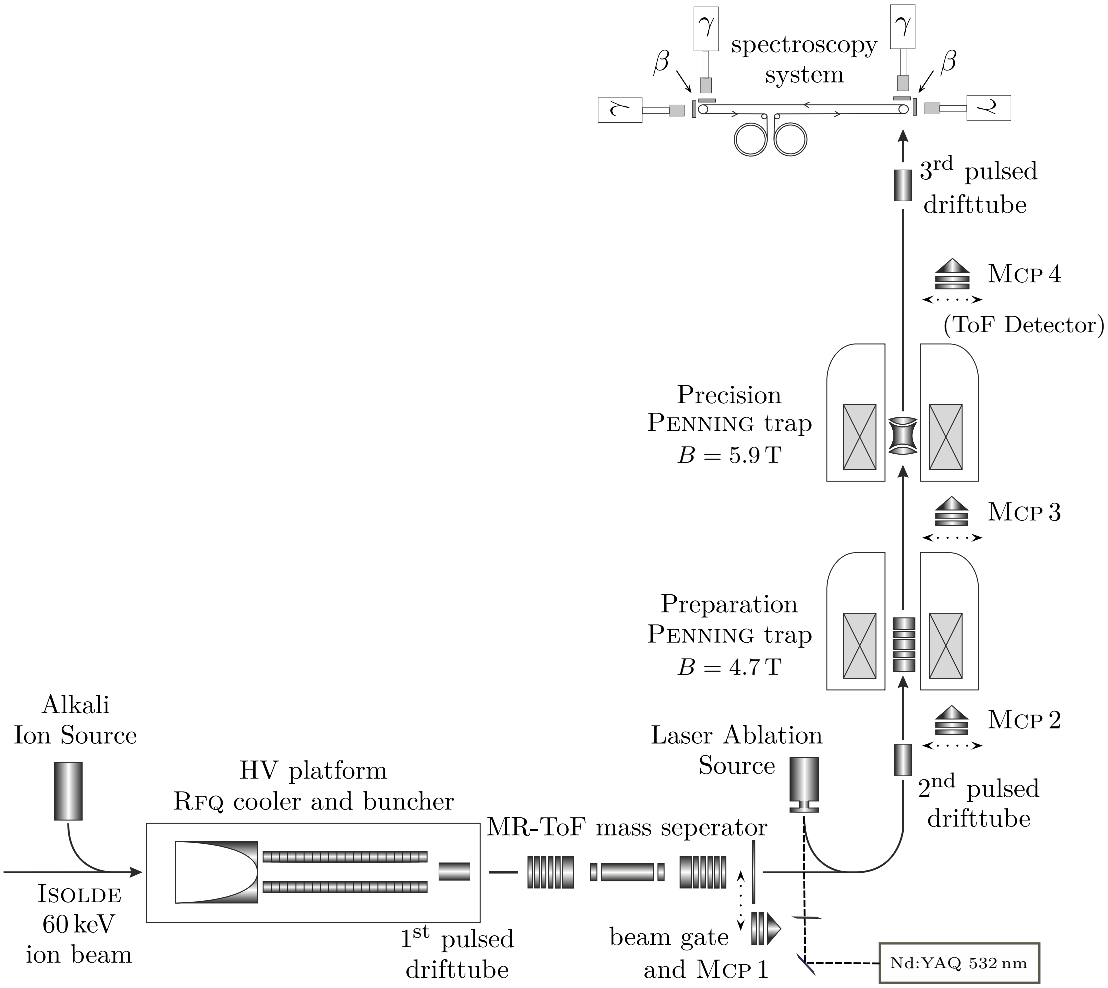

Figure 4.2: *Schematic drawing of the* ISOLTRAP *setup. The ion beam is stopped, accumulated and cooled in the* RFQ cooler and buncher *and cleaned in the* MR-ToF mass separator. *Further cleaning and cooling can be done in the* preparation PENNING trap. *In between, two* pulsed drift tubes *reduce the beam energy. Subsequently, either a mass determination using the* precision PENNING trap *is performed or the beam is (if necessary) further cleaned, re-accelerated by a pulsed drift tube and sent to the* spectroscopy system. *Instead of* ISOLDE *beam, ions from the* alkali ion source *or the* laser ablation source *can be used. Several movable* MCPs *are used for ion detection.*

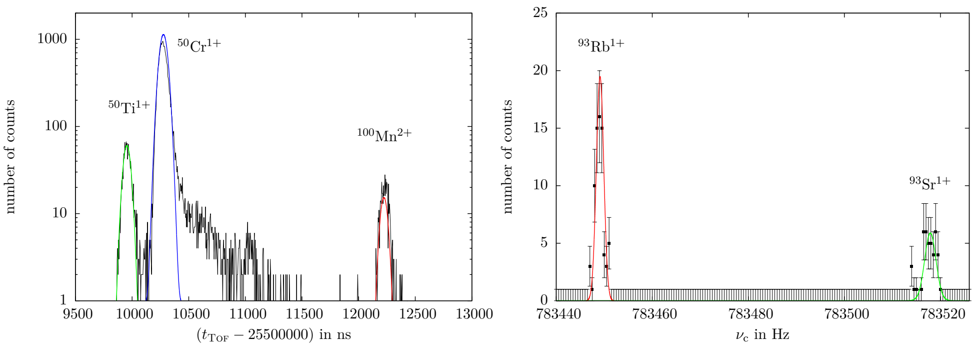

(a) **(b)**

Figure 4.3: *(Color) Selection of isobars during beam preparation. (a) In the* Mr-Tof*, isobars separate by time of flight and can be selected by switching a beam gate at the corresponding time. Here, $^{50}Ti^{1+}$, $^{50}Cr^{1+}$ and $^{100}Mn^{2+}$ are shown as an example (*Mcp *1, see Fig. 4.2). (b) In the preparation* Penning *trap, isobars can be selected depending on the cyclotron frequency ν_c. Here, the isobars $^{93}Rb^{1+}$ and $^{93}Sr^{1+}$ are shown as an example (*Mcp *3).*

beam, the buncher electrodes form a trapping potential with a common voltage offset corresponding to the beam energy. Improving the emittance of the beam is achieved by two means: First, buffer-gas cooling using helium gas at a pressure on the order of 10^{-3} mbar (similar to the technique described in 2.3) is used for reduction of the energy and the energy spread. Secondly, an rf signal is applied for radial confinement. It is thus possible to achieve a transverse emittance of $\epsilon_{\mathrm{trans}} \approx 10\pi\,\mathrm{mm\,mrad}$ and a longitudinal emittance of $\epsilon_{\mathrm{long}} \approx 10\,\mathrm{eV}\,\mu\mathrm{s}$. Once the accumulation and cooling of the beam is sufficient, the last electrodes are switched to a lower potential to eject the beam. A following pulsed drift tube sets the beam energy to around 3 keV.

After the ejection from the Rfq, the beam is transferred to the *multi-reflectron time-of-flight (*Mr-Tof*) mass separator* for removal of unwanted species, which was newly installed in 2010 [101, 102]. For the removal of unwanted species, the particles are trapped between two sets of electrostatic mirrors and reflected multiple times. As all particles ejected from the buncher have roughly the same energy, particles with different mass separate in time and space due to different velocities (see Fig. 4.3 a). After the ejection from the Mr-Tof mass separator, the ions of interest are selected by switching a beam gate at the corresponding time of flight. With this whole process taking some few milliseconds, a resolving power on the order of 10^5 is achieved.

Following the beam cleaning in the Mr-Tof purification system and a further decrease of the beam energy to about 100 eV by a second pulsed drift tube, the beam is transferred to the first, cylindrical Penning trap, often referred to as *preparation trap*, which is placed in a 4.7-T superconducting magnet. Here, additional cleaning and cooling using the mass-selective buffer-gas cooling technique (see Section 2.3 and [36]) can be performed. Helium at a pressure of $10^{-3} - 10^{-4}$ mbar is used as a buffer-gas. At this pressure, isobars can be selected within a few hundred milliseconds with a resolving power of $10^4 - 10^5$ as shown in Fig. 4.3 b. For short-lived species, this process can be shortened thus accepting a lower resolving power. After these steps, the beam, now with an energy around 10 eV, is injected into the mass determination part of the setup.

4.2.2 Mass Determination

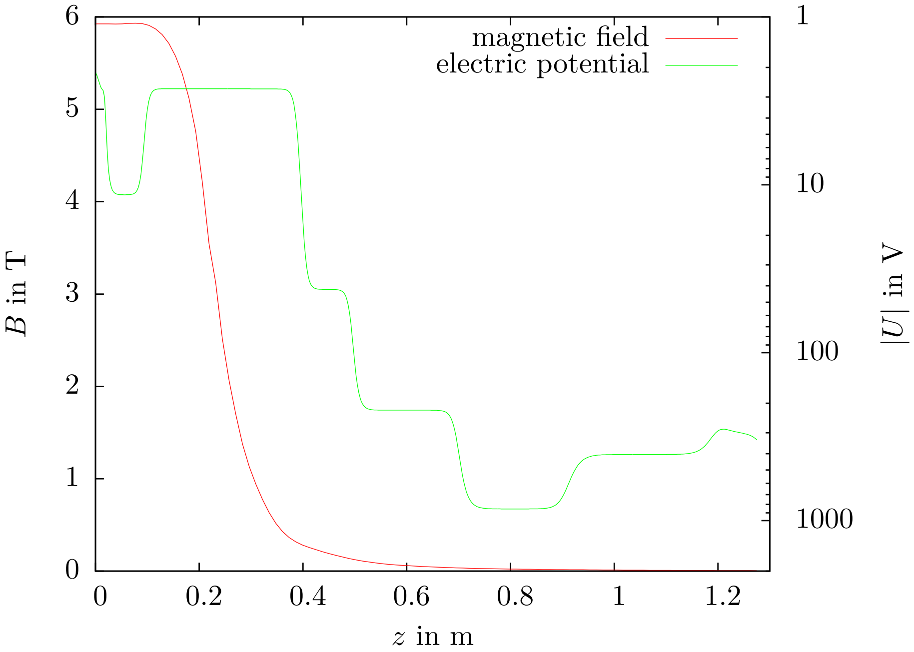

Figure 4.4: *(Color) The distribution of the magnetic field and electric potential from the center of the trap along the beam axis towards the* MCP *detector. The magnetic field distribution is based on measurements and the electric potential has been extracted from a* SIMION *[103] simulation based on the potentials applied to the different electrostatic elements. In the region with the largest magnetic field gradient (≈ $0.1 - 0.4$ m) the particles are kept at a low energy to ensure a good conversion of the radial energy into axial energy. Afterwards, the ions are accelerated and focused onto the* MCP *detector.*

The mass determination part of ISOLTRAP consists of the second PENNING trap, referred to as *precision trap*, and the drift region towards a *multi-channel plate* (MCP) detector [97].

The precision trap is a hyperbolic PENNING trap and placed in a 5.9-T superconducting magnet. As a last step of beam preparation, dipole cleaning can be performed here with a resolving power of up to 10^6 in case of unwanted isomeric states or other nuclides which are close in mass to the nuclide of interest. After the final cleaning, the TOF-ICR technique (see Section 2.4 and [38]) is used to determine the cyclotron frequency. In order to maximize the time-of-flight effect, sufficient time has to be ensured for the conversion of the radial energy of the ions into axial energy in the region with the largest magnetic field gradient. This is achieved by keeping the electric field at a low value in this region (see Fig. 4.4). The recorded time of flight is the time it takes the ions to reach the detector in about 1.3 m distance after they are ejected from the trap. The typical acquisition time is $0.5 - 2$ ms. Using a multi-channel scaler (MCS) with 1024 channels (bins), this results in a time resolution (bin size) of around $0.5 - 2\,\mu$s. Usually one aims at around one ion per cycle to reduced space-charge effects. A typical time-of-flight resonance as shown in Fig. 4.5 requires at least some hundred ions and takes in the order of 30 min.

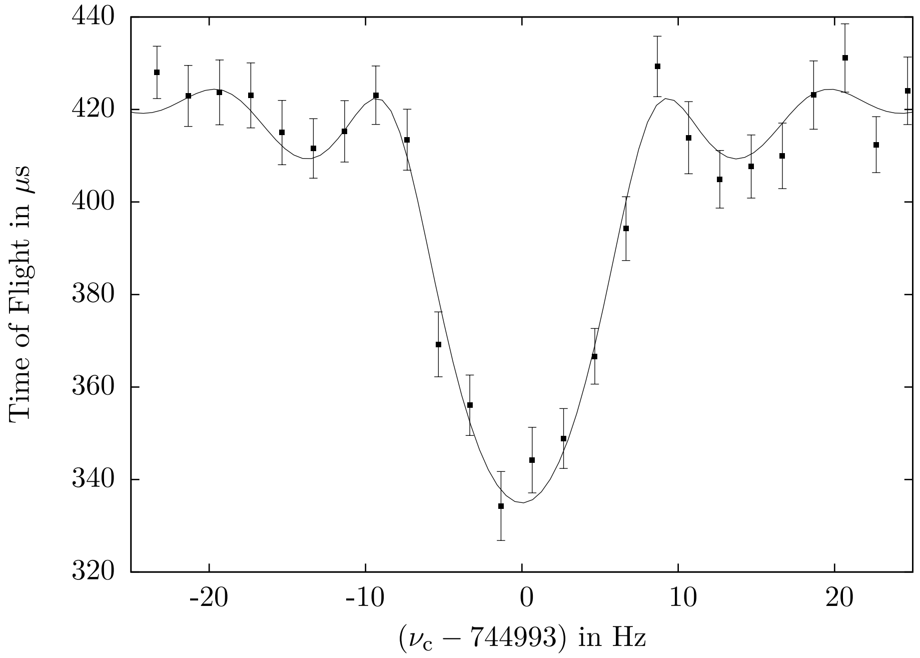

Figure 4.5: *A time-of-flight resonance of* $^{122}Ag^{+}$. *The solid line is a fit of the theoretical line shape to the data points based on Eq. (2.23).*

4.2.3 Decay Spectroscopy

In order to broaden the possibilities of ISOLTRAP in the field of mass measurements, in 2009 a *decay spectroscopy system* was added on top of the experimental setup [104, 105] (see Fig. 4.2).

To allow an efficient spectroscopy, the ions are re-accelerated after the ejection from the precision PENNING trap and then focused onto a movable tape. Detection of β or γ particles resulting from the decay of the implanted ions is achieved with use of several β and γ detectors either directly at the implantation point or after moving the tape to a different position. The later place is chosen for the measurement in case of long-lived nuclei to use the time more efficiently: It allows a measurement taking place while at the same time new particles are collected at the implantation point. The use of several detectors at the same time, as seen in Fig. 4.2, is favorable, as thus coincidence spectra can be obtained. Consequently, the background is significantly decreased.

By observing decay properties like β and γ transitions at ISOLTRAP, two different approaches are possible: *decay-spectroscopy-assisted mass measurements* and *trap-assisted decay spectroscopy*. The main difference between the two is the focus of the measurement: In the first case, "normal" mass measurements are performed at ISOLTRAP and, in addition, the decay system is used to identify the measured species more precisely based on decay properties, e. g. by identifying whether a nuclear ground state or isomeric state is present. This is interesting since in the case of close-lying isomers, with an energy difference on the order of several tens keV, it is usually not possible to resolve them by using the standard mass-determination procedure. Consequently, during the data analysis (see Section 6.1), a mixture of both states has to be assumed, resulting in a significant increase in uncertainty of the determined mass. This increase can be avoided if the relative intensities of the isomeric states are determined in the spectroscopy system.

In the second case, the ISOLTRAP setup as a whole is used for beam preparation and purification. Thus, a clean radioactive ion ensemble can be provided to the spectroscopy setup for decay studies, resulting in a significant reduction of isobaric and isomeric background [105, 106].

In the context of this work, the spectroscopy system was only used in the first mode, i. e. assisting mass measurements.

5 The ISOLTRAP Control System (CS)

The complexity of the ISOLTRAP setup as discussed in Section 4.2 makes it indispensable to use a computer-based control system for the operation of the experiment: The whole experimental cycle has to be synchronized with a precision down to several tens of nanoseconds and several hundred different parameters like voltages, buffer-gas pressures, frequencies and voltage amplitudes have to be set and controlled. Furthermore, it is necessary to save and reproduce parameters once a good set has been found. Finally, the measurement data have to be acquired and stored.

The ISOLTRAP control system is based on the *CS framework* (see Section 5.1) [107], which has been developed and maintained by the *Experiment Elektronik* (EE) group at the GSI Helmholtzzentrum für Schwerionenforschung GmbH in Darmstadt, Germany. To derive a control system from the CS framework, experiment-specific components have to be added:

$$\text{control system} = \text{CS framework} + \text{experiment-specific components}.$$

The maintenance and further development of the ISOLTRAP control system was one of the main technical tasks carried out in the context of this thesis. Hence, its current design is described below in greater detail. First, an overview of the CS framework is given. Second, the ISOLTRAP adaption of the CS framework including components specific to the experiment is presented. Finally, the enhancements achieved in the context of this thesis are reported.

5.1 The CS Framework

The CS framework is based on the graphical programming language *Lab*VIEW developed by National Instruments (NI). To allow an easy use and further development, the CS framework has been published online [108] under the free *General Public License* GPL [109]. It is widely used at many different experiments apart from ISOLTRAP like e. g. SHIPTRAP [26], TRIGATRAP [110], WITCH [111] and HITRAP [112]. At present, the largest implementation is located at the high-energy laser system PHELIX [113].

As a basic communication layer between different instances of the control system, the DIM (*Distributed Information Management*) protocol [114, 115] is used. Apart from the core (or main part) of the CS framework, which is handling the control of the experimental hardware and the data acquisition, several small sub-projects have been programmed for the management of the control system itself.

5.1.1 The Basic Communication Layer: DIM

Usually, a control system is distributed over several different machines (nodes). This is aimed at improving the reliability (a breakdown of one node should not take down the whole control system), the availability (in case of a breakdown of one node, services can be transferred to another node), the performance (less tasks for each node) as well as the flexibility of the control system (different hardware architectures may be needed for different tasks). However, this approach poses the challenge to ensure a proper communication between the different nodes, which is especially difficult if they are based on completely different hardware architectures or operating systems.

For this purpose, the CS makes use of the Dim (*Distributed Information Management*) protocol [114, 115]. It was originally developed for the communication within the Delphi experiment at Cern and is nowadays widely used at the Lhc (see e. g. Refs. [116, 117]).

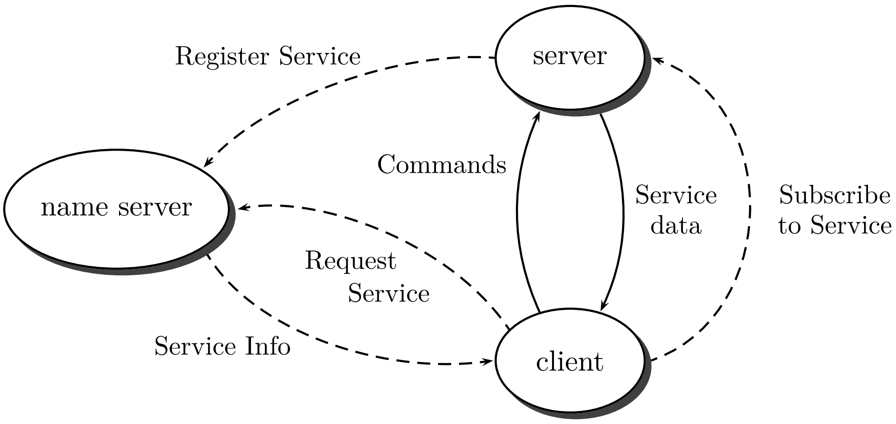

Figure 5.1: *Dataflow within* Dim*, the communication layer between different components of the control system. Services are registered and service information are requested at the* name server*. After a* client *has subscribed to a service, the transmission of data takes place between the server and the client directly. When using a monitored service, the transmission of data is initiated by the server and therefore only takes place if the service data is updated. Clients in turn can send commands to the server to trigger predefined actions. This concept is called* event-driven communication.

In order to achieve a performance, reliability and availability as high as possible, Dim omits a central server managing all the data. Consequently, a peer-to-peer communication is used (see Fig. 5.1). An important concept within Dim is a *(named) service*. A service is defined as a set of data with a name associated to it. Each service is offered by a *server* and can be requested by an interested *client*. In a typical control system, the update rate of services varies strongly: Some service data change within seconds or even less while other data remain constant for hours or days. As means to reduce network traffic and computing power, it is therefore often desirable to update data on the clients only when necessary. Using a *monitored* service within Dim, data are hence not requested (or *polled*) by the clients at a constant interval, but are sent by the publishing server to the subscribed clients only when they have changed.[1] From the client side, *commands* can be send to the server to trigger a predefined action.[2] This is referred to as *publisher-subscriber concept* or *event-driven communication*.

To reach a high availability, it should be possible to transfer services from one server to another in case of a breakdown. For realizing this concept, a *name server* has been introduced. It keeps track of all servers and services offered as well as all clients subscribed to them. On start-up, a server registers its services at the name server and clients request information about the required services therefrom. Afterwards, the distribution of data is independent from the name server and dealt with directly between the server and the client. In case of a problem, each component (name server, server and client) can be transferred to a different location and/or restarted without leaving an inconsistent system and disturbing the remaining components.

For the integration of DIM into LabVIEW, an interface has been provided by GSI and can be found online [118, 119].

5.1.2 The Core of the CS Framework

The core of the CS framework is programmed in the graphical programming language LabVIEW [120]. LabVIEW has been chosen for several reasons: First, its basic concepts are easy and fast to learn, which is especially important in case no long-term manpower is available for maintenance of the control system. Second, many hardware interfaces are supported by LabVIEW by default and many manufactures already provide device drivers for LabVIEW. This reduces the integration time of new devices significantly. Third, LabVIEW is by default multi-threaded and thus the available CPUs are used efficiently without special attention from the programmers side. For the actual implementation as a control system, the code programmed in the *NI Development Environment* is compiled into executable files using the *NI Application Builder*.

To allow a reasonable scaling of the control system for growing experiments, an object-oriented approach has been realized within the CS framework (see Fig. 5.2)[3]: Each type of hardware device is represented by a *class*, which can inherit common features from a parent class: For example, all frequency generators share the possibility to set and read a frequency and an amplitude. Thus, these methods are already basically implemented in a base class called *AfgBase*[4]. Within the derived class *DS345*, representing a special type of frequency generator, the DS345 from Stanford Research, these methods only have to be adapted accordingly. This reduces the development time significantly. During runtime[5], for each hardware device an object is created from its corresponding class.

---

[1] In case the update rate of a service is very high, this approach may exceed the available computing resources. Therefore, a further type of service is available within DIM: a *timed* service. Here, the service is updated by the server at a regular time interval. Thus, a constant load can be ensured. However, within the CS framework this type of service is not used.

[2] Within DIM, a command is a special type of service.

[3] The object oriented approach used within the CS framework had been engraved on top of basic LabVIEW. Starting with LabVIEW 8.20, NI has implemented its own object-oriented approach, called LVOOP. The object-oriented approach within the CS framework is quite different and thus LVOOP is currently not used in the main CS code.

[4] *Afg = Arbitrary Function Generator*

[5] *Runtime* denotes the time a computer program (in this case the control system) is being executed.

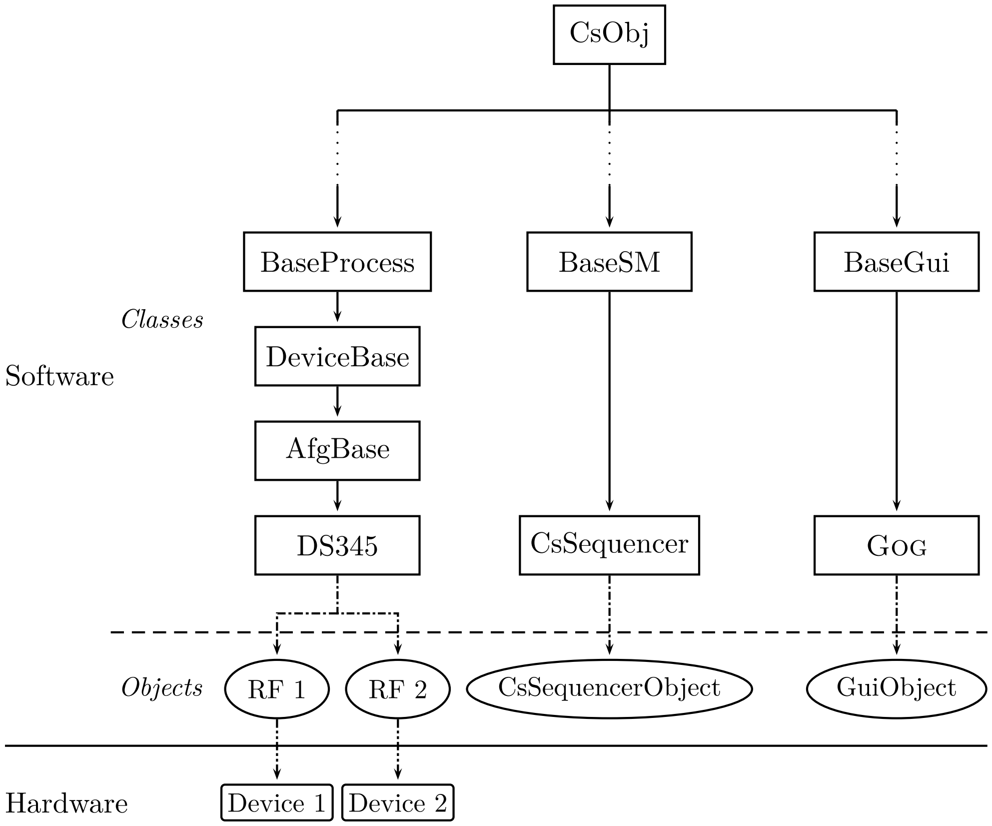

Figure 5.2: *Sample excerpt of the hierarchy within the CS with the parent–child relations being denoted by solid arrows. The base class is* CsObj*. Further down in hierarchy, one finds the* BaseProcess*, which passes on down to* DS345*, a class describing a specific type of frequency generators (SR DS345). During runtime,* objects *of this class (RF 1 and RF 2) are created controlling the connected hardware devices (Device 1 and Device 2). For controlling the sequence of an experimental cycle, a sequencer (*CsSequencerObject*) is used which is based on a state machine (*BaseSM*). For the visualization of values a* Graphical User Interface *(*Gui*) is necessary, here called* GuiObject.

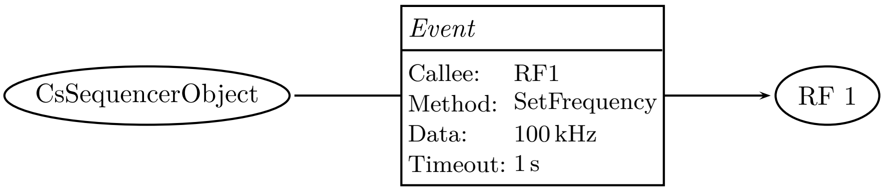

Figure 5.3: *Within the CS, objects communicate via events with each other. An event contains the name of the target object, the method to be called, the data and timeout information. In this example, the sequencer object sends an event to a frequency generator object to set a frequency.*

Three types of objects commonly occur within the CS: objects corresponding to hardware devices, a sequencer object to control the experimental cycle, as well as GUI objects for displaying and controlling parameters. A special type of GUI object, the *General Object* GUI (GOG) can be used to manage all the other GUIs which control the respective devices.

The communication between different objects is based on *events*. An event contains the name of the called object, the method to be executed, the data and a timeout information (see Fig. 5.3). Events in turn are realized via DIM: An event for setting e. g. a new frequency value results in a DIM command being sent to the responsible server. Once the command is processed by the server, the corresponding (frequency) values are changed. This change of values triggers the next event: Updated service data are being sent to the subscribed GUI(s). Therewith, all kinds of parameters necessary within the control system can be set and read and furthermore, objects can be created or destroyed. It also ensures a transparent change of devices in case of a breakdown, as only the name of the targeted object has to be replaced.

5.1.3 Management of the Control System

Three different types of management are used for the operation of the control system: the *process management* taking care of the processes (programs) necessary for the operation of the control system, the *configuration management* providing the configuration data for the control system objects and the *settings management* coping with the device settings.

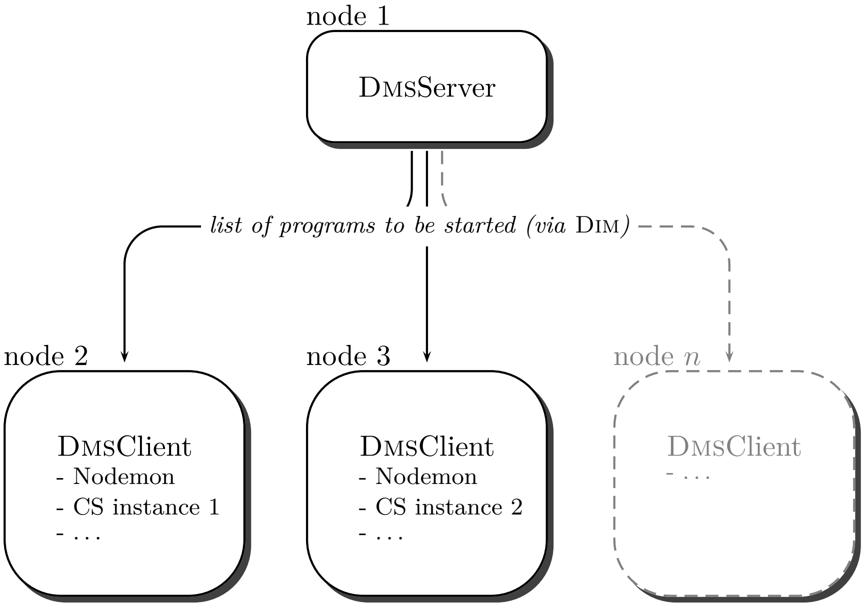

Figure 5.4: *CS process management using the* DMS*. The* DMS*Server holds a list of programs to be started and distributes this list via* DIM *to the clients. The clients in turn (re-)start, stop or kill the corresponding programs, e. g. the different instances of the control system or a small program for collecting information about the nodes called* NODEMON.

Process Management In order to manage the startup and monitoring of all control system instances (and other programs necessary for the control system), the *Domain Management System* (DMS) [121] is used at ISOLTRAP (see Fig. 5.4): A DMS*Server* publishes a list of programs to be started on the different nodes of the control system via DIM. On each node, a DMS*Client* reads the list dedicated to its node and (re-)starts, stops or kills the respective processes.[6]

Information about the individual nodes like memory consumption, CPU usage, running processes etc. are published via DIM by a small program called NODEMON [122] running on each machine. It has been inspired by the program PCMON, which serves a similar task and was developed together with DIM at CERN. The published data can be used to monitor the nodes and the control system, e. g. with the so-called DMS*Viewer*.

Configuration management The configuration information of all possible control system objects (their names, the corresponding classes, timeout settings, interface settings of the connected devices, etc.) are stored in a database, which is realized as a MICROSOFT ACCESS database. In case an object is being created, the different instances of the CS query this data via the so-called SQL*Server* [123], which reads the database using the *Structured Query Language* SQL.

Settings management When using the standard GOG for managing the objects, a list of all these objects, the used methods as well as their nominal values can be saved and reloaded using XML (*Extensible Markup Language*) settings files. This allows an easy and automated creation of the control system objects and setting of the desired method values at the start-up of the control system instance.

5.2 The CS at ISOLTRAP

The use of the CS framework at ISOLTRAP started in 2003 when it replaced an outdated VME-based control system [124]. Currently, the ISOLTRAP control system is distributed over six PCs running Microsoft Windows XP. A (decoupled) seventh PC has been set up for control-system development.

Two different categories of devices have to be controlled via the control system: slow, not time-critical devices — like power supplies and gas controls — and time-critical (or *real-time*) devices, which have to fulfill their tasks — like switching a voltage, starting a frequency generator or acquiring data — within a given time interval in the sub-microsecond range. While the handling of the slow devices as well as the configuration of the time-critical devices is performed via non-real-time standard equipment like PCs and their corresponding interfaces, the starting and stopping of the time-critical devices are realized using a real-time *timing generator* also referred to as *Pulsed Pattern Generator* (PPG, see Section 5.2.1).

As described in Section 2.4, the acquisition of a time-of-flight resonance at ISOLTRAP requires variation of the cyclotron excitation frequency in the precision trap and recording of the corresponding ions' time of flight. Each measurement consists of *cycles* and

---

[6] The list of programs is published as a DIM service by the DMSServer. The DMSClient subscribes to this service as shown in Fig. 5.1.

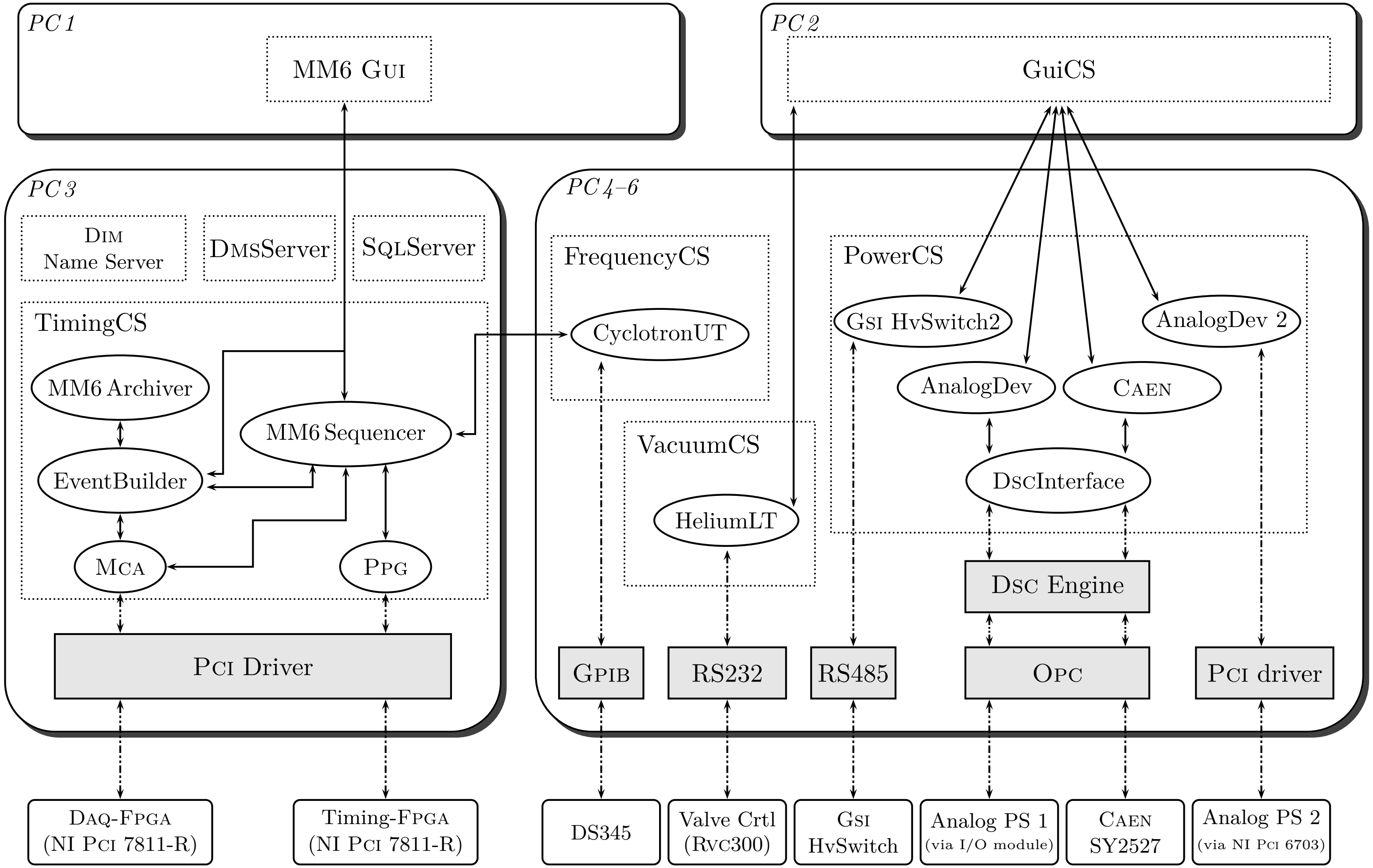

Figure 5.5: *Simplified communication scheme of the* Isoltrap *control system during the acquisition of a time-of-flight resonance. The experimental cycle is configured via the* MM6 Gui*, which passes the information to the sequencer. The sequencer configures the necessary devices and hands over to the timing generator (*Ppg*). After the timing cycle is finished, the sequencer requests the* EventBuilder *to obtain and bundle the data which have been acquired by the* Mca*. These data are then written to a file by the* MM6 Archiver *and displayed for online analysis by the* MM6 Gui*. Parameters not changed within the experimental cycle are configured using the* GuiCS*. The communication between the control system objects (ellipses) and the experimental hardware (rounded boxes) is realized via a driver layer (gray boxes).*

scans: With each experimental cycle a TOF for a given frequency value is obtained. A bunch of cycles with different frequency values (typically around 41) form a scan. For a *measurement*, each scan is repeated several ten times until a sufficient number of data points has been collected.

A simplified communication scheme for a TOF measurement can be seen in Fig. 5.5: The configuration of the timing cycle and of the scan parameters (start/end values and step-size) is entered into the *MM6* GUI (see Section 5.2.3) which passes the information to the *MM6 Sequencer*. The sequencer configures the required devices like the frequency generators for the excitations, the timing generator and the MCA (*Multi-Channel Analyzer*) for data acquisition. Then it hands over to the timing generator. After the timing generator reports one timing cycle to be finished, the sequencer calls the *Event-Builder* which reads the data from the DAQ device and publishes them via DIM. From time to time the data are read by the *MM6 Archiver*, which writes them in binary and compressed format to a file. Furthermore, the data are displayed by the MM6 GUI for online analysis. Then the sequencer starts the next sequence (i. e. with a new frequency value). This loop can be stopped (or aborted) via the MM6 GUI. Parameters of devices which remain unchanged during a measurement, like voltages or gas-pressures are not included in the MM6 GUI. They are configured in advance via the *GuiCS*, an instance of the CS running a GUI *object*. For the communication between the control-system objects and the experimental hardware, a (third-party) driver layer depending on the respective interface is used.

5.2.1 Real-Time Applications

Real-time applications require an answer to a command within a specific time. At ISOLTRAP, this time limit lies on the order of several tens of nanoseconds. Most of these real-time applications are implemented in hard-wired circuits within the corresponding devices and triggered via a TTL signal (switches, frequency generators, data acquisition). Generating the sequence of all TTL signals (the *timing pattern*) is achieved using a *Pulsed Pattern Generator* (PPG) based on an FPGA (*Field Programmable Gate Array*) card [125, 126] with a 40 MHz clock (NI PCI 7811-R). Thus, a time resolution down to 25 ns can be achieved. The communication with the non-real-time part of the control system is realized via the PCI bus. A typical timing pattern of the experimental cycle when using ISOLDE ion beams is visible in Fig. 5.6: After the sequencer hands over the control, the timing generator waits for an external trigger to start the cycle. This trigger is either related to the proton impact on the ISOLDE target or (in less time-critical cases) produced by a frequency generator. Following the trigger signal, the pre-configured timing pattern is generated. The times for each step are adapted to each nuclide of interest individually resulting in a typical timing-cycle length of $0.3 - 4$ s. After the timing cycle is finished, the timing generator reports the end of the cycle to the sequencer and stops. If a measurement is performed using one of the ISOLTRAP offline ion sources, the timing pattern is adapted to the specific requirements of the corresponding source.

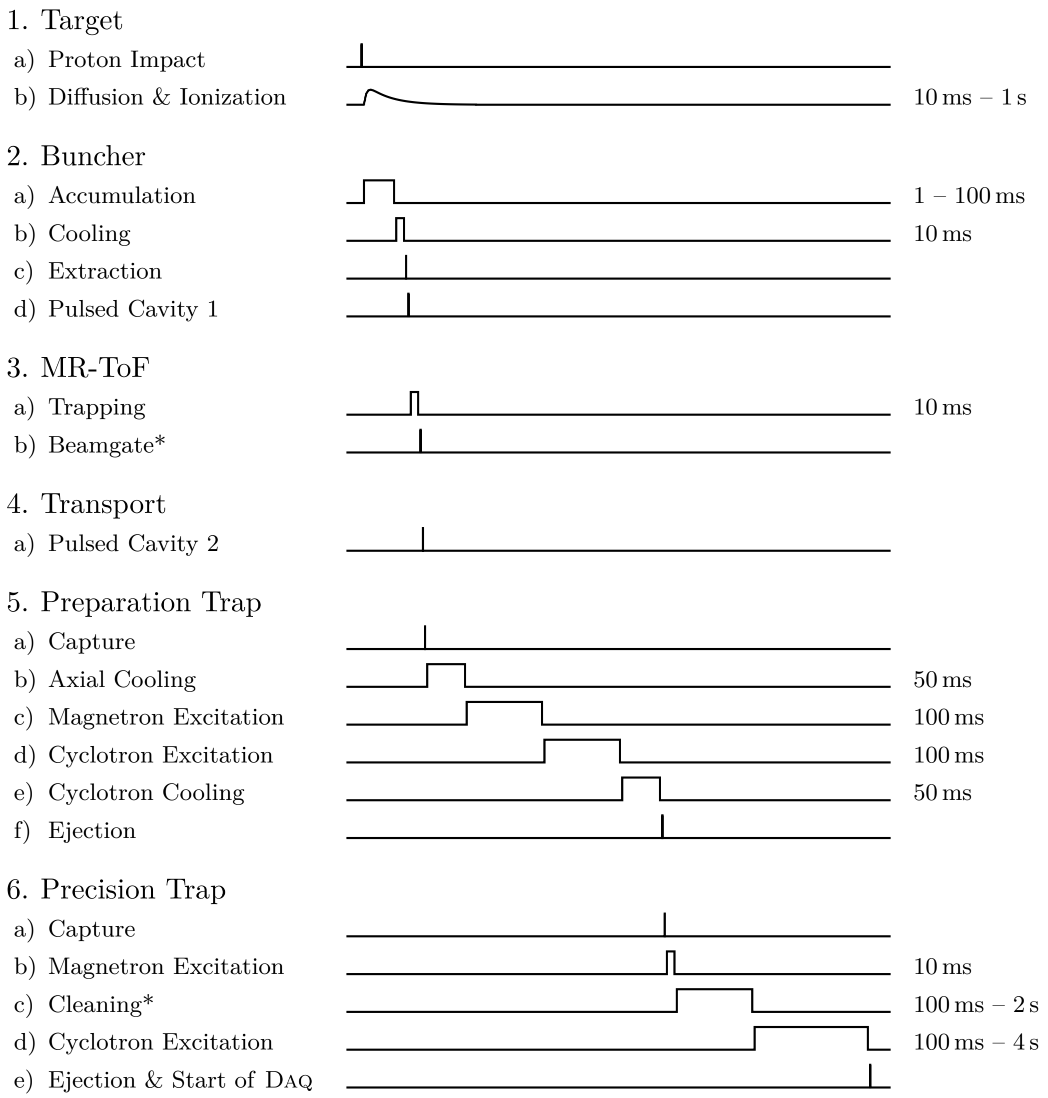

Figure 5.6: *Simplified typical timing pattern of* ISOLTRAP *for a measurement using beam from* ISOLDE. *The cycle is triggered by the proton impact on the* ISOLDE *target or (in less time-critical cases) by a frequency generator. The given times reflect the order of magnitude for the corresponding item and are usually adapted to each nuclide individually. Items marked with an asterisk (*) are only used if necessary. For a measurement using one of the* ISOLTRAP *offline ion sources, the timing pattern is adapted accordingly.*

5.2.2 Non-Real-Time Applications

In contrast to the real-time applications, which need to react within a given time frame, for many applications the speed of execution of commands is not a critical value: A varying reaction time in the order of several tens of milliseconds or even more is sufficient. They are referred to as *non-real time applications* and include at ISOLTRAP tasks like setting a voltage or gas pressure as well as the configuration of real-time applications. Non-real-time communication can be achieved by means of standard PC equipment. For these tasks, a variety of different connections is used at ISOLTRAP, including PROFIBUS, Ethernet, OPC, GPIB, RS232, RS485 and USB. For the communication with the devices necessary for the operation of the buncher potential-free connections are essential as these devices are floating on high voltage. Hence, a set of fiber-optical connections is deployed.

5.2.3 MM6 — the GUI for Mass Measurements

As a remain from the VME-based control system, an (adapted) *Graphical User Interface* (GUI) written in C++ is used for the configuration of the sequencer and for online analysis of the acquired data. It is named MM6 referring to *Mass Measure* version 6 and serves two purposes: First, it sends the configuration data for the experimental cycle (timing pattern, frequency values for the excitations and scans to be performed) via DIM to the sequencer and starts/stops the sequencer. Second, it reads the measured data via DIM from the EventBuilder and displays them for online analysis including the possibility of simple fits.

For a detailed offline analysis of the recorded data, an evaluation program called EVA is used, which is also written in C++ in analogy to MM6.

5.3 Further Development of the ISOLTRAP Control System

The integration of the MR-TOF mass separator (see Section 4.2.1) and the decay spectroscopy setup (see Section 4.2.3) required, apart from their physical integration into the ISOLTRAP setup, a further development of the ISOLTRAP control system, which was done in the context of this thesis. Apart from the integration of the required power supplies and the integration into the timing cycle, a new experimental procedure, the so-called *stacking mode*, has been realized to fully exploit the potential of the MR-TOF mass separator.

Integration of MR-TOF Mass Separator and Decay Spectroscopy Setup For the integration of both systems into the experimental timing cycle, a modification of the MM6 sequencer became necessary: in the version used up-to-now, the number of different timing channels was limited to 16, whereas for the operation of the new parts additional trigger channels were needed. Hence, the number of available channels has been increased to 32. The modification should allow the use of up to 48 channels, but this has not been tested as 32 channels are sufficient for the current requirements.

Stacking In order to use the Mr-Tof mass separator most efficiently, a possibility to separate the timing cycle into two sub-cycles (each comprising 16 channels) and repeat each sub-cycle multiple times has been introduced into the *MM6 Sequencer* as a second step. This concept opens the possibility of so-called *stacking operation*: Here, the first part of the cycle (steps 1. a)–5. b) in Fig. 5.6) is repeated multiply before the remaining timing pattern is executed. This leads to an accumulation of ions in the preparation trap. Afterwards, they are cooled and (further) cleaned, and then transferred as a bunch into the mass determination part of the setup. In case part of the necessary beam purification can be done with the Mr-Tof mass separator and the half-life of the ion of interest is long enough, this allows, together with enhancements of the experimental hardware[7], to deal with a higher amount of unwanted ions at Isoltrap and furthermore to reduce the measurement time significantly. This feature has been successfully used in 2012 to perform measurements like the determination of the mass of ^{82}Zn, which would not have been possible otherwise [127].

5.4 Additional Improvements of the ISOLTRAP Control System

In addition to the extensions of the control system already described in Section 5.3, several further improvements have been realized in the context of this thesis, including changes in the administration of the computers, integration of new devices, and programming of new CS classes. These enhancements are described below.

5.4.1 Enhanced Computer Administration

The maintenance of the control system PCs has been improved by customizing the *Computer Management Framework* (Cmf) used at Cern [128, 129]. Although originally developed for the management of control systems PCs, Cmf quickly became the state-of-the-art management tool for all Windows computers at Cern. It allows grouping of computers, performing automated actions like installing applications (including Windows updates) and reinstalling PCs automatically with the same applications as before. Using Cmf, updates are regularly deployed by the Cern IT department to keep the operating system and the installed applications secure and up-to-date. As in the Cmf standard configuration the installation of these updates is usually forced after a certain time period, this may result in a restart of the control system PCs during a beam time. To avoid this problem, a sub-group "Isoltrap" has been created within the Cmf comprising the Isoltrap control system PCs. This group is now under local management (*locally managed*), i. e. the software packages to be installed as well as the time of installation can be adapted to the requirements at Isoltrap. Consequently, the availability of the control system is enhanced and a loss of beam time because of forced restarts can be prevented.

Furthermore, in order to facilitate the management and the distribution of control system applications and settings, a Subversion (Svn) repository [130] in analogy to the

---

[7] These enhancements include a replacement of the switching circuit of the first pulsed cavity to allow a higher repetition rate. This work is part of the PhD thesis of Robert Wolf.

repository used for the CS framework has been set up. Using Svn, it is possible to save files and folders with an associated number (a *version*) and restore each version later-on. To make this procedure efficient only the changes to the previous version are copied to the repository, which reduces the necessary time and disk space significantly. Applied to Isoltrap, this concept allows an easy distribution of new control system applications and facilitates a documented and commented backup of control system settings like the object configuration database, domain configuration data, or Gui settings.

5.4.2 Integration of Further Devices

In addition to the improvements described above, several new devices have been integrated into the control system.

- For the data acquisition at Isoltrap the Mcs SR430 from Stanford Research had been used. Due to problems with this device, which seriously and increasingly hampered the reliability and performance of the control system, the need for a new Mcs arose. As a solution, an Fpga card (NI Pci 7811R, the same type used for the timing generator) has been implemented as an Mcs using an existing CS class [131]. As a further advantage, the time for data processing in the new Mcs is reduced by several hundred milliseconds compared to the SR430, which reduces the measurement time by up to 50%. In the following, this Fpga-Mcs has been used successfully for several beam times in 2012.

- A new class has been programmed for the valve control device Pfeiffer Rvc 300 (for a code example see Fig. 5.7). It is now possible to use a Pi (proportional integral) control based on the feedback of a Penning vacuum gauge for the pressure regulation in the buncher and in the preparation trap. Before, only a gas flow could be set via an analog control voltage. As a constant pressure of helium is required within both systems, the pressure had to be monitored and corrected manually before. The communication between the control system and the Rvc 300 is realized via an RS232 interface. In the case of using the device for the operation of the buncher, a potential-free connection is required. To allow an easy integration of further devices requiring a potential-free connection, an optical fiber based on Ethernet technology has been chosen together with an RS232-Ethernet converter.[8]

- In the context of the implementation of the Mr-Tof mass separator and the stacking mode, a second high-voltage (HV) power supply (Heinzinger Pnc 65 kV) was required. A class for the integration into the control system has been written together with an corresponding LabView instrument driver. As the experimentalist is supposed to control both HV power supplies by setting one absolute voltage value and the second relative to the first, an additional wrapper class has been programmed to allow an convenient use of both HV power supplies. The communication between the control system and the new Heinzinger power supply

---

[8] Meanwhile, a R&S AM300 frequency generator has been integrated in addition using an Usb-Ethernet converter.

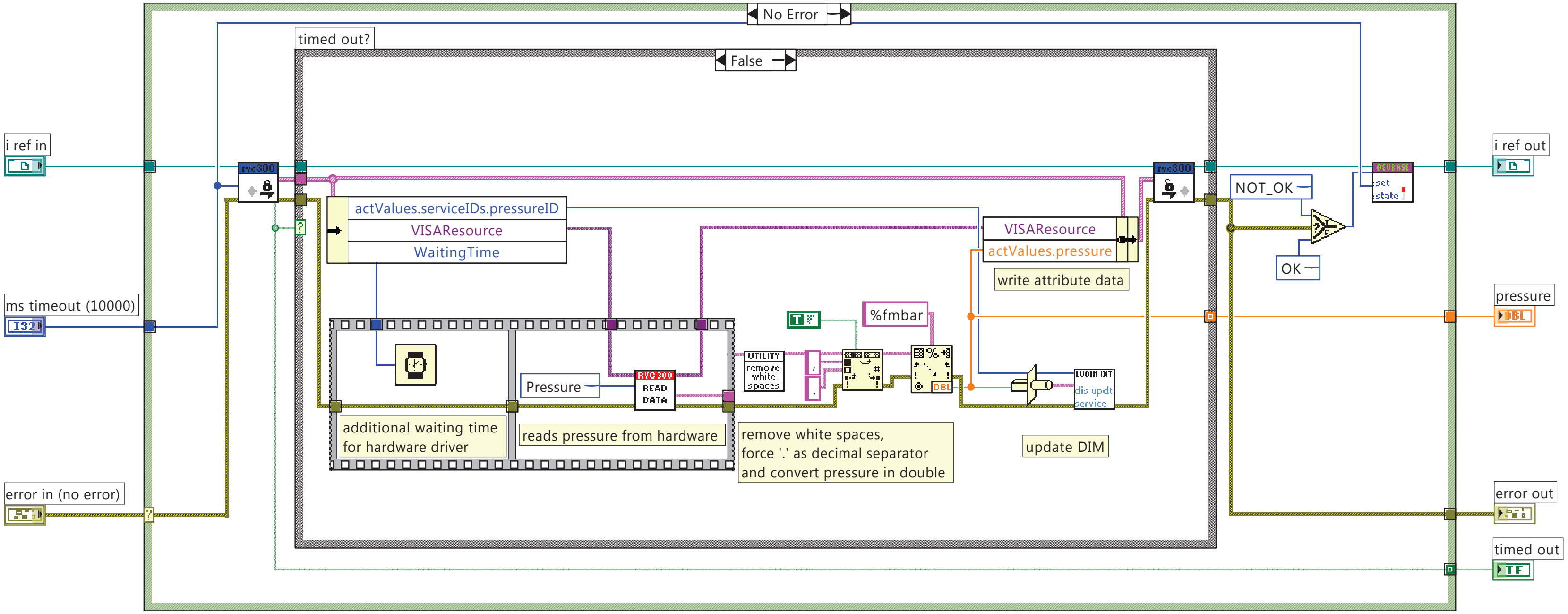

Figure 5.7: *(Color) Sample* LabView *code. This snippet is taken from the CS class Pfeiffer-*Rvc*300, which integrates the valve control device* Pfeiffer Rvc *300 into the CS framework. It shows the code of the method* GetPressure*, which reads the actual pressure from the device using the instrument driver provided by* Pfeiffer.

is realized via the Gpib interface and a Gpib–Ethernet converter to circumvent instability problems due to cable length exceeding the Gpib specifications (> 4 m).

- A new multi-channel high-voltage power supply (Caen SY2527) has been taken into operation and integrated into the control system. The communication is performed via Ethernet (Tcp/Ip) in connection with the Opc protocol. The integration into LabView is done using the Dsc (*Datalogging and Supervisory Control*) module from National Instrument.
- Furthermore, several steering elements in the transfer region between the preparation trap and the precision trap, which were manually set before, are now fully integrated into the control system. The output-voltage values are set via analog control voltages. The control voltages are generated using already existing analog-voltage output modules. These modules are connected to the control PCs via a Profibus system using an RS485 connection. The communication with the control system in turn is based on Opc as in case of the Caen SY2527.
- For focusing the beam from the alkali offline ion source into the main Isoltrap beam line (see Fig. 4.2), small quadrupole steering elements are used. They had been manually controlled and are now as well integrated into the control system. For this purpose, an analog control voltage is used, which is produced by a NI Pci 6703 card. In addition, a wrapper class has been written to allow a comfortable setting of voltages in terms of a general focus voltage and two voltages dedicated to vertical and horizontal focusing, respectively.

With the integration of the above-mentioned power supplies into the control system, all regularly changed power supplies at Isoltrap are now accessible via the control system.

5.4.3 Upgrade to LabVIEW 2009

The control system of Isoltrap was based on the CS framework version 3.14, which was programmed using LabView 8.20. As this LabView version is no longer supported by National Instruments, the support for the corresponding CS framework version was dropped as well by the developers. Hence, the whole Isoltrap control system has been successfully migrated to the most recent CS framework version 3.21 which is based on LabView 2009. At the same time, obsolete classes and drivers have been removed from the control-system source code. The core of the control system is now compiled into three different executable files, one including timing classes, the second one including power-supply classes and the third one including further device classes. These three executable files are in turn used to create the currently eight different instances of the control system.[9]

---

[9] For example, the PowerCS as shown in Fig. 5.5 is in reality split into three different instances on three different nodes.

6 Measurements and Evaluation

In this chapter, the data-analysis method including the calculation of uncertainties will be described. Furthermore, the evaluation of mass values in the context of the Atomic Mass Evaluation (AME) is discussed. Finally, the measurements performed in the context of this thesis are presented.

6.1 Mass Determination and Data Analysis

The experimental technique for the determination of the cyclotron frequency of an ion stored in a PENNING trap has been described in Sections 2.4 and 4.2.2. In order to calculate the mass from a measured cyclotron frequency, the relation between mass and free cyclotron frequency as introduced in Eq. (2.2)

$$\nu_c = \frac{1}{2\pi} \cdot \frac{q}{m_{\text{ion}}} \cdot B$$

is used as a starting point.[1] In order to cancel the magnetic field B, the cyclotron frequency of an ion with well-known mass is measured in addition (typically called *reference measurement).* At ISOLTRAP, usually alkali ions such as $^{39}\text{K}^+$, $^{85}\text{Rb}^+$ or $^{133}\text{Cs}^+$ are used for this purpose. The reference frequency ν_{ref} together with the cyclotron frequency of the ion of interest ν are then combined to yield the mass of the ion of interest m_{ion}

$$m_{\text{ion}} = \frac{\nu_{\text{ref}}}{\nu} \cdot m_{\text{ion,ref}} \cdot \frac{q}{q_{\text{ref}}}, \tag{6.1}$$

with $m_{\text{ion, ref}}$ denoting the mass of the reference ion, q the charge of the ion of interest and q_{ref} the charge of the reference ion. In the context of this thesis, only singly positively charged ions have been measured, so the charge of the ion of interest and the charge of the reference ion cancel. Using furthermore atomic masses m and m_{ref} instead of the ionic masses m_{ion} and $m_{\text{ion, ref}}$ as well as the mass of the electron m_e Eq. (6.1) therefore results in

$$m = r \cdot (m_{\text{ref}} - m_e) + m_e \tag{6.2}$$

$$\text{where} \quad r = \frac{\nu_{\text{ref}}}{\nu}. \tag{6.3}$$

In the cases investigated, the binding energy of the electron is small compared to the uncertainties obtained and hence neglected. As the values for the mass of the reference m_{ref} and the mass of the electron m_e may be subject to changes in the future due to new measurements, the mass of the measured nuclide may change accordingly. However, the

---

[1] Hereafter, the index "c" is omitted for clarity, as only cyclotron frequencies are discussed ($\nu_c \equiv \nu$).

ratio r between the cyclotron frequencies is independent of m_{ref} and is thus durable. From this frequency ratio r, the mass of the measured nuclide can be calculated at any time using Eq. (6.2) and the most recent mass values of reference nuclide and electron, respectively.

Below, it is described how the individual cyclotron frequencies, the individual frequency ratios as well as their uncertainties are determined. Usually, several measurements of the cyclotron frequencies are performed to determine the final frequency ratio r. Therefore, the combination of k different frequency ratios to one common ratio is described along with the calculation of its uncertainty.

6.1.1 Determination of the Cyclotron Frequency

To determine the cyclotron frequency of the ion of interest, the excitation frequency is varied in i steps around the assumed cyclotron frequency (see as well Section 2.4 and 4.2.2). For each experimental cycle with frequency value ν_{rf}^i, the number of ions counted using the MCP detector (see Fig. 4.2), their (binned) time of arrival, and the excitation frequency are recorded. A sequence of experimental cycles comprising all frequency steps i is called a *scan*. Each scan is repeated several times until a reasonable TOF resonance as shown in Fig. 2.23 is obtained. Such a TOF resonance is then called a measurement. For the actual determination of the cyclotron frequency, the recorded ions are then summed according to the frequency values. With T_j denoting the binned arrival time of the ions, $N_{i,j}$ the number of ions in the j-th bin and N_i the total number of ions for the i-th frequency value, a mean TOF $\overline{T}_i$ is calculated for each frequency value

$$\overline{T}_i = \frac{\sum_j N_{i,j} \cdot T_j}{N_i}. \tag{6.4}$$

As uncertainty usually the standard deviation of $\overline{T}_i$ would be used. However, for the measurements presented in the context of this thesis, the number of ions per frequency step is usually too small to form a solid statistical basis for the use of the standard deviation. Instead, the *sum statistics* approach (see e. g. Ref. [132–134]) has been chosen. Here, it is assumed that the time of flight is independent of the excitation frequency ν_{rf} (which is not the case in reality and therefore only an approximation). Hence, the standard deviation of the whole ion distribution

$$\sigma_{\overline{T}} = \sqrt{\frac{1}{N-1} \sum_j N_j \cdot (\overline{T} - T_j)^2} \tag{6.5}$$

can be used as basis. Here, N denotes the total number of ions within a measurement, N_j the total number of ions which arrived at the time T_j and $\overline{T}$ the mean time of flight of all ions. The uncertainty of the frequency-dependent mean time-of-flight values $\overline{T}_i$ as calculated by Eq. (6.4) is then determined by

$$\sigma_i = \frac{\sigma_{\overline{T}}}{\sqrt{N_i}}. \tag{6.6}$$

However, this procedure usually leads to an overestimation of the uncertainty, as the standard deviation of the whole ion distribution is usually larger due to the frequency dependence of the Tof. It is used here nevertheless as it is the only reasonable possibility to assign an uncertainty to Tof values with low numbers of ions, which is especially obvious for values with only one ion.

The cyclotron frequency and its uncertainty is then obtained by fitting Eq. (2.23) to the frequency-dependent mean time-of-flight values. The distributions of the electric and magnetic fields required therefore are shown in Fig. 4.4.

In order to account for shifts of the cyclotron frequency due to Coulomb interaction of the ions of interest with unwanted ions present in the trap during the excitations [135], a *count-rate analysis* [136, 137] is performed. Here, the ions are grouped in classes depending on the number of ions per cycle. Then the cyclotron frequency is determined for each class individually. Afterwards, the cyclotron frequency is extrapolated to one (unperturbed) ion in the trap with an assumed detector efficiency of 30 (±10)%.

The whole procedure of cyclotron frequency determination as described above is performed using a C++ program called Eva (see as well Section 5.2.3).

6.1.2 Determination of the Individual Frequency Ratios

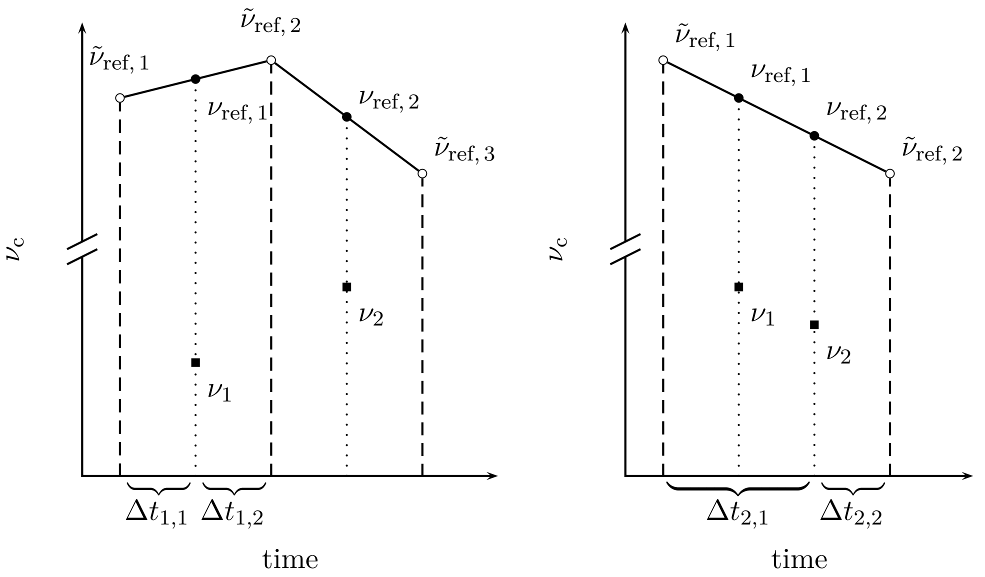

(a) **(b)**

Figure 6.1: *Interpolation of reference measurements. As the magnetic field is subject to changes, the cyclotron frequency of the reference ion $\nu_{ref,k}$ at the time of the measurement of the cyclotron frequency of the ion of interest ν_k is interpolated from two measurements $\tilde{\nu}_{ref,m}$ taken before and after. To save measurement time, usually at least one reference measurement is shared. In (a), two measurements of the ion of interest share one reference measurement, in (b) two references are shared. $\Delta t_{k,1}$ denotes the time from the first reference measurement until the measurement of the ion of interest and $\Delta t_{k,2}$ the time from the measurement of the ion of interest until the second reference measurement.*

The magnetic field generated by a cryogenic superconducting magnet is not stable, but decays linearly with time due to *flux creep* [138, 139] and depends in addition on non-linear temperature and pressure fluctuations [137]. As it is not possible to measure the cyclotron frequency of the reference ion at the same time as the one of the ion of interest, two reference measurements denoted $\tilde{\nu}_{\mathrm{ref},m}$ and $\tilde{\nu}_{\mathrm{ref},m+1}$, taken before and after the measurement of the ion of interest k are used for each individual frequency ratio. From these two measurements, the cyclotron frequency $\nu_{\mathrm{ref},k}$ of the reference ion at the time of the measurement is interpolated (see Fig. 6.1) according to

$$\nu_{\mathrm{ref},k} = \frac{1}{\Delta t_{k,1} + \Delta t_{k,2}} \left(\tilde{\nu}_{\mathrm{ref},m+1} \cdot \Delta t_{k,1} + \tilde{\nu}_{\mathrm{ref},m} \cdot \Delta t_{k,2}\right). \tag{6.7}$$

Here, $\Delta t_{k,1}$ denotes the time from the first reference measurement until the measurement of the ion of interest and $\Delta t_{k,2}$ the time from the measurement of the ion of interest until the second reference measurement. From the interpolated reference frequency and the cyclotron frequency of the ion of interest, the individual frequency ratio r_k

$$r_k = \frac{\nu_{\mathrm{ref},k}}{\nu_k} \tag{6.8}$$

is calculated.

The calculation of the common frequency ratio as well as its error requires the determination of the variance matrix $\boldsymbol{V}$. As a starting point to calculate the elements of this matrix,

$$V_{k,k'} = \mathrm{cov}(r_k, r_{k'}) = \sum_i \sum_j \left(\frac{\partial r_k}{\partial f_i}\right) \left(\frac{\partial r_{k'}}{\partial f_j}\right) \mathrm{cov}(f_i, f_j) \tag{6.9}$$

is used[2]. Here, the f_i, f_j comprise the reference measurements $\tilde{\nu}_{\mathrm{ref},m}$ and the ion-of-interest measurements ν_k

$$\{f_i, f_j\} = \{\nu_k\} \cup \{\tilde{\nu}_{\mathrm{ref},m}\} \tag{6.10}$$

and $\mathrm{cov}(f_i, f_j)$ denotes the covariance between f_i and f_j. As all f_i, f_j are statistically independent, $\mathrm{cov}(f_i, f_j)$ is

$$\mathrm{cov}(f_i, f_j) = \delta_{ij} \cdot \sigma_{f_i}^2. \tag{6.11}$$

Therefore, Eq. (6.9) becomes

$$V_{k,k'} = \sum_i \left(\frac{\partial r_k}{\partial f_i}\right) \left(\frac{\partial r_{k'}}{\partial f_i}\right) \sigma_{f_i}^2. \tag{6.12}$$

If one evaluates Eq. (6.12) together with Eqs. (6.7) and (6.8) for the diagonal elements ($k = k'$), this results

$$V_{k,k} = \frac{1}{\nu_k^2 (\Delta t_{k,1} + \Delta t_{k,2})^2} \left(\sigma_{\mathrm{ref},m+1}^2 \cdot \Delta t_{k,1}^2 + \sigma_{\mathrm{ref},m}^2 \cdot \Delta t_{k,2}^2\right) + \left(\frac{r_k}{\nu_k}\right)^2 \sigma_k^2, \tag{6.13}$$

which is the variance in the case of no correlations. However, one reference is usually shared by at least two measurements of the ion of interest to save valuable measurement time (see Fig. 6.1). In this case, the frequency ratios r_k and $r_{k'}$ are correlated, which has to be taken into account. Hence, the variance matrix is further populated with

---

[2] For a derivation of this formula, see a textbook about error calculation, e. g. Ref. [140]

correlation terms.[3] In the case of one common reference (see Fig. 6.1 a), Eq. (6.12) becomes

$$V_{k,k'} = \frac{1}{\nu_k \nu_{k'}(\Delta t_{k,1} + \Delta t_{k,2})(\Delta t_{k',1} + \Delta t_{k',2})} \cdot \Delta t_{k,1} \cdot \Delta t_{k',2} \cdot \sigma^2_{\mathrm{ref},m+1}. \tag{6.14}$$

In case both reference measurements are shared (see Fig. 6.1 b), the correlation between the frequency ratios k and k' is calculated by

$$V_{k,k'} = \frac{1}{\nu_k \nu_{k'}(\Delta t_{k,1} + \Delta t_{k,2})^2} \cdot (\Delta t_{k,1} \cdot \Delta t_{k',1} \cdot \sigma^2_{\mathrm{ref},m+1} + \Delta t_{k,2} \cdot \Delta t_{k',2} \cdot \sigma^2_{\mathrm{ref},m}). \tag{6.15}$$

Furthermore, a relative systematic uncertainty u_B is added in quadrature to the uncorrelated error to account for the magnetic field drift due to the flux creep. It is calculated according to [137] via

$$u_\mathrm{B} = 6.35 \cdot 10^{-11}/\mathrm{min} \cdot \Delta T, \tag{6.16}$$

with $\Delta T = \Delta t_{k,1} + \Delta t_{k,2}$ denoting the time between the two reference measurements.

6.1.3 Determination of the Common Frequency Ratio

After the determination of the individual frequency ratios, a weighted average is calculated to obtain the common frequency ratio. In the context of this work, frequency ratios with an uncertainty 10 times larger than the smallest error have been omitted due to insignificance. The weighted average is calculated via

$$\bar{r} = \frac{\sum_{k,k'}(V^{-1})_{k,k'} \cdot r_k}{\sum_{k,k'}(V^{-1})_{k,k'}} \tag{6.17}$$

with $(V^{-1})_{k,k'}$ denoting the elements of the inverse matrix $\boldsymbol{V}^{-1}$. The corresponding uncertainty $\sigma_{\bar{r}}$ resulting from error propagation is calculated using

$$\sigma_{\bar{r}} = \sqrt{\frac{1}{\sum_{k,k'}(V^{-1})_{k,k'}}}. \tag{6.18}$$

To check the consistency of the data, the reduced χ^2 is calculated using the weighted average $\bar{r}$ and the vector of all individual frequency rations $\vec{r} = \{r_1, \ldots, r_k\}$

$$\chi^2/(k-1) = (\vec{r} - \bar{r} \cdot \vec{e}) \cdot \boldsymbol{V}^{-1} \cdot (\vec{r} - \bar{r} \cdot \vec{e})' \tag{6.19}$$

with $\vec{e}$ denoting the unity vector. In case $\chi^2/(k-1) \leq 1$ the mean ratio is used as calculated. In case $\chi^2/(k-1) > 1$ (but not too large) and no further source of uncertainty can be identified after careful consideration, the uncertainty $\sigma_{\bar{r}}$ is increased by a factor $\sqrt{\chi^2/(k-1)}$ according to Ref. [142].

Apart from the decay of the magnetic field discussed above, a further systematic

---

[3] This approach is also used at PENNING-trap mass spectrometer TITAN, see Ref. [134, 141].

uncertainty, a mass-dependent effect ϵ_m

$$\frac{\epsilon_m(r)}{r} = -1.6(4) \cdot 10^{-10}/\mathrm{u} \cdot (m - m_\mathrm{ref}) \tag{6.20}$$

has been found in the study of systematic uncertainties at ISOLTRAP [136, 137]. Therefore, the frequency ratio r is corrected to obtain the final ratio r_final by

$$r_\mathrm{final} = \bar{r} + (1.6 \cdot 10^{-10}/\mathrm{u} \cdot (m - m_\mathrm{ref})) \cdot \bar{r}. \tag{6.21}$$

In addition, an uncertainty of the same magnitude

$$\sigma_m = (1.6 \cdot 10^{-10}/\mathrm{u} \cdot (m - m_\mathrm{ref})) \cdot \bar{r} \tag{6.22}$$

is added quadratically to the uncertainty [137]. As a residual systematic uncertainty σ_res

$$\sigma_\mathrm{res} = 8 \cdot 10^{-9} \cdot \bar{r}, \tag{6.23}$$

whose origin is undetermined up to know, has been found [137], it is taken into account as well.

The final uncertainty σ_final of the frequency ratio is therefore calculated by

$$\sigma_\mathrm{final} = \sqrt{\sigma_{\bar{r}}^2 + \sigma_m^2 + \sigma_\mathrm{res}^2}. \tag{6.24}$$

All calculations for the data analysis as discussed here and in Section 6.1.2 have been performed using the open-source programming language OCTAVE [143].[4]

6.2 The Atomic Mass Evaluation (AME)

To make the discussion of mass values more convenient, the *mass excess* (*ME*)

$$ME = m - A \cdot \mathrm{u} \tag{6.25}$$

with A denoting the mass number and u the atomic mass unit is commonly used. This quantity must not be mixed up with the binding energy as defined in Eq. (3.2): In contrast to the binding energy, which is referring to the mass of proton and neutron, the mass excess makes use of the atomic mass unit u which is derived from ^{12}C.

In the ideal case, a mass is not only measured by one experiment, but by several experiments (ideally using several different experimental techniques). Furthermore, in many cases other masses are needed as input parameters for the determination of the measured mass value (in the case of this thesis the mass of ^{133}Cs). This leaves the questions how to determine the input mass values as well as how to determine a common mass value from many different experiments. To solve this problem, the *Atomic Mass Evaluation* (AME) was created [46, 144].

In order to provide a reliable mass value within the AME, a least-squares fit of all

---

[4] OCTAVE is specially dedicated to numerical calculations and has been programmed to be mostly compatible with the well-known commercial programming language MATLAB.

available mass values is done. For this fit, a linear relation[5] between the mass excess of the ion of interest and the mass excess of the reference ion is taken according to

$$ME - C \cdot ME_{\text{ref}} = MD, \tag{6.26}$$

with C defined as the truncated three-digit approximation

$$C = \left(\frac{A}{A_{\text{ref}}}\right)_{\text{trunc}} \tag{6.27}$$

and MD being the *mass difference*. In case of the Isoltrap experiment (and other experiments providing frequency ratios), this mass difference is derived from Eq. (6.2) to be

$$MD = ME_{\text{ref}} \cdot (r - C) + m_e \cdot (1 - r) + A_{\text{ref}} \cdot \left(r - \frac{A}{A_{\text{ref}}}\right) \tag{6.28}$$

with A and A_{ref} denoting the mass number of the ion of interest and of the reference ion, respectively. In this case, all mass and mass excess values are expressed in atomic mass units. For more details see Ref. [145].

To include a new Isoltrap measurement into the Ame, the MD value is calculated from the frequency ratio r and a new least-squares fit is performed over all (possible) MD values. This yields the intermediate mass-excess value ME_{exp} and its error σ_{exp}. If there is a possibility of unresolved isomers (see Section 4.2.3), an isomeric correction is applied according to Ref. [144]: In case of one unresolved isomer[6] with an excitation energy $E_1 \pm \sigma_1$ and an unknown ratio between ground state and isomer, the corrected mass excess value for the ground state ME_{gs} and its error σ_{gs} are obtained via

$$ME_{\text{gs}} = ME_{\text{exp}} - \frac{1}{2}E_1 \tag{6.29}$$

$$\sigma_{\text{gs}} = \sqrt{\sigma_{\text{exp}}^2 + \left(\frac{1}{2}\sigma_1\right)^2 + \frac{1}{12}E_1^2}. \tag{6.30}$$

If there are no unresolved isomers, the intermediate value M_{exp} will become the final mass-excess value.

6.3 Results

In the context of this thesis, the masses of silver, francium, radium and thallium nuclides have been determined. The data were recorded in four separate beam times (also called *runs*) between 2009 and 2011. The parameters of the different runs are summarized in Tab. 6.1. All targets for the production of the short-lived nuclides were made from uranium-carbide (UC). In the first run, a neutron converter (see Section 4.1) was used in order to enhance the ratio of neutron-rich to neutron-deficient fragments. For the ionization of the silver isotopes and partly for measurements of the thallium isotopes,

---

[5] In general, a linear relation between the fit parameters is preferred when performing a least-squares fit as it greatly simplifies the fit procedure.

[6] In the context of this thesis, only corrections for one unresolved isomer have been applied. For cases with more than one unresolved isomer, see Ref. [144].

Table 6.1: *Parameters of the separate beam times. For all runs, time period,* Cern *experiment number,* Isolde *front end (FE),* Isolde *target type and number, the type of ion source as well as the beam energy are listed.*

Run	Date	Exp.	FE	Target	Ion Source	Beam Energy
1	05.-07.06.2009	IS 413	GPS	UC-Ta, n-conv (#400)	Rilis	30 keV
2	16.-17.11.2010	IS 463	HRS	UC-W (#441)	surface	40 keV
3	07.-09.06.2011	IS 473	HRS	UC-Ta (#447)	surface	50 keV
4	18.-22.07.2011	IS 463	GPS	UC-W (#453)	surface / Rilis	50 keV

Rilis (see Section 4.1) was used. The other isotopes were ionized via surface ionization only. To keep the mass-dependent error as low as possible as discussed in Section 6.1.3, ^{133}Cs^{+}, the heaviest ion available from Isoltrap's alkali offline ion source, was used as a reference ion for all measurements. In addition, in all runs the mass of ^{85}Rb was determined as a cross check. The results of the cross checks agree in all cases within $1\,\sigma$ with the literature value. An overview of the frequency ratios obtained with the data analysis procedure as described in Section 6.1 is given in Tab. 6.2. Comparing the mass-excess values calculated from the frequency ratios with the previous known literature values ME_{prev}, a good overall agreement is visible (see Fig. 6.2).

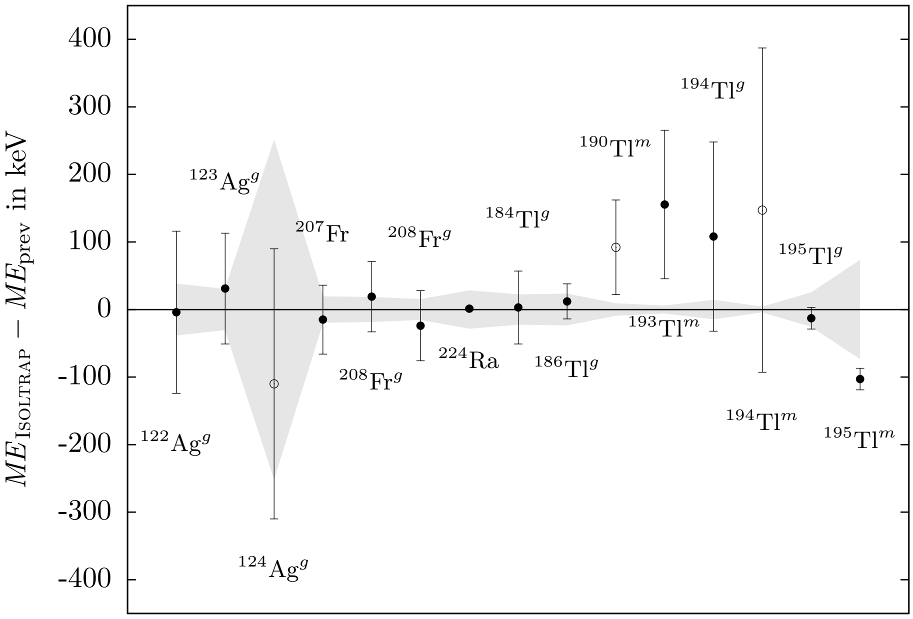

Figure 6.2: *Agreement of the new mass values with previous measurements. The plot shows the difference between the new* Isoltrap *mass-excess value (this work) and the previously known mass-excess value taken from the* Ame *before entering the new data [146, 147]. Open circles denote values where the previous mass excess values was only estimated. The gray-shaded area denotes the uncertainties of the new measurements and the errorbars denote the uncertainties of the previously known values.*

Table 6.2: *Results of the data analysis. The first column denotes the nuclide investigated, the second column the run during which the measurement was performed, the third the number k of resonances taken and the fourth the frequency ratio obtained. States are labeled in ascending order with 'g', 'm' and 'n' for ground, first and second excited state, respectively. In case of a possibly unresolved mixture 'x' is used. The reference ion is* $^{133}Cs^{+}$ *in all cases.*

Isotope	Run	k	frequency ratio
^{122}Ag^{x}	1	3	0.917371415 (138)
^{123}Ag^{x}	1	3	0.924907931 (228)
^{124}Ag^{x}	1	2	0.93245906 (201)
^{207}Fr	3	1	1.557477497 (151)
^{208}Fr^{g}	3	2	1.565002922 (148)
^{208}Fr^{g}	4	3	1.565003269 (119)
^{224}Ra	3	1	1.685563561 (226)
^{184}Tl^{x}	4	6	1.3843079180 (467)
^{186}Tl^{x}	4	5	1.3993322212 (645)
^{186}Tl^{n}	4	2	1.399335335 (259)
^{190}Tl$^{7(+)}$	4	7	1.4293932577 (712)
^{193}Tl^{m}	2	2	1.4519430629 (438)
^{194}Tl^{g}	2	2	1.459468599 (114)
^{194}Tl^{m}	2	6	1.4594706992 (310)
^{195}Tl^{g}	2	2	1.466982887 (200)
^{195}Tl^{m}	2	2	1.466987515 (593)

After the data analysis, all frequency ratios have been included in the AME as described in Section 6.2. The results of the evaluation can be found in Tab. 6.3. All mass excess values labeled *previous* have been taken from the AME just before entering the new data whereas all mass excess values labeled *new* have been taken from the AME after including the new results presented here. All results concerning the previous and new AME are taken from Ref. [146, 147]. A complete version of the most recent AME is scheduled for publication later this year [147]. Following the convention used throughout the AME, values which are not based on measurements but on systematic extrapolations are marked by '#'. Furthermore, ground states are labeled with 'g' and isomeric states in ascending order with 'm' and 'n'. Possibly unresolved mixtures are labeled with 'x'.

6.3.1 Neutron-rich Silver Isotopes

The measurements of the silver isotopes $^{122-124}$Ag completed a series of measurements on neutron-rich silver isotopes started in 2006 [47, 48]. For ^{122,123}Ag the uncertainty could be reduced significantly, whereas the mass of ^{124}Ag was determined for the first time. The results of the data analysis and evaluation have been published in Ref. [48].

^{122}Ag

The *ME* value obtained for ^{122}Ag at ISOLTRAP was −71066 (17) keV. As there are known isomers for this isotope and both are produced at ISOLDE [148], isomeric corrections had to be applied. Nevertheless, the knowledge of excitation energies of these isomers is quite poor. The best information available at the moment is an assumption based on the known isomers of the odd-N neighbors. These assumptions resulted in a predicted excitation energy of 80# (50#) keV [54] for an averaged isomer. Based on an unknown production rate of the isomers at ISOLDE and the unknown excitation energy, it was assumed, that the estimated excitation energy mentioned above is sufficient to achieve a reasonable correction. This yields for the ground-state $ME(^{122}\mathrm{Ag}) = -71106\,(38)$ keV. In case of further knowledge of the excitation energy of the isomers in the future, the isomeric corrections to derive the ground state can be easily adapted. The mass excess value previously included in the AME for ^{122}Ag was determined at the *Experimental Storage Ring* ESR to $ME(^{122}\mathrm{Ag}) = -71110\,(120)$ keV [149] and agrees with the new value. Due to the precision of the new measurement, the *ME* included in the new evaluation is now completely determined by the ISOLTRAP result.

^{123}Ag

For ^{123}Ag a *ME* value of −69538 (28) keV was obtained. Deduced from the neighboring even-N silver isotopes, an isomer with an excitation energy of 20# (20#) keV was assumed based on Fig. 6.3. After the isomeric corrections the new *ME* for the ground state is −69548 (30) keV. The old value included in the mass evaluation was $ME(^{123}\mathrm{Ag}) = -69517\,(82)$ keV, which was determined by a previous ISOLTRAP measurements of Breitenfeldt et al. [47] with 54% and Sun et al. [149] at the ESR with 46%. The mass-excess value in the new AME is now completely determined by the new value presented here.

Table 6.3: *Overview of the data evaluation. The first column denotes the nuclide and the second the run in which its mass has been determined. The third column shows the ME value obtained from the frequency ratio. The value in the forth column is corrected for a possible isomeric contamination. The fifth column shows the ME value known before the measurement and the last column the ME value resulting from the new* Ame *[146, 147]. Values based on systematic extrapolations are marked by '#'. States are labeled in ascending order with 'g', 'm' and 'n'. In case of a possibly unresolved mixture 'x' is used. All ME values are in keV. For more details see text.*

Isotope	Run	Isoltrap *ME*	Isoltrap *ME* (corrected)	previous *ME*	new *ME*
^{122}Ag^{x}	1	−71066 (17)			
^{122}Ag^{g}			−71106 (38)	−71110 (120)	−71106 (38)
^{123}Ag^{x}	1	−69538 (28)			
^{123}Ag^{g}			−69548 (30)	−69517 (82)	−69548 (30)
^{124}Ag^{x}	1	−66200 (250)			
^{124}Ag^{g}			−66200 (250)	−66310#(200#)	−66200 (250)
^{207}Fr	3	−2846 (19)		−2861 (51)	−2845 (18)
^{208}Fr^{g}	3	−2691 (18)		−2672 (52)	−2665 (11)
^{208}Fr^{g}	4	−2648 (15)			
^{224}Ra	3	18826 (28)		18827.2 (2.2)	18827.2 (2.2)
^{184}Tl^{x}	4	−16898.6 (5.8)			
^{184}Tl^{g}			−16874 (22)	−16871 (54)	−16873 (20)
^{184}Tl^{m}				−16923 (62)	−16925 (37)
^{184}Tl^{n}				−16423 (63)	−16425 (37)
^{186}Tl^{x}	4	−19876.0 (8.0)			
^{186}Tl^{g}			−19887 (23)	−19875 (26)	−19887 (23)
^{186}Tl^{m}				−19875# (56#)	−19865 (32)
^{186}Tl^{n}	4	−19491 (32)		−19501# (56#)	−19491 (32)
^{190}Tl$^{7(+)}$	4	−24292.1 (8.8)			
^{190}Tl^{g}				−24333 (49)	−24382# (51#)
^{190}Tl^{m}				−24200# (70#)	−24292.1 (8.8)
^{193}Tl^{g}				−27320 (110)	−27292.0 (6.7)
^{193}Tl^{m}	2	−27105.5 (5.4)		−26950 (110)	−27105.5 (5.4)
^{194}Tl^{g}	2	−26938 (14)		−26830 (140)	−26938 (14)
^{194}Tl^{m}	2	−26677.2 (3.8)		−26530# (240#)	−26677.2 (3.8)
^{195}Tl^{g}	2	−28162 (25)		−28175 (16)	−28155 (11)
^{195}Tl^{m}	2	−27589 (73)		−27692 (16)	−27673 (11)

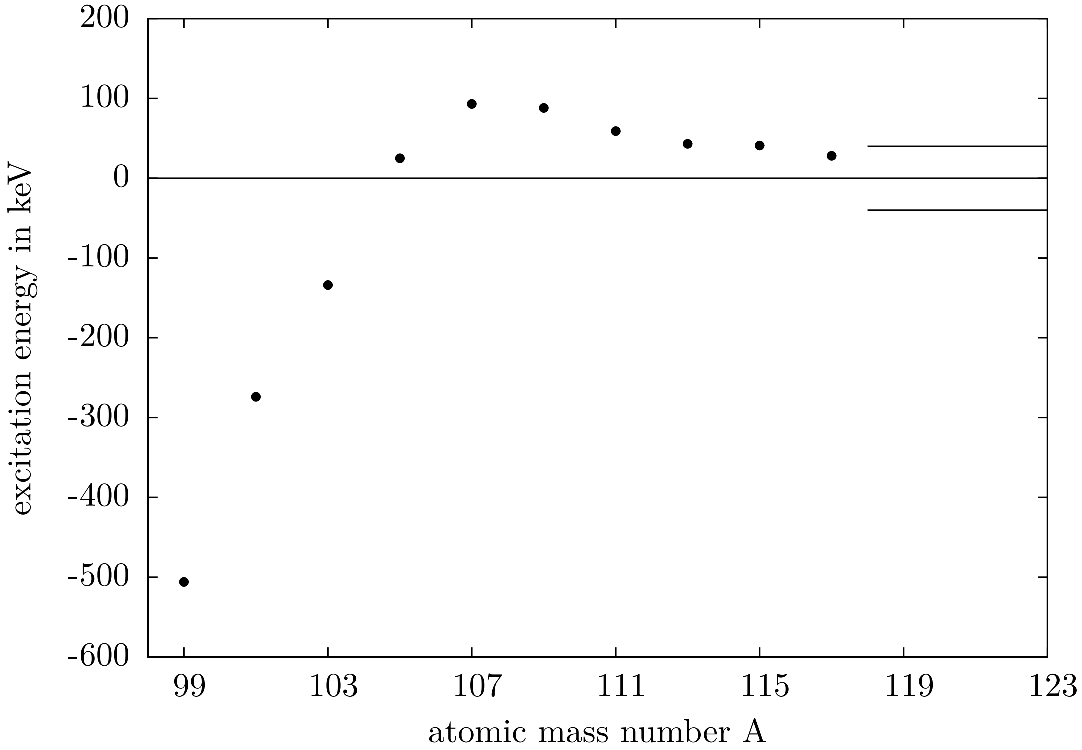

Figure 6.3: *Excitation energy of even-N silver isomers depending on the atomic mass number. The negative values for the first three values result from a reverse of the spins for ground-state and first excited state from* ^{99}*Ag to* ^{103}*Ag. The short horizontal line shows the range for the energy of the assumed isomers. The error bars are too small to be visible.*

^{124}Ag

For ^{124}Ag a *ME* value of −66200 (250) keV was obtained. Similar to $^{122-123}$Ag, an isomer is assumed. The excitation energy is predicted to be 0# (100#) keV. Thus, isomeric corrections had been applied, but due to the larger error of the mass-excess value, these corrections did not change the originally obtained value. As these measurements are the first ones for ^{124}Ag, the mass-excess value in the present mass evaluation is completely determined by this result. It agrees within the uncertainties with the previous estimated value of −66310# (200#) keV.

6.3.2 Neutron-deficient Francium Isotopes

The masses of the neutron-deficient francium isotopes $^{207-208}$Fr were determined in 2011. For both nuclides, the uncertainty could be reduced by at least a factor of three.

^{207}Fr

The mass of ^{207}Fr was determined in the beam time in June 2011. The obtained ISOLTRAP mass excess was −2846 (19) keV. As no isomers are known for this nuclide, no correction was applied. The new *ME* resulting from the AME is −2845 (18) keV.

It is determined to 88 % from this measurement, to 11.7 % from measurements of the α-decay energy to ^{203}At [150–152], and to 0.3 % from a mass measurement based on the deflection in electric and magnetic fields [153, 154].

^{208}Fr

The mass of ^{208}Fr was determined in two beam times in June and July 2011. The two results differ by $1.8\,\sigma$. However, both results agree within $1\,\sigma$ with the previous literature value for the ground state. A possible admixture of the first isomeric state could be excluded for both measurements as this state is too short-lived to be seen at ISOLTRAP. The new *ME* derived from the AME is −2653.1 (8.5) keV, resulting to 95.3 % from this measurement, to 4.2 % from measurements of the α-decay energy to ^{204}At [150–152], and to 0.6 % from a mass measurement based on the deflection in electric and magnetic fields [153, 154].

6.3.3 Radium-224

The mass of ^{224}Ra was determined in the beam time in June 2011 with a mass excess of 18826 (28) keV. As no isomers are known for this nuclide, no correction had to be applied. Due to its large uncertainty, the current measurement does not contribute to the *ME* of ^{224}Ra in the AME, which is currently determined to 58 % from measurements of the α-decay energy from ^{228}Th and to 42 % from the measurements of the α-decay energy to ^{220}Rn [155]. Nevertheless, it is the first direct mass measurement of this nuclide and confirms the present AME value. Furthermore, it serves as a cross-check for the other measurements presented here.

6.3.4 Neutron-deficient Thallium Isotopes

The masses of ground and isomeric states of the neutron-deficient thallium isotopes $^{184,186,190,193-195}$Tl were measured.The uncertainties could be reduced up to a factor of 20 (in case of ^{193}Tl^{m}) and the excitation energy of the first isomeric state in ^{194}Tl was determined for the first time.

^{184}Tl

In case of ^{184}Tl a *ME* of −16898.6 (5.8) keV was obtained at ISOLTRAP. Currently, the state ordering of the lowest-lying 2^- and the 7^+ states is unclear. In the Atomic Mass Evaluation, the 2^- state was assumed to be the ground state and the 7^+ state was assumed to be the isomeric state with an excitation energy of −50 (30) keV. From the ISOLTRAP side no information is available which of the states was measured. In a different experiment at ISOLDE a composition of 72 % for the 2^- and 28 % for 7^+ has been reported [156]. However, the data analysis of this experiment is still preliminary. Therefore, an equal mixture of both was assumed in the present evaluation, which resulted a corrected *ME* of −16874 (22) keV. Including this result in the AME, a new *ME* of the ground state has been determined to −16873 (20) keV. This value is determined to 86.3 % by the measurement presented here and to 13.7 % by measurements of the α-decay energy to ^{180}Au [157, 158].

^{186}Tl

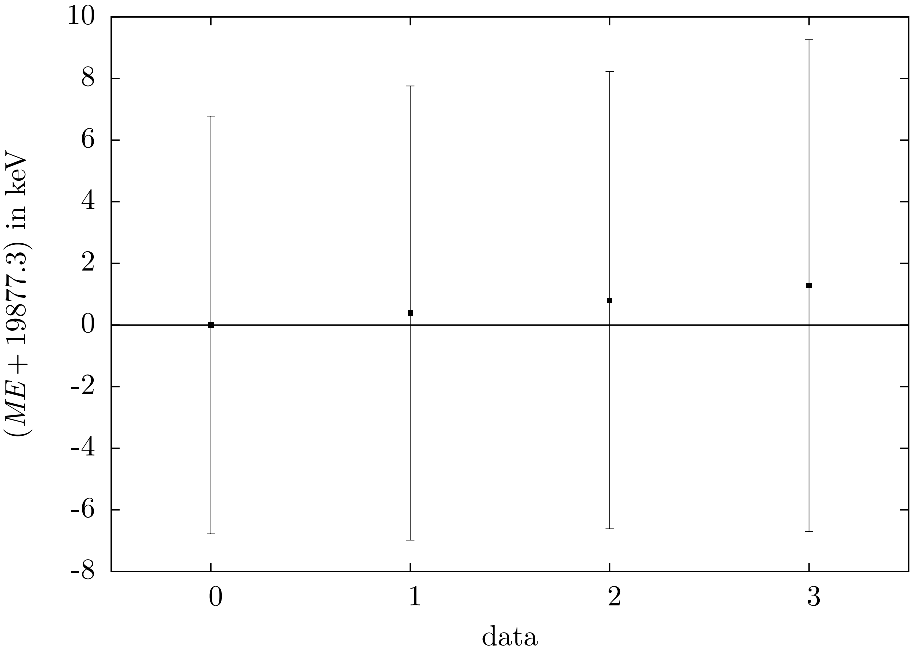

Figure 6.4: *Contributions due to correlations for $^{186}Tl^{g+m}$. In point 0, no correlations are taken into account. Point 1 includes correlations due to one shared reference, point 2 correlations due to two shared references and point 3 the final result with both correlations. A clear shift of the ME and increase of the error bars is visible.*

For ^{186}Tl two states were observed: For the low-lying state, a *ME* of −19876.0 (8.0) keV was obtained, whereas for the (weakly visible) high-lying state a *ME* of −19491 (32) keV was extracted using a double fit. The difference between the two states was thus calculated to 386 (33) keV. Due to this difference, the high-lying state can be easily assigned to the 10^- state, where the excitation energy between the 10^- and the 7^+ is known to be 373.9 (0.5) keV [159]. For the low-lying state, the situation is more complicated: In a previous measurement at ISOLTRAP by WEBER et al. [160] the measured state was assigned to be the 7^+ state based on spin systematics. In the light of the preliminary results of RAPISARDA and colleagues for ^{184}Tl [156] as discussed above, this argumentation might be challenged. Therefore, in the present argumentation, an equal mixture between the 2^- and 7^+ state was assumed. With an energy difference of 22 (41) kV between the two states, this yielded a corrected ground-state *ME* of −19887.0 (22.9) keV. The previous mass value included in the AME was completely determined by the earlier ISOLTRAP measurement. In the new mass evaluation, a ground-state *ME* of −19887 (23) keV and a second-isomer *ME* of −19491 (32) keV has been calculated. Both mass excesses are entirely determined by the measurements presented here.

As in case of this nuclide the highest corrections of the uncertainty and the frequency ratio due to correlation effects as described in Section 6.1.2 were observed during the data analysis, an overview of these effects is presented in Fig. 6.4: The overall effect is rather small, but nevertheless, a clear increase in uncertainty as well as a shift in the frequency ratio is visible.

^{190}Tl

For ^{190}Tl a *ME* of −24292.1 (8.8) keV was obtained. From decay spectroscopy performed together with the mass measurement, the *ME* could be assigned to the $7^{(+)}$ state [161]. The mass excess of the $7^{(+)}$ state in the new AME is entirely determined by the measurement presented in this work. This state is assumed to be the first isomeric state with an estimated energy difference to the ground state of 90# (50#) keV. The ground state energy of ^{190}Tl is therefore calculated to −24382# (51#) keV in the new evaluation and is solely based on the result presented in this work. The previous ground-state value was determined to −24330 (50) keV using SCHOTTKY mass spectrometry [25, 162].

^{193}Tl

The data analysis of the ^{193}Tl data resulted in a *ME* of −27105.5 (5.4) keV. Performing mass-assisted spectroscopy together with the mass measurement, the 372-keV internal transition was visible, which indicates that this *ME* belongs to the first isomeric state [161]. The *ME* value included in the AME before entering the new data was −27320 (110) keV, which was obtained using SCHOTTKY mass spectrometry [25]. Based on the mass excess of the first isomeric state, a ground-state mass excess of −27478.031 (6.7) keV has been obtained for the most recent AME, which is due to the precision of the new measurement completely determined by the ISOLTRAP value.

^{194}Tl

Up to now, the energy difference between the ground state and the isomeric state of ^{194}Tl had been unknown. In the context of this thesis, it could be determined for the first time by measuring the mass of the ground state and the mass of the excited state (for an example of the corresponding cyclotron frequency resonances, see Fig. 6.5). The ISOLTRAP mass excess of the ground state was determined to −26938 (14) keV and the mass excess of the excited state to −26677.2 (3.8) keV, which yields an excitation energy of 260 (15) keV. This agrees with the previous prediction derived from systematics of 300# (200#) keV. Plotted together with the excitation energies of further even-A thallium isotopes, the new excitation energy fits very well as one can see in Fig. 6.6.

Furthermore, the uncertainty of the ground-state mass excess could be reduced by one order of magnitude with respect to the previously known *ME* value of −26830 (140) keV measured using SCHOTTKY mass spectrometry [25] and is now, due to its precision, entirely based on the value presented in this work. From spectroscopic observations the high-spin state could be assigned to the isomer [161]. The measurement became possible by using a special technique for changing the abundance ratio of ground and isomeric state: While both, the ground state and the isomeric state were produced at ISOLDE, the ground state fraction was much lower than the isomeric fraction (on the order of 10%). This abundance ratio could be changed considerably (negligible contribution of the isomeric state) by stopping the proton impact on the target. Obviously, the main production channel for the isomer was direct production whereas the ground state was mainly populated indirectly by β decay from ^{194}Pb. The new AME values for the ground and the first excited state are entirely determined by the values presented here.

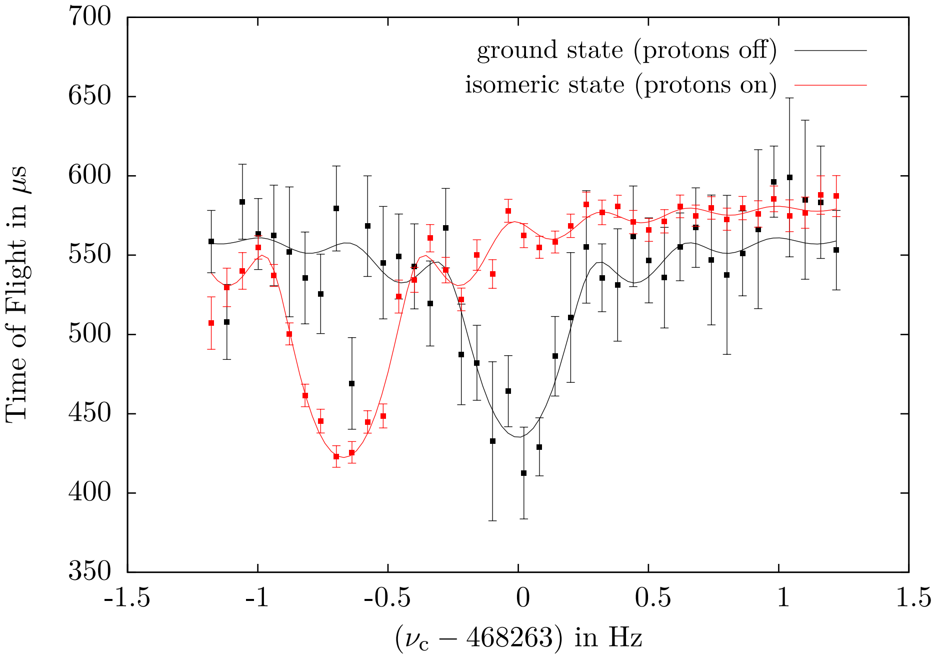

Figure 6.5: *(Color) Time-of-flight resonances of* $^{194}Tl^+$*. The abundance ratio of the ground and isomeric state at* ISOLDE *could be changed by switching the protons on the target on or off. The line is a fit to the data points using Eq. (2.23).*

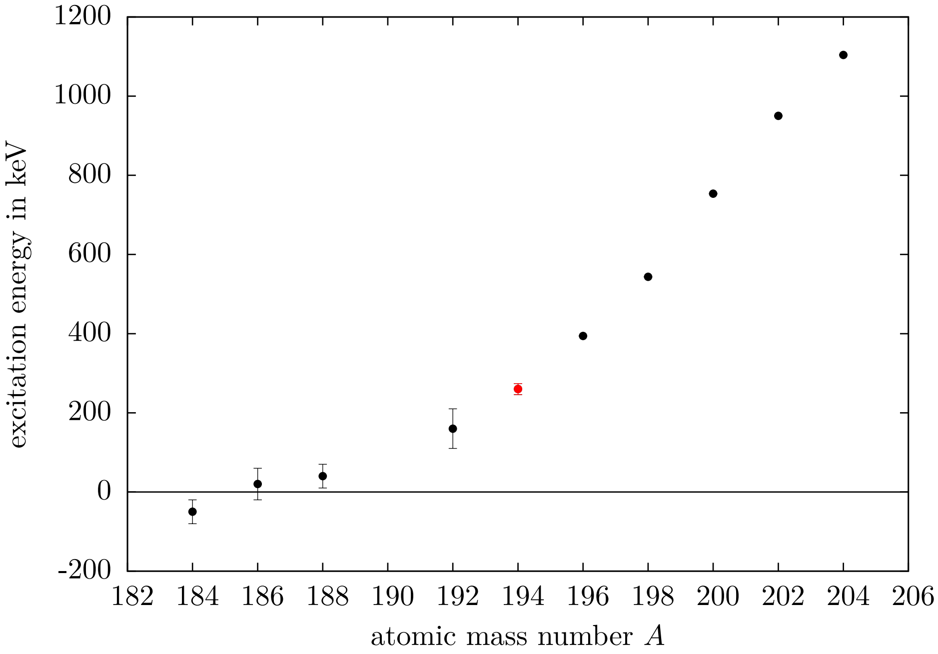

Figure 6.6: *(Color) Excitation energies of the first isomeric state in even-A thallium isotopes. The newly determined excitation energy of* ^{194}Tl *is marked in red.*

^{195}Tl

In the measurement of ^{195}Tl the ground state as well as the (hardly visible) isomeric state could be resolved. As only a slight asymmetry of the TOF resonances was visible, additional checks were performed to validate the presence of the isomeric state: Due to the strongly different half-lives of isomeric and ground state (3.6 s and 1.16 h respectively [54]), TOF spectra for different excitation times (100 ms and 1.2 s) were recorded. In these spectra, a significant increase in the number of decay products with increasing excitation time was observed as expected in case of an isomeric admixture. Consequently, a double fit using the known energy difference between ground and isomeric state [54] as a starting point was performed. For the ground state a *ME* of −28162 (25) keV was determined and for the isomeric state a *ME* of −27589 (73) keV, which results in an excitation energy of 573 (75) keV. This value agrees within 1.2 σ with the excitation energy of 482.36 (0.17) keV listed in NUBASE 2003 [54]. Furthermore, the ground-state mass excess has been found in agreement with the previous AME value of −28175 (16) keV. The new AME value for the ground state of −28155 (11) keV is determined to 56.4 % by a measurement of the α-decay energy from ^{199}Bi^{m}, to 21.9 % by SCHOTTKY mass measurements [25, 162] and to 21.7 % by the measurement presented here.

The example of ^{195}Tl is well-suited to illustrate the different connections within the AME: Via different steps the masses of ^{195}Tl and ^{207}Fr (see above) are linked and influence each other as visible in Fig. 6.7.

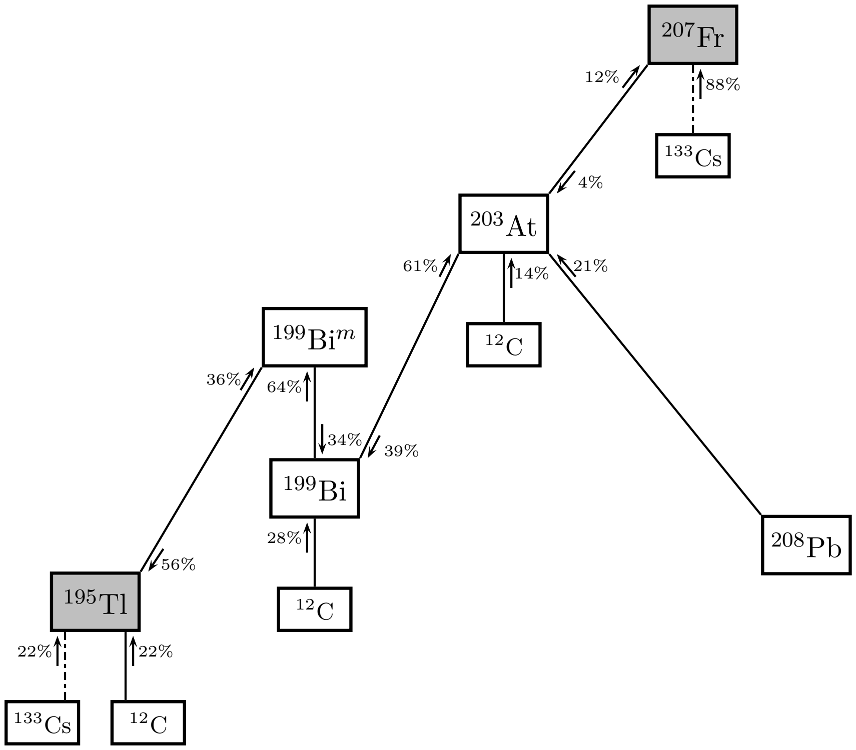

Figure 6.7: *Connection between ^{195}Tl and ^{207}Fr within the* AME. *Each line between two nuclide represents one (or more) measurements. The numbers in percent show the (rounded) influence of this measurement on the mass of the respective nuclide. The two dashed-dotted lines represent the new measurements provided within this work. The measurements determining the masses of ^{133}Cs and ^{208}Pb have been omitted for clarity.*

7 Physics Interpretation

For the discussion of the new odd-Z mass data, which have been obtained in the context of this thesis, two approaches have been chosen: First, the mass data are compared with theoretical models (see as well Section 3.4) and second, the experimental values are analyzed in the context of differences of binding energies (see as well Section 3.1).

7.1 Comparison With Mass Models

The benchmark for all theoretical calculations is always the comparison with experimental data. Hence, the new mass data are compared with theoretical values below. Mass values obtained by other experiments have been taken into account as well to allow a discussion of the corresponding region of isotopes. For the comparison only models providing a mass table which covers the complete nuclear chart have been used as these are especially challenged when looking at heavy and exotic nuclei. A comparison with *ab initio* calculations is unfortunately not possible as these are limited to light nuclei (see as well Section 3.4.2). The liquid-drop model has been chosen as a macroscopic model (see as well Section 3.4.1) and the FRDM1995 as a mic-mac model (see as well Section 3.4.3). For the mean-field models (see as well Section 3.4.2), two models with different underlying forces have been chosen, the HFB21 (based on the SKYRME force) and the D1M (based on the GOGNY force). An overview of the results of the comparison in terms of the root-mean-square deviation σ_{rms} (see Section 3.4) can be found in Tab. 7.1. As expected, the liquid-drop model provides the least agreement with a deviation well above 1 MeV. Nevertheless, the σ_{rms} is in all cases smaller than the σ_{rms} for the whole nuclear chart. The FRDM1995 and the HFB21 reproduce the data to a similar amount with a standard deviation around 0.33 MeV. Hence, the agreement for the discussed elements is as well better than the average agreement of these models with experimental masses. The agreement of the D1M predictions with the experimental data depends strongly on the element: While the agreement is quite good in case of thallium, the

Table 7.1: *Comparison of experimental data with theoretical models. The listed values are the σ_{rms} in MeV calculated using Eq. (3.9). The mass values used for the calculation are identical to the ones used for the mass comparison plots below ($N = 67 - 77$ for silver, $N = 118 - 128$ for francium and $N = 103 - 114$ for thallium).*

	Silver	Francium	Thallium
liquid drop	2.336	2.336	1.432
FRDM1995	0.280	0.389	0.331
HFB21	0.283	0.320	0.355
D1M	0.655	1.393	0.356

σ_{rms} in case of francium is with 1.4 MeV well above the average σ_{rms} for this model. A more detailed discussion of the individual elements is given below.

7.1.1 Approaching the $N = 82$ Shell Closure With New Silver Masses

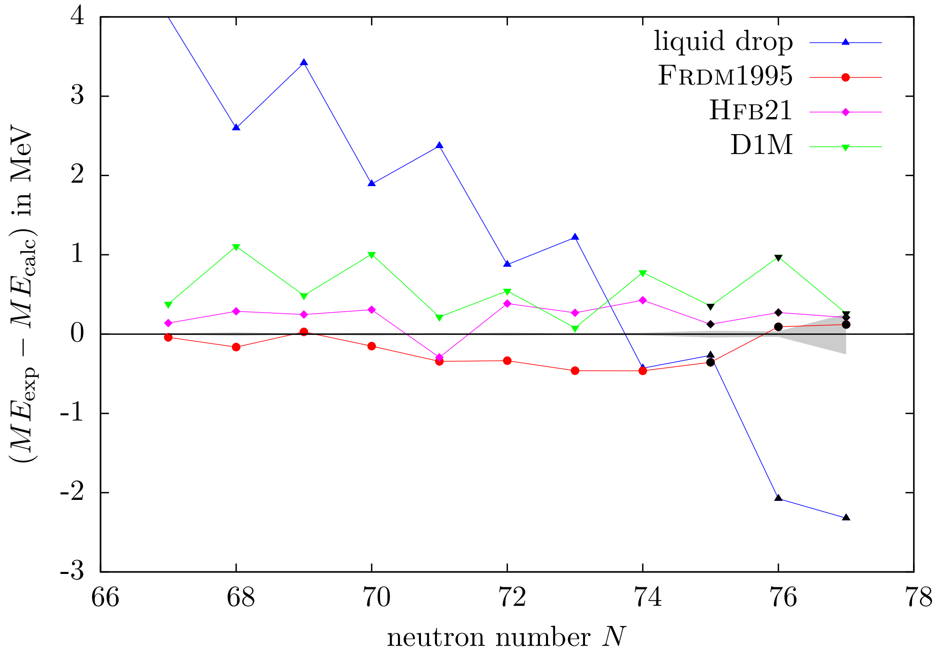

Figure 7.1: *(Color) Comparison of experimental silver data with different mass models. The gray-shaded area denotes the uncertainty of the experimental values. The new values presented in this thesis are marked in black. All experimental values taken from Ref. [9].*

Comparing the experimental silver values with $N = 67{-}77$ with the models mentioned above, the liquid-drop model provides the least agreement (see Fig. 7.1) with $\sigma_{\text{rms}} = 2.336$ MeV. This is expected as no shell or pairing effects are included (see Eq. (3.10)). Its extension, the finite-range droplet model (FRDM), provides a much better agreement ($\sigma_{\text{rms}} = 0.280$ MeV), which is also better than the average agreement for this model in general. Furthermore, it reproduces the pairing correctly, but overestimates the masses slightly. Considering the mean-field models, the HFB21 reproduces the experimental mass values to a similar amount as the FRDM, but underestimates the masses slightly ($\sigma_{\text{rms}} = 0.283$ MeV). For the D1M, an odd-even staggering is visible, indicating that this model does not reproduce the pairing correctly. As the sign of the staggering is opposite to the sign of the staggering for the liquid drop model, the pairing strength seems to be overestimated. Furthermore, the D1M mass values are in general underestimated and hence differ more from the experimental values than the predictions made by the FRDM and HFB21 model ($\sigma_{\text{rms}} = 0.655$ MeV). For the masses newly measured in the context of this thesis ($N = 75 - 77$), a similar agreement with respect to the already known masses with smaller N as shown in Fig. 7.1 is observed.

7.1.2 New Mass Data Towards the $N = 126$ Shell Closure for Francium

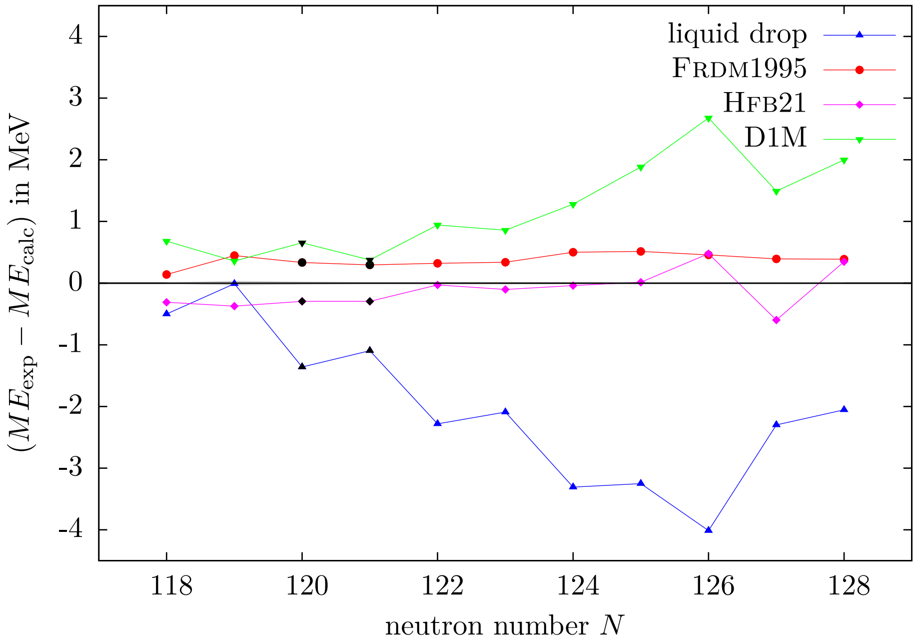

Figure 7.2: *(Color) Comparison of experimental francium data with different mass models. The gray-shaded area denotes the uncertainty of the experimental values. The new values presented in this thesis are marked in black. All experimental values taken from Ref. [147].*

The comparison of the experimental data with theoretical models for the francium chain with $N = 118 - 128$ is indistinct: Not surprisingly, the liquid-drop model fails especially once approaching the shell closure at $N = 126$ ($\sigma_{\text{rms}} = 2.336\,\text{MeV}$) due to the reasons already mentioned for the silver isotopes (see Fig. 7.2). For the FRDM in turn, the agreement is quite well apart from a constant offset ($\sigma_{\text{rms}} = 0.389\,\text{MeV}$): While the FRDM mostly overestimates the masses in case of the silver isotopes, it underestimates the mass in case of the the francium isotopes. For the HFB21, the overall agreement is best with $\sigma_{\text{rms}} = 0.320\,\text{MeV}$, but it reveals problems towards the shell closure. Similar problems but much more pronounced are visible for the D1M model. The latter model reproduces the measurements only less than a factor of two better than the liquid-drop model ($\sigma_{\text{rms}} = 1.393\,\text{MeV}$). However, while the liquid-drop model overestimates the mass values, they are considerably underestimated in the D1M.

7.1.3 Thallium Isotopes Close to the Doubly-Magic ^{208}Pb

Having discussed the silver and francium data already, the comparison of the thallium nuclides with $N = 103 - 114$ reveals the most interesting behavior (see Fig. 7.3): Not only the liquid-drop model shows a large odd-even staggering effect, but all models fail to correctly reproduce the odd-even staggering of the experimental values: For the FRDM1995, the staggering is considerably smaller than for the liquid-drop model but still present. This indicates that the pairing effect is underestimated. This is especially

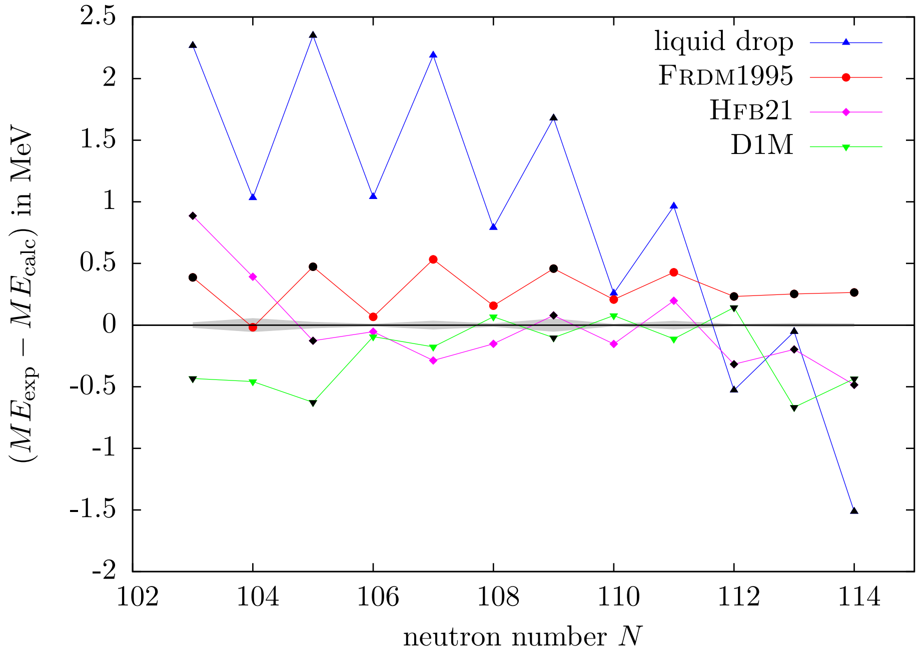

Figure 7.3: *(Color) Comparison of experimental thallium data with different mass models. The gray-shaded area denotes the uncertainty of the experimental values. The new values presented in this thesis are marked in black. All experimental values taken from Ref. [147].*

interesting as for the two other elements discussed before (silver and francium) the strength of the pairing effect included in the FRDM worked reasonable as no significant odd-even staggering is visible (see for comparison Figs. 7.1 and 7.2). Furthermore, an overall underestimation with $\sigma_{\mathrm{rms}} = 0.331\,\mathrm{MeV}$ is observed for this model. Considering the D1M model, an odd-even staggering is visible as well. However, the sign of the staggering is different to the one seen for the macroscopic-based models. This could indicate that the included pairing effect is too strong. The overall agreement of the D1M is nevertheless pretty good with $\sigma_{\mathrm{rms}} = 0.356\,\mathrm{MeV}$. In case of the HFB21, the situation is more difficult: While between $N = 104$ and $N = 108$ the pairing seems to be slightly overestimated as for the D1M, for higher nuclide numbers, the pairing seems to be underestimated similar to the liquid-drop based models. The overall prediction of the masses is comparable to the D1M with $\sigma_{\mathrm{rms}} = 0.355\,\mathrm{MeV}$. In total, one can conclude, that this region is, despite the pairing effects discussed above, obviously quite well reproduced by mass models as the average deviation for the shown models is in all cases smaller than the overall σ_{rms} of the models. Nevertheless, it is astonishing that, in contrast to the silver and francium isotopes, all mass models fail to reproduce the pairing effect of the thallium isotopes properly.

7.2 Nuclear-Structure Studies

Apart from the comparison of the new data with with theoretical mass models, valuable indications about nuclear structure can be drawn from differences of binding energies.

As introduced in Section 3.1, several differences are of special interest: Below, the discussion mainly focuses on the two-neutron separation energies $S_{2\mathrm{n}}$, but in case of the thallium isotopes the two-proton separation energies $S_{2\mathrm{p}}$ as well as the one-proton separation energies S_{p} are discussed as well.

7.2.1 Nuclear Structure Towards the $N = 82$ Shell Closure

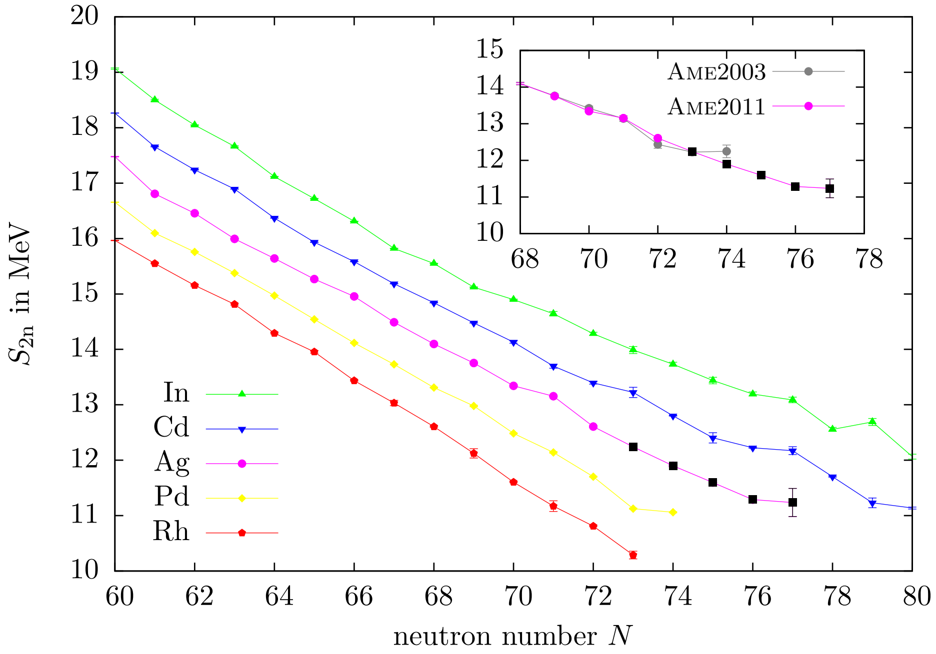

Figure 7.4: *(Color) $S_{2\mathrm{n}}$ values in the silver region. The black dots denote values which have been improved in the context of this thesis. The overall behavior of the $S_{2\mathrm{n}}$ values follows the linear trend. Compared with the values included in the* AME*2003, the $S_{2\mathrm{n}}$ values for silver became smoother (see inset). Values taken from Refs. [9, 144].*

Together with further ISOLTRAP mass measurements on neutron-rich silver isotopes [47], the new measurements presented in the context of this thesis helped to smooth the trend of the silver $S_{2\mathrm{n}}$ values around $N = 73$ compared to the values included in the AME2003 (see inset in Fig. 7.4 for a comparison). These results have been already presented in Ref. [48] and included in the preview to the to-be-published AME2012, here referred to as AME2011 [9]. By providing new silver data, the $S_{2\mathrm{n}}$ values can furthermore help to improve the predictions towards the $N = 82$ shell closure.

Despite the usual smooth trend, a kink in the $S_{2\mathrm{n}}$ trend is visible for the neighboring-Z nuclides around $N = 77$ (see Fig. 7.4). With the new mass value for ^{124}Ag the first hint of a kink in the $S_{2\mathrm{n}}$ values for silver emerges as well. However, the uncertainty on this point is quite high and further nuclides have to be measured before a substantial statement in this direction can be made.

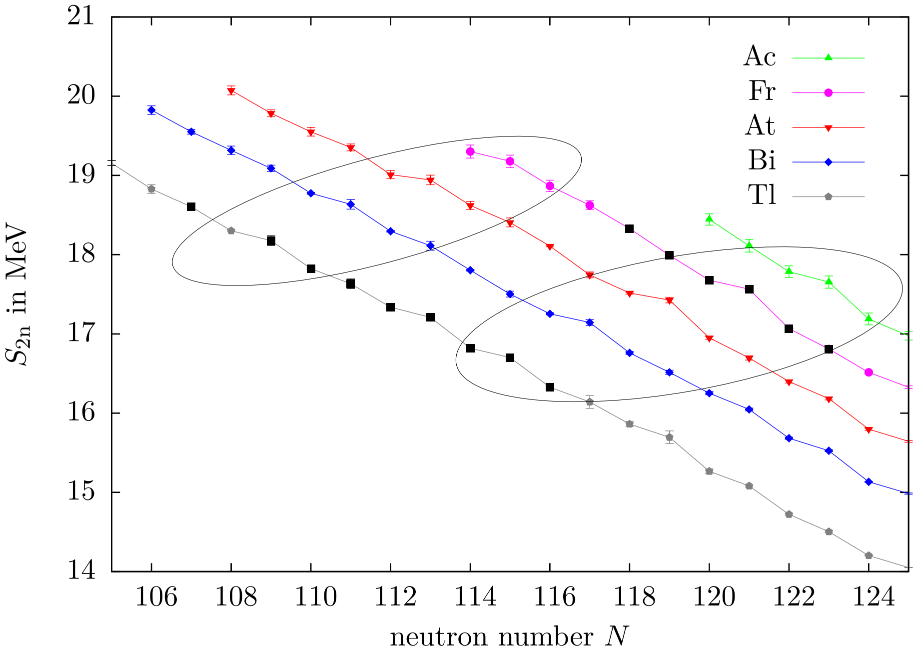

Figure 7.5: *(Color) S_{2n} values in the francium region for odd-Z. The black dots denote values which have been improved in the context of this thesis. Wheareas the overall behavior of the S_{2n} values follows the linear trend, in two regions (see marks) kinks are visible for all odd-Z elements. All values taken from Ref. [147].*

7.2.2 Irregularities in the Separation Energies Around $Z = 87$

The francium S_{2n} values follow in general a very smooth trend (see Fig. 7.5). However, slight kinks occur not only for the francium (in case of $N = 121$), but also for some other nuclides with an odd proton number (e. g. ^{198}At$_{113}$, ^{204}At$_{119}$ or ^{200}Bi$_{117}$). This raises the question whether these observations are real or just measuring artifacts due to inaccurate mass values: In case masses are derived from decay-spectroscopy data, they are easily underestimated by missing levels during the data analysis [163]. Thus, new measurements using a direct measuring technique like PENNING trap mass spectrometry are desirable. In case of the francium isotopes, the kink for $N = 121$ could be confirmed by the new measurements of ^{207,208}Fr. It occurs for the neighboring odd-Z nuclides as well, but the neutron number of its occurrence is shifted with the proton number ($N = 119$ for $Z = 85$, $N = 121$ for $Z = 87$ and $N = 123$ for $Z = 89$). It may be connected as well to the odd-even staggering which is visible for the thallium chain (which is further discussed in the next section). However, the effect seems to be more pronounced for larger Z. Unfortunately, the reason for this observations has to remain unsolved for the moment. As many masses in this region are determined (and linked) via α decay, the observation discussed above may as well have its reason here: One problematic measurement may influence many other nuclides. Hence, more PENNING-trap mass measurements in this region are urgently needed to confirm (or disprove) the observed effect.

7.2.3 Fine-Structure Effect in the Binding Energies of Thallium Isotopes

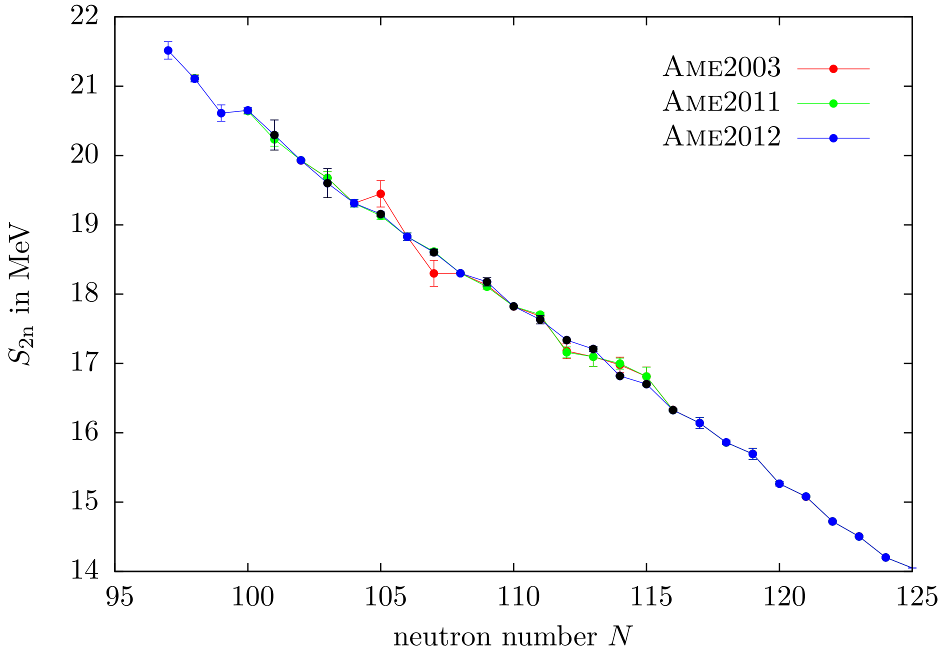

Figure 7.6: *(Color) Change of thallium S_{2n} values. The black dots denote values which have been improved in the context of this thesis. Compared with values already included in the* AME*2003, the S_{2n} values for thallium became smoother.*

With the new data on thallium isotopes, the S_{2n} values for the thallium chain are now considerably smoother than before (see Fig. 7.6). As one can easily see, this is a clear improvement over the situation in previous studies [160], where for the S_{2n} energies of thallium significant irregularities had been observed. While the kinks for ^{184,186}Tl were already corrected before the measurements presented here due to a re-evaluation of existing data in the context of the AME2011, the “ironing” of the region around $N = 113$ is due to the new measurements obtained in the context of this work. The overall trend of the S_{2n} values in this region is now pretty straight (see Fig. 7.7). However, this smoothing of the S_{2n} values is not the end of the story: Subtracting the usual linear trend from the S_{2n} energies, an interesting fine structure is revealed: Odd-even staggering (see Fig. 7.8). This fine structure seems to cover almost the whole chain from $N = 104 - 124$ with changing magnitude and is especially pronounced in the region $N = 108 - 116$. Being on the order of $100 - 200$ keV, it is only visible due to the small uncertainties of the new measurements presented here. Usually the odd-even staggering should be removed by looking at S_{2n} values. The fact that it still occurs so pronounced points towards a stronger change of the pairing energy than usual. This idea of an unusual change of the pairing energy is further supported by the observation of the odd-even staggering visible in the comparison with mass models as discussed in Section 7.1.3. Compared with other elements in this region (see Fig. 7.9), the odd-even staggering is visible in small ranges of other chains as well (e. g. for lead isotopes with $N > 111$). However, it is most pronounced in thallium.

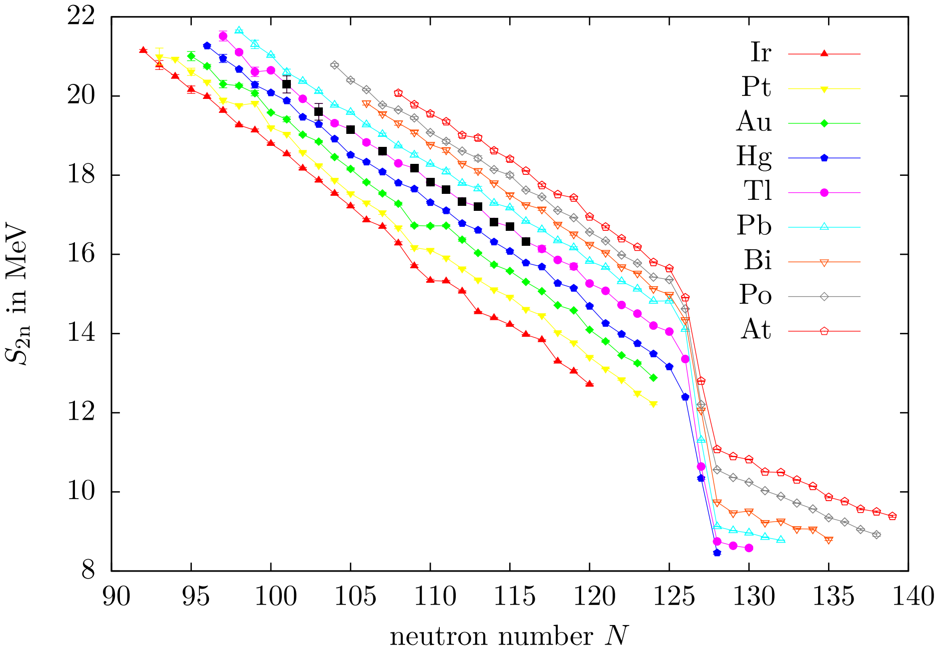

Figure 7.7: *(Color) S_{2n} values in the thallium region. The black dots denote values which have been improved in the context of this thesis. The overall behavior of the S_{2n} values follows the linear trend. Compared to previous discussions, the S_{2n} values for thallium are considerably smoother. The drop of the S_{2n} values around $N = 126$ visualizes the shell close. All values taken from Ref. [147].*

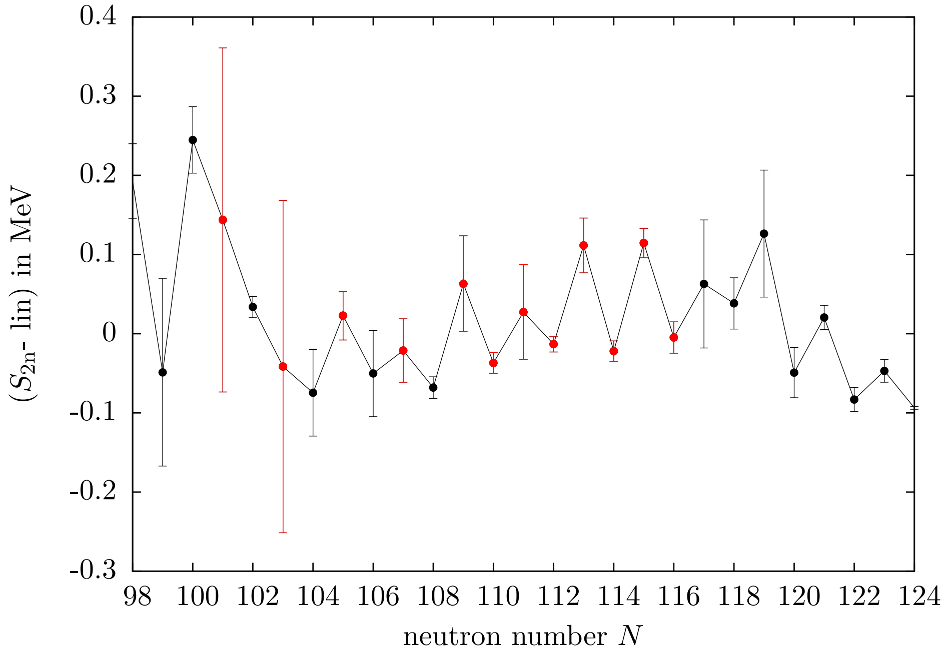

Figure 7.8: *(Color) S_{2n} values for thallium with the linear trend subtracted. A clear odd-even staggering is visible. Red dots denote values influenced by the new measurements presented here. All values taken from Ref. [147].*

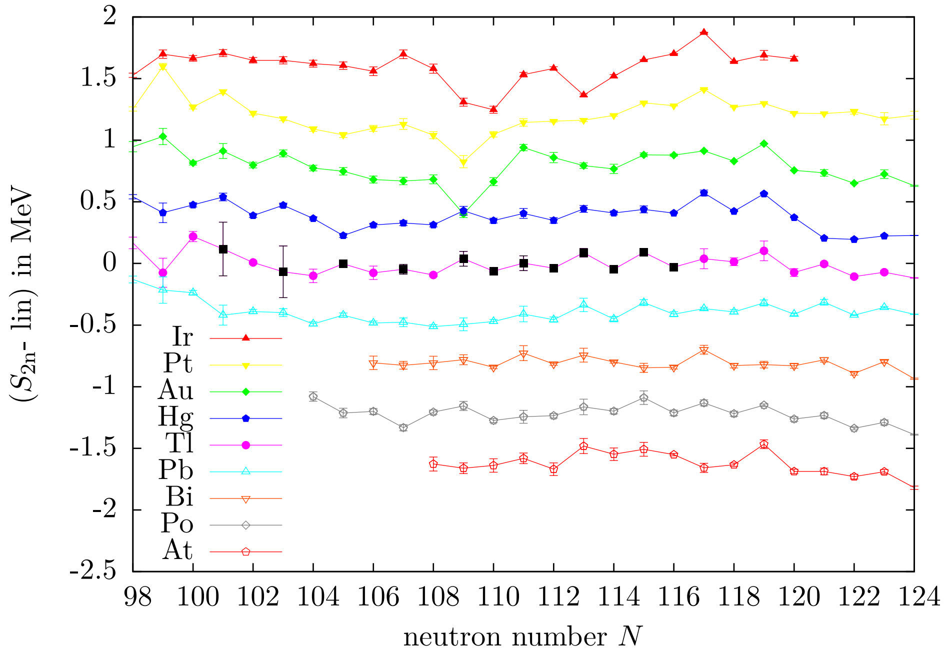

Figure 7.9: *(Color)* S_{2n} *values in the thallium region with the linear trend subtracted. The different elements have been separated by* 0.4 *MeV each for a better visibility. Black dots denote values influenced by the new measurements presented here. All values taken from Ref. [147].*

Looking furthermore at the two-proton separation energies S_{2p} for thallium (see Fig. 7.10), a clear staggering is observed as well, especially in the region $N = 99 - 108$. Compared to the neighboring-Z elements, this behavior is pretty unusual. This phenomena has already been observed in Ref. [160] and is confirmed using the new data. However, for the masses around $N = 113$, the previously observed odd-even staggering is no longer visible taking into account the new measurements. This mystery gets especially puzzling when taking into account as well the S_p values (see Fig. 7.11): Here an odd-even staggering is expected and nicely visible for the neighboring elements (apart from parts of the lead chain). For thallium, however, this staggering is only visible for $N > 115$.

Taking into account the staggering deviation of the experimental data to the mass models, the staggering in the S_{2n} and S_{2p} as well as the (almost) missing staggering in the S_p values, clear indications for an interesting effect are seen. Its origin may be related to the pairing of the neutrons with each other, but as thallium has an unpaired proton just below the closed shell at $Z = 82$, pairing between neutron and proton may be another possible reason for this effect. In Ref. [164], it was pointed out that odd-even staggering of binding energies may have its origin not only in surface pairing effects but as well in a polarization of the core. This was consequently demonstrated in a recent publication [165] and may pose a possible explanation for the observed effects in thallium as well. However, detailed theoretical calculations would be required to investigate this. The region around $Z = 81$ is furthermore well known for shape coexistence (see Section 3.3 and Ref. [15]). This discussion started after a large odd-even staggering for the

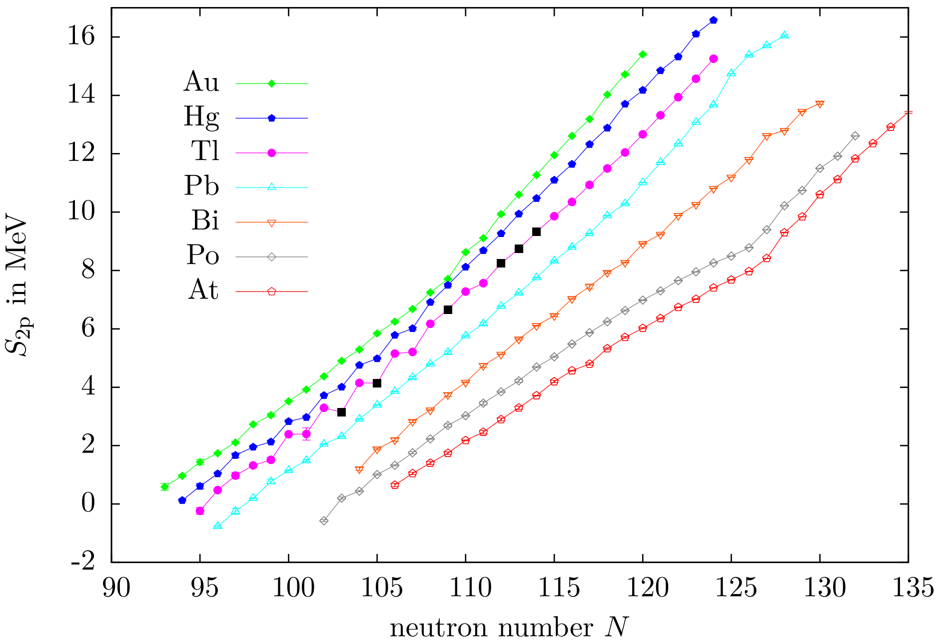

Figure 7.10: *(Color) S_{2p} values in the thallium region. The black dots denote values which have been improved in the context of this thesis. A clear odd-even staggering for Tl is visible. All values taken from Ref. [147].*

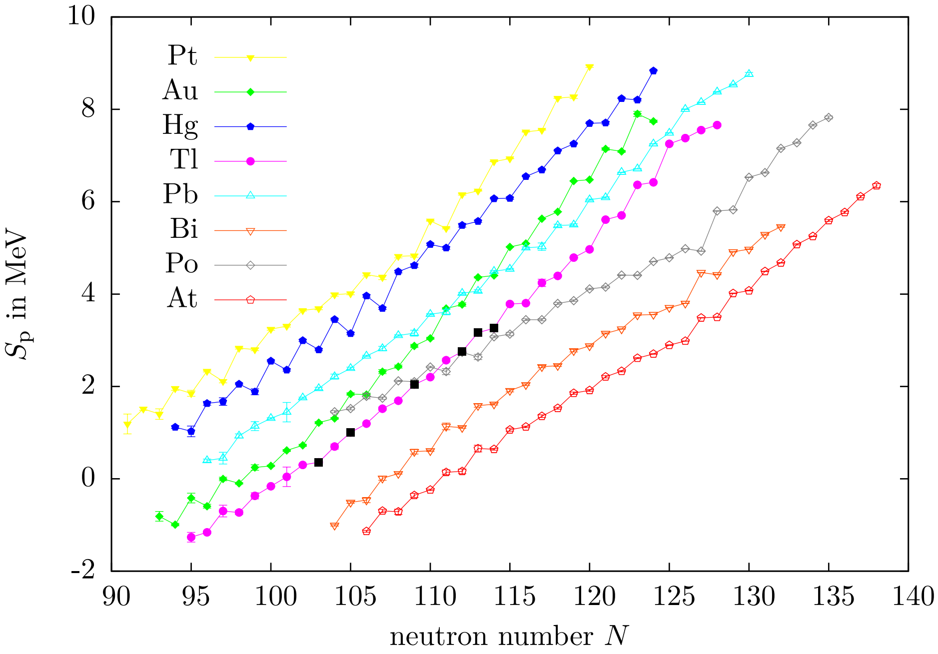

Figure 7.11: *(Color) S_p values in the thallium region. The black dots denote values which have been improved in the context of this thesis. All values taken from Ref. [147].*

charge radii of the mercury isotopes had been observed [12, 166]. Later-on, also the charge radii of the thallium chain have been studied in various experiments [12]. A comparison of the odd-even staggering in the thallium $S_{2\mathrm{n}}$ energies presented here with the effects observed for the charge radii will be given elsewhere [167].

8 Summary and Outlook

In the technical part of the present work, the LabView-based control system of the Isoltrap experiment has been enhanced and adapted to the current requirements: Several new devices have been implemented and the number of available timing channels for synchronization of the setup has been increased to allow the integration of setup extensions like the MR-ToF mass separator and the decay spectroscopy setup. Furthermore, the whole control system has been migrated to a new LabView version. As a main enhancement a new operation mode, the stacking mode, has been introduced. Together with improvements of the Isoltrap buncher, it is now possible to accumulate ions in the preparation Penning trap over several measurement cycles. These ions are then transferred as one bunch to the precision trap for the actual mass determination. In case of low production rates (and sufficiently long half-life), this mode reduces the measurement time significantly as the most time-consuming excitations in the Penning traps are only performed once per bunch. Furthermore, if part of the beam cleaning can be performed using the MR-ToF mass separator, the stacking mode enables the Isoltrap experiment to deal with higher amounts of contaminating ions, hence preparing the Isoltrap experiment for future challenges. Several measurements performed in 2012 could only be carried out successfully with use of this enhancement. One example is the mass measurement of ^{82}Zn, which had failed several times before at different facilities because of low production rates and large amounts of contaminating ions. This mass is of particular interest in nuclear astrophysics for the understanding of neutron stars and will be presented in an upcoming publication [127].

On the physics side of the present work, the ground-state masses of $^{122-124}$Ag, ^{207,208}Fr and ^{184,186,194,195}Tl as well as the masses of isomeric states of ^{186,190,193,194,195}Tl have been determined. The uncertainty of most of these mass values could be improved significantly (up to a factor of 20) and several of them could be measured for the first time. Furthermore, the influence of correlations between frequency ratios due to shared references has been studied for the first time at Isoltrap. However, the corrections to the frequency ratios and their uncertainties turned out to be rather small.

Following the data analysis, mass models have been tested and nuclear-structure studies have been carried out using the new mass values. The new mass values of silver isotopes in the vicinity of the doubly-magic ^{132}Sn and the $N = 82$ shell closure continue the smooth trend of the already known $S_{2\mathrm{n}}$ energies. Hence, more accurate prediction of masses towards the shell closure at ^{129}Ag are now possible.

In case of the francium isotopes, the kink in the $S_{2\mathrm{n}}$ values around ^{208}Fr is reproduced and rendered more precisely by the measurements presented here. This region is currently under investigation using laser spectroscopy as well [168, 169]. Topics of interest in this context are measurements of the atomic hyperfine levels to investigate a possible change of the nuclear ground-state energy levels with decreasing neutron number indicating a possible octupole deformation [170] as well as the determination of the β-decay properties using laser-assisted decay spectroscopy [171]. The new mass measurements provide valuable absolute anchor points for the level scheme and may furthermore support the discussion of nuclear shapes above the $Z = 82$ shell closure. More mass measurements in this region are of particular interest to provide additional anchor points and to resolve problematic links due to masses derived from decay-spectroscopy measurements.

For the thallium masses an interesting fine-structure odd-even staggering of the $S_{2\mathrm{n}}$ energies was revealed. This fine structure points towards an unusual change of the pairing with increasing neutron number. Furthermore, all discussed global mass models fail to reproduce the pairing effect correctly. Consequently, these observations are particularly suitable for a theoretical study of the residual proton-neutron interaction in an independent particle approach as for thallium only one proton is missing from a closed shell. In addition, the thallium isotopic chain is currently under investigation by means of laser spectroscopy in combination with decay spectroscopy [172]. The presented mass measurements are hence an important step to provide absolute anchor points for building level schemes. All this contributes to an understanding of shape coexistence and shape staggering in this region. A further investigation of this issue, especially with respect to a comparison with charge-radii measurements and a discussion of the pairing gap energies, will be presented in another work [167]. Furthermore, a detailed examination of the isomeric states in thallium including spin systematics will be given elsewhere [161]. As a next step, a precise mass measurement of ^{180,182}Tl would be desirable, as this could determine whether the odd-even staggering continues as well for $N < 104$. The mass of the α-decay daughter of ^{184}Tl, ^{180}Au is currently of high interest for building up the level scheme for the α decay [156]. The presented measurements already contributed to this discussion, but additional measurements are necessary.

Looking into the ISOLTRAP future, a long shutdown is coming up beginning at the end of 2012 because of the shutdown of the accelerator chain at CERN and the construction work related to HIE-ISOLDE, an extension of the ISOLDE facility. This shutdown will be used for enhanced maintenance of the ISOLTRAP setup, including a refurbishment of the superconducting magnet housing the precision trap, which has been running continuously for the last 20 years. On the control system side, a change of the operating system from Windows XP to Windows 7 will be necessary as the support for Windows XP will be phased out at CERN with the beginning of the long shutdown. A further motivation for the change to Windows 7 will be a new version of the measurement GUI, MM8, which is currently being developed at Michigan State University [173]. On the physics side, one could turn towards lighter masses, e. g. neutron-rich copper isotopes for studying the behavior of binding energies towards the doubly-magic ^{78}Ni. Furthermore, mass measurements of chromium and scandium in the region around $N = 32$ and $N = 34$ would be of high interest as these masses could contribute to the discussion whether these respective neutron numbers become magic numbers in this part of the nuclear chart. Part of these measurements could be carried out as well using the MR-ToF device instead of the PENNING traps as already suggested in Ref. [174]: As the mass separation process in the MR-ToF device is considerably faster than in the PENNING traps, this could significantly reduce decay losses in case of short-lived nuclides like ^{55}Sc, hence allowing measurements which might not be possible otherwise.

Bibliography

[1] H. Geiger and E. Marsden. *On a Diffuse Reflection of the α-Particles.* Proc. R. Soc. Lond. A **82** (1909) 495–500. URL `http://dx.doi.org/10.1098/rspa.1909.0054`.

[2] E. Rutherford. *LXXIX. The Scattering of α and β Particles by Matter and the Structure of the Atom.* Philos. Mag. Series 6 **21** (1911) 669–688. URL `http://dx.doi.org/10.1080/14786440508637080`.

[3] J. Chadwick. *Possible Existence of a Neutron.* Nature **129** (1932) 312. URL `http://dx.doi.org/10.1038/129312a0`.

[4] C. F. v. Weizsäcker. *Zur Theorie der Kernmassen.* Z. Phys. A **96** (1935) 431–458. URL `http://dx.doi.org/10.1007/BF01337700`.

[5] C. F. v. Weizsäcker. *Metastabile Zustände der Atomkerne.* Naturwissenschaften **24** (1936) 813–814. URL `http://dx.doi.org/10.1007/BF01497732`.

[6] M. Goeppert-Mayer. *On Closed Shells in Nuclei.* Phys. Rev. **74** (1948) 235–239. URL `http://dx.doi.org/10.1103/PhysRev.74.235`.

[7] O. Haxel, J. H. D. Jensen, and H. E. Suess. *On the "Magic Numbers" in Nuclear Structure.* Phys. Rev. **75** (1949) 1766–1766. URL `http://dx.doi.org/10.1103/PhysRev.75.1766.2`.

[8] M. Goeppert-Mayer. *On Closed Shells in Nuclei. II.* Phys. Rev. **75** (1949) 1969–1970. URL `http://dx.doi.org/10.1103/PhysRev.75.1969`.

[9] G. Audi and W. Meng. Private Communication (2011). URL `http://amdc.in2p3.fr/masstables/Ame2011int/filel.html`.

[10] M. Huyse. *The Why and How of Radioactive-Beam Research.* In: J. Al-Khalili and E. Roeckl (eds.), *The Euroschool Lectures on Physics with Exotic Beams, Vol. I*, volume 651 of *Lecture Notes in Physics*, 1–32. Springer Berlin / Heidelberg (2004). URL `http://dx.doi.org/10.1007/978-3-540-44490-9`.

[11] B. Rubio and W. Gelletly. *Beta Decay of Exotic Nuclei.* In: J. Al-Khalili and E. Roeckl (eds.), *The Euroschool Lectures on Physics with Exotic Beams, Vol. III*, volume 764 of *Lecture Notes in Physics*, 99–151. Springer Berlin / Heidelberg (2009). URL `http://dx.doi.org/10.1007/978-3-540-85839-3`.

[12] H.-J. Kluge and W. Nörtershäuser. *Lasers for nuclear physics.* Spectrochim. Acta, Part B **58** (2003) 1031–1045. URL `http://dx.doi.org/10.1016/S0584-8547(03)00063-6`.

[13] G. Neyens. *Nuclear magnetic and quadrupole moments for nuclear structure research on exotic nuclei.* Rep. Prog. Phys. **66** (2003) 633. URL `http://dx.doi.org/10.1088/0034-4885/66/4/205`.

[14] A. Görgen. *Shapes and collectivity of exotic nuclei via low-energy Coulomb excitation.* J. Phys. G: Nucl. Part. Phys. **37** (2010) 103101. URL `http://dx.doi.org/10.1088/0954-3899/37/10/103101`.

[15] K. Heyde and J. L. Wood. *Shape coexistence in atomic nuclei.* Rev. Mod. Phys. **83** (2011) 1467–1521. URL `http://dx.doi.org/10.1103/RevModPhys.83.1467`.

[16] D. Lunney, J. M. Pearson, and C. Thibault. *Recent trends in the determination of nuclear masses.* Rev. Mod. Phys. **75** (2003) 1021–1082. URL `http://dx.doi.org/10.1103/RevModPhys.75.1021`.

[17] K. Blaum. *High-accuracy mass spectrometry with stored ions.* Phys. Rep. **425** (2006) 1–78. URL `http://dx.doi.org/10.1016/j.physrep.2005.10.011`.

[18] G. Münzenberg. *The separation techniques for secondary beams.* Nucl. Instrum. Methods Phys. Res. B **70** (1992) 265–275. URL `http://dx.doi.org/10.1016/0168-583X(92)95942-K`.

[19] S. Hofmann and G. Münzenberg. *The discovery of the heaviest elements.* Rev. Mod. Phys. **72** (2000) 733–767. URL `http://dx.doi.org/10.1103/RevModPhys.72.733`.

[20] U. Köster. *Intense radioactive-ion beams produced with the ISOL method.* Eur. Phys. J. A **15** (2002) 255–263. URL `http://dx.doi.org/10.1140/epja/i2001-10264-2`.

[21] J. Ketelaer. *The construction of TRIGA-TRAP and direct high-precision Penning trap mass measurements on rare-earth elements and americium.* Ph.D. thesis, Johannes Gutenberg-Universität, Mainz, Germany (2010). URL `http://ubm.opus.hbz-nrw.de/volltexte/2010/2418/`.

[22] B. Franzke. *The heavy ion storage and cooler ring project ESR at GSI.* Nucl. Instrum. Methods Phys. Res. B **24–25, Part 1** (1987) 18–25. URL `http://dx.doi.org/10.1016/0168-583X(87)90583-0`.

[23] A. Estradé et al. *Time-of-Flight Mass Measurements for Nuclear Processes in Neutron Star Crusts.* Phys. Rev. Lett. **107** (2011) 172503. URL `http://dx.doi.org/10.1103/PhysRevLett.107.172503`.

[24] H. Savajols. *The SPEG Mass Measurement Program at GANIL.* Hyperfine Interact. **132** (2001) 243–252. URL `http://dx.doi.org/10.1023/A:1011964401634`.

[25] Yu. A. Litvinov et al. *Mass measurement of cooled neutron-deficient bismuth projectile fragments with time-resolved Schottky mass spectrometry at the FRS-ESR facility.* Nucl. Phys. A **756** (2005) 3–38. URL `http://dx.doi.org/10.1016/j.nuclphysa.2005.03.015`.

[26] M. Block et al. *Towards direct mass measurements of nobelium at SHIPTRAP.* Eur. Phys. J. D **45** (2007) 39–45. URL `http://dx.doi.org/10.1140/epjd/e2007-00189-2`.

[27] M. Mukherjee et al. *ISOLTRAP: An on-line Penning trap for mass spectrometry on short-lived nuclides.* Eur. Phys. J. A **35** (2008) 1–29. URL `http://dx.doi.org/10.1140/epja/i2007-10528-9`.

[28] E. Kugler. *The ISOLDE facility.* Hyperfine Interact. **129** (2000) 23–42. URL `http://dx.doi.org/10.1023/A:1012603025802`.

[29] T. W. Hänsch. *Nobel Lecture: Passion for precision.* Rev. Mod. Phys. **78** (2006) 1297–1309. URL `http://dx.doi.org/10.1103/RevModPhys.78.1297`.

[30] L. S. Brown and G. Gabrielse. *Geonium theory: Physics of a single electron or ion in a Penning trap.* Rev. Mod. Phys. **58** (1986) 233–311. URL `http://dx.doi.org/10.1103/RevModPhys.58.233`.

[31] H. Dehmelt. *Experiments with an isolated subatomic particle at rest.* Rev. Mod. Phys. **62** (1990) 525–530. URL `http://dx.doi.org/10.1103/RevModPhys.62.525`.

[32] F. M. Penning. *Die Glimmentladung bei niedrigem Druck zwischen koaxialen Zylindern in einem axialen Magnetfeld.* Physica **3** (1936) 873–894. URL `http://dx.doi.org/10.1016/S0031-8914(36)80313-9`.

[33] G. Bollen et al. *The accuracy of heavy-ion mass measurements using time of flight-ion cyclotron resonance in a Penning trap.* J. Appl. Phys. **68** (1990) 4355–4374. URL `http://dx.doi.org/10.1063/1.346185`.

[34] G. Werth. *Principles of Ion Traps.* In: *Trapped Charged Particles and Fundamental Interactions*, volume 749 of *Lecture Notes in Physics*, 1–37. Springer Berlin / Heidelberg (2008). URL `http://dx.doi.org/10.1007/978-3-540-77817-2`.

[35] M. Rosenbusch et al. *A study of octupolar excitation for mass-selective centering in Penning traps.* Int. J. Mass Spectrom. **314** (2012) 6–12. URL `http://dx.doi.org/10.1016/j.ijms.2012.01.002`.

[36] G. Savard et al. *A new cooling technique for heavy ions in a Penning trap.* Phys. Lett. A **158** (1991) 247–252. URL `http://dx.doi.org/10.1016/0375-9601(91)91008-2`.

[37] S. Schwarz. *Simulations for Ion Traps Buffer Gas Cooling.* In: K. Blaum and F. Herfurth (eds.), *Trapped Charged Particles and Fundamental Interactions*, volume 749 of *Lecture Notes in Physics*, 1–21. Springer Berlin / Heidelberg (2008). URL `http://dx.doi.org/10.1007/978-3-540-77817-2`.

[38] M. König et al. *Quadrupole excitation of stored ion motion at the true cyclotron frequency.* Int. J. Mass Spectrom. **142** (1995) 95–116. URL `http://dx.doi.org/10.1016/0168-1176(95)04146-C`.

[39] E. Rutherford et al. *Discussion on the Structure of Atomic Nuclei.* Proc. R. Soc. Lond. A **123** (1929) 373–390. URL `http://dx.doi.org/10.1098/rspa.1929.0074`.

[40] G. Gamow. *Mass Defect Curve and Nuclear Constitution.* Proc. R. Soc. Lond. A **126** (1930) 632–644. URL `http://dx.doi.org/10.1098/rspa.1930.0032`.

[41] W. Heisenberg. *Über den Bau der Atomkerne. I.* Z. Phys. A **77** (1932) 1–11. URL `http://dx.doi.org/10.1007/BF01342433`.

[42] W. Heisenberg. *Über den Bau der Atomkerne. II.* Z. Phys. A **78** (1932) 156–164. URL `http://dx.doi.org/10.1007/BF01337585`.

[43] M. Goeppert-Mayer. *The Shell Model.* In: *Nobel Lectures, Physics 1963–1970.* Elsevier Publishing Company, Amsterdam (1972).

[44] M. Goeppert-Mayer. *Nuclear Configurations in the Spin-Orbit Coupling Model. I. Empirical Evidence.* Phys. Rev. **78** (1950) 16–21. URL `http://dx.doi.org/10.1103/PhysRev.78.16`.

[45] A. Einstein. *Ist die Trägheit eines Körpers von seinem Energieinhalt abhängig?* Ann. Phys. **323** (1905) 639–641. URL `http://dx.doi.org/10.1002/andp.19053231314`.

[46] G. Audi, A. H. Wapstra, and C. Thibault. *The 2003 atomic mass evaluation: (II). Tables, graphs and references.* Nucl. Phys. A **729** (2003) 337–676. URL `http://dx.doi.org/10.1016/j.nuclphysa.2003.11.003`.

[47] M. Breitenfeldt. *Mass measurements on short-lived Cd and Ag nuclides at the online mass spectrometer ISOLTRAP.* Ph.D. thesis, Universität Greifswald, Germany (2009). URL `http://ub-ed.ub.uni-greifswald.de/opus/volltexte/2009/666/`.

[48] M. Breitenfeldt et al. *Approaching the* $N = 82$ *shell closure with mass measurements of Ag and Cd isotopes.* Phys. Rev. C **81** (2010) 034313. URL `http://dx.doi.org/10.1103/PhysRevC.81.034313`.

[49] A. Martín et al. *Mass measurements of neutron-deficient radionuclides near the end-point of the rp-process with SHIPTRAP.* Eur. Phys. J. A **34** (2007) 341–348. URL `http://dx.doi.org/10.1140/epja/i2007-10520-5`.

[50] V. Elomaa et al. *Light-ion-induced reactions in mass measurements of neutron-deficient nuclides close to* $A = 100$*.* Eur. Phys. J. A **40** (2009) 1–9. URL `http://dx.doi.org/10.1140/epja/i2008-10732-1`.

[51] Ch. Borgmann et al. *Cadmium mass measurements between the neutron shell closures at* $N = 50$ *and 82.* AIP Conf. Proc. **1377** (2011) 332–334. URL `http://dx.doi.org/10.1063/1.3628403`.

[52] D. G. Madland and J. Nix. *New model of the average neutron and proton pairing gaps.* Nucl. Phys. A **476** (1988) 1–38. URL `http://dx.doi.org/10.1016/0375-9474(88)90370-3`.

[53] O. Hahn. *Über ein neues radioaktives Zerfallsprodukt im Uran.* Naturwissenschaften **9** (1921) 84–84. URL `http://dx.doi.org/10.1007/BF01491321`.

[54] G. Audi et al. *The NUBASE evaluation of nuclear and decay properties.* Nucl. Phys. A **729** (2003) 3–128. URL `http://dx.doi.org/10.1016/j.nuclphysa.2003.11.001`.

[55] P. Walker and G. Dracoulis. *Energy traps in atomic nuclei.* Nature **399** (1999) 35–40. URL `http://dx.doi.org/10.1038/19911`.

[56] M. Arnould, S. Goriely, and K. Takahashi. *The r-process of stellar nucleosynthesis: Astrophysics and nuclear physics achievements and mysteries.* Phys. Rep. **450** (2007) 97–213. URL `http://dx.doi.org/10.1016/j.physrep.2007.06.002`.

[57] M. Busso, R. Gallino, and G. J. Wasserburg. *Nucleosynthesis in Asymptotic Giant Branch Stars: Relevance for Galactic Enrichment and Solar System Formation.* Annu. Rev. Astron. Astrophys. **37** (1999) 239–309. URL `http://dx.doi.org/10.1146/annurev.astro.37.1.239`.

[58] M. Arnould and S. Goriely. *The p-process of stellar nucleosynthesis: astrophysics and nuclear physics status.* Phys. Rep. **384** (2003) 1–84. URL `http://dx.doi.org/10.1016/S0370-1573(03)00242-4`.

[59] H. A. Bethe and R. F. Bacher. *Nuclear Physics A. Stationary States of Nuclei.* Rev. Mod. Phys. **8** (1936) 82–229. URL `http://dx.doi.org/10.1103/RevModPhys.8.82`.

[60] W. D. Myers and W. J. Swiatecki. *Nuclear masses and deformations.* Nucl. Phys. **81** (1966) 1–60. URL `http://dx.doi.org/10.1016/0029-5582(66)90639-0`.

[61] G. Audi and A. H. Wapstra. *The 1995 update to the atomic mass evaluation.* Nucl. Phys. A **595** (1995) 409–480. URL `http://dx.doi.org/10.1016/0375-9474(95)00445-9`.

[62] gnuplot Homepage (2012). URL `http://www.gnuplot.info/`.

[63] R. D. Woods and D. S. Saxon. *Diffuse Surface Optical Model for Nucleon-Nuclei Scattering.* Phys. Rev. **95** (1954) 577–578. URL `http://dx.doi.org/10.1103/PhysRev.95.577`.

[64] B. A. Brown. *Lecture Notes in Nuclear Structure Physics.* online (2005). URL `http://www.nscl.msu.edu/~brown/Jina-workshop/BAB-lecture-notes.pdf`.

[65] M. Bender, P.-H. Heenen, and P.-G. Reinhard. *Self-consistent mean-field models for nuclear structure.* Rev. Mod. Phys. **75** (2003) 121–180. URL `http://dx.doi.org/10.1103/RevModPhys.75.121`.

[66] R. Machleidt and I. Slaus. *The nucleon-nucleon interaction.* J. Phys. G: Nucl. Part. Phys. **27** (2001) R69. URL `http://dx.doi.org/10.1088/0954-3899/27/5/201`.

[67] R. Vinh Mau. *The theory of the nucleon-nucleon interaction.* In: J. Arias and M. Lozano (eds.), *An Advanced Course in Modern Nuclear Physics*, volume 581 of *Lecture Notes in Physics*, 1–38. Springer Berlin / Heidelberg (2001). URL `http://dx.doi.org/10.1007/3-540-44620-6`.

[68] R. B. Wiringa, V. G. J. Stoks, and R. Schiavilla. *Accurate nucleon-nucleon potential with charge-independence breaking.* Phys. Rev. C **51** (1995) 38–51. URL `http://dx.doi.org/10.1103/PhysRevC.51.38`.

[69] S. Veerasamy and W. N. Polyzou. *Momentum-space Argonne V18 interaction.* Phys. Rev. C **84** (2011) 034003. URL `http://dx.doi.org/10.1103/PhysRevC.84.034003`.

[70] S. C. Pieper. *The Illinois Extension to the Fujita-Miyazawa Three-Nucleon Force.* AIP Conf. Proc. **1011** (2008) 143–152. URL `http://dx.doi.org/10.1063/1.2932280`.

[71] M. Baldo and A. E. Shaban. *Dependence of the nuclear equation of state on two-body and three-body forces.* Phys. Lett. B **661** (2008) 373–377. URL `http://dx.doi.org/10.1016/j.physletb.2008.02.040`.

[72] R. Machleidt, K. Holinde, and Ch. Elster. *The bonn meson-exchange model for the nucleon—nucleon interaction.* Phys. Rep. **149** (1987) 1–89. URL `http://dx.doi.org/10.1016/S0370-1573(87)80002-9`.

[73] R. Machleidt. *High-precision, charge-dependent Bonn nucleon-nucleon potential.* Phys. Rev. C **63** (2001) 024001. URL `http://dx.doi.org/10.1103/PhysRevC.63.024001`.

[74] E. de Guerra. *The limits of the mean field.* In: J. Arias and M. Lozano (eds.), *An Advanced Course in Modern Nuclear Physics*, volume 581 of *Lecture Notes in Physics*, 155–194. Springer Berlin / Heidelberg (2001). URL `http://dx.doi.org/10.1007/3-540-44620-6`.

[75] T. H. R. Skyrme. *CVII. The nuclear surface.* Philos. Mag. **1** (1956) 1043–1054. URL `http://dx.doi.org/10.1080/14786435608238186`.

[76] J. Dechargé and D. Gogny. *Hartree-Fock-Bogolyubov calculations with the* $D1$ *effective interaction on spherical nuclei.* Phys. Rev. C **21** (1980) 1568–1593. URL `http://dx.doi.org/10.1103/PhysRevC.21.1568`.

[77] F. Tondeur et al. *Towards a Hartree-Fock mass formula.* Phys. Rev. C **62** (2000) 024308. URL `http://dx.doi.org/10.1103/PhysRevC.62.024308`.

[78] M. Samyn et al. *A Hartree–Fock–Bogoliubov mass formula.* Nucl. Phys. A **700** (2002) 142–156. URL `http://dx.doi.org/10.1016/S0375-9474(01)01316-1`.

[79] S. Goriely, N. Chamel, and J. M. Pearson. *Further explorations of Skyrme-Hartree-Fock-Bogoliubov mass formulas. XII. Stiffness and stability of neutron-star matter.* Phys. Rev. C **82** (2010) 035804. URL `http://dx.doi.org/10.1103/PhysRevC.82.035804`.

[80] S. Goriely et al. *First Gogny-Hartree-Fock-Bogoliubov Nuclear Mass Model.* Phys. Rev. Lett. **102** (2009) 242501. URL `http://dx.doi.org/10.1103/PhysRevLett.102.242501`.

[81] P. Möller et al. *Nuclear Ground-State Masses and Deformations.* At. Data Nucl. Data Tables **59** (1995) 185–381. URL `http://dx.doi.org/10.1006/adnd.1995.1002`.

[82] P. Möller et al. *New Finite-Range Droplet Mass Model and Equation-of-State Parameters.* Phys. Rev. Lett. **108** (2012) 052501. URL `http://dx.doi.org/10.1103/PhysRevLett.108.052501`.

[83] W. D. Myers and W. J. Swiatecki. *Average nuclear properties.* Ann. Phys. (NY) **55** (1969) 395–505. URL `http://dx.doi.org/10.1016/0003-4916(69)90202-4`.

[84] W. D. Myers and W. J. Swiatecki. *The nuclear droplet model for arbitrary shapes.* Ann. Phys. (NY) **84** (1974) 186–210. URL `http://dx.doi.org/10.1016/0003-4916(74)90299-1`.

[85] P. Möller and J. R. Nix. *Nuclear mass formula with a Yukawa-plus-exponential macroscopic model and a folded-Yukawa single-particle potential.* Nucl. Phys. A **361** (1981) 117–146. URL `http://dx.doi.org/10.1016/0375-9474(81)90473-5`.

[86] J. Treiner et al. *Bulk compression due to surface tension in Hartree-Fock, Thomas-Fermi and Droplet-model calculations.* Nucl. Phys. A **452** (1986) 93–104. URL `http://dx.doi.org/10.1016/0375-9474(86)90510-5`.

[87] K. Riisager et al. (eds.). *HIE-ISOLDE: the Scientific Opportunities.* CERN, Geneva, Switzerland (2007). URL `https://cdsweb.cern.ch/record/1078363`. CERN-2007-008.

[88] R. Catherall et al. *Radioactive ion beams produced by neutron-induced fission at ISOLDE.* Nucl. Instrum. Methods Phys. Res. B **204** (2003) 235–239. URL `http://dx.doi.org/10.1016/S0168-583X(02)01915-8`.

[89] J. R. J. Bennett. *A Single Pulse Method for Measuring the Release Curves of Radioactive Nuclear Beam Targets.* In: S. Myers et al. (eds.), *6th European Particle Accelerator Conference*, 2383. Stockholm, Sweden (1998). URL `http://cdsweb.cern.ch/record/858931`.

[90] ISOLDE Homepage (2012). URL `http://isolde.web.cern.ch/isolde`.

[91] M. Kowalska. *Minutes of the 39th Meeting of the INTC on 2-3 February 2011.* Technical Report CERN-INTC-2011-025. INTC-039, CERN, Geneva (2011). URL `http://cdsweb.cern.ch/record/1331527/`.

[92] L. Penescu et al. *Development of high efficiency Versatile Arc Discharge Ion Source at CERN ISOLDE.* Rev. Sci. Instrum. **81** 02A906. URL `http://dx.doi.org/10.1063/1.3271245`.

[93] V. N. Fedosseev et al. *ISOLDE RILIS: New beams, new facilities.* Nucl. Instrum. Methods Phys. Res. B **266** (2008) 4378–4382. URL `http://dx.doi.org/10.1016/j.nimb.2008.05.038`.

[94] V. N. Fedosseev et al. *Upgrade of the resonance ionization laser ion source at ISOLDE on-line isotope separation facility: New lasers and new ion beams.* Rev. Sci. Instrum. **83** 02A903. URL `http://dx.doi.org/10.1063/1.3662206`.

[95] T. Giles. Private Communication (2012).

[96] V. Barozier. Private Communication (2012).

[97] J. L. Wiza. *Microchannel plate detectors.* Nucl. Instrum. Methods **162** (1979) 587–601. URL `http://dx.doi.org/10.1016/0029-554X(79)90734-1`.

[98] K. Blaum et al. *Carbon clusters for absolute mass measurements at ISOLTRAP.* Eur. Phys. J. A **15** (2002) 245–248. URL `http://dx.doi.org/10.1140/epja/i2001-10262-4`.

[99] D. Fink et al. *Q Value and Half-Lives for the Double-β-Decay Nuclide* ^{110}Pd. Phys. Rev. Lett. **108** (2012) 062502. URL `http://dx.doi.org/10.1103/PhysRevLett.108.062502`.

[100] F. Herfurth et al. *A linear radiofrequency ion trap for accumulation, bunching, and emittance improvement of radioactive ion beams.* Nucl. Instrum. Methods Phys. Res. A **469** (2001) 254–275. URL `http://dx.doi.org/10.1016/S0168-9002(01)00168-1`.

[101] R. Wolf et al. *A multi-reflection time-of-flight mass separator for isobaric purification of radioactive ion beams.* Hyperfine Interact. **199** (2011) 115–122. URL `http://dx.doi.org/10.1007/s10751-011-0306-8`.

[102] R. N. Wolf et al. *Static-mirror ion capture and time focusing for electrostatic ion-beam traps and multi-reflection time-of-flight mass analyzers by use of an in-trap potential lift.* Int. J. Mass Spectrom. **313** (2012) 8–14. URL `http://dx.doi.org/10.1016/j.ijms.2011.12.006`.

[103] SIMION Homepage (2012). URL `http://simion.com/`.

[104] S. Naimi. *Onsets of nuclear deformation from measurments with the ISOLTRAP mass spectrometer.* Ph.D. thesis, Université Paris-Diderot - Paris VII (2010). URL `http://tel.archives-ouvertes.fr/tel-00548779`.

[105] M. Kowalska et al. *Trap-assisted decay spectroscopy with ISOLTRAP.* Nucl. Instrum. Methods Phys. Res. A **689** (2012) 102–107. URL `http://dx.doi.org/10.1016/j.nima.2012.04.059`.

[106] M. Kowalska et al. *Preparing a journey to the east of* ^{208}*Pb with ISOLTRAP: Isobaric purification at* $A = 209$ *and new masses for* $^{211\text{-}213}$*Fr and* ^{211}*Ra.* Eur. Phys. J. A **42** (2009) 351–359. URL `http://dx.doi.org/10.1140/epja/i2009-10835-1`.

[107] D. Beck et al. *A new control system for ISOLTRAP.* Nucl. Instrum. Methods Phys. Res. A **527** (2004) 567–579. URL `http://dx.doi.org/DOI:10.1016/j.nima.2004.02.043`.

[108] CS Framework Homepage (2012). URL `http://wiki.gsi.de/cgi-bin/view/CSframework/`.

[109] GNU Homepage (2012). URL `http://www.gnu.org/licenses/`.

[110] J. Ketelaer et al. *TRIGA-SPEC: A setup for mass spectrometry and laser spectroscopy at the research reactor TRIGA Mainz.* Nucl. Instrum. Methods Phys. Res. A **594** (2008) 162–177. URL `http://dx.doi.org/10.1016/j.nima.2008.06.023`.

[111] M. Tandecki et al. *Computer controls for the WITCH experiment.* Nucl. Instrum. Methods Phys. Res. A **629** (2011) 396–405. URL `http://dx.doi.org/10.1016/j.nima.2010.10.111`.

[112] G. Maero et al. *Numerical investigations on resistive cooling of trapped highly charged ions.* Appl. Phys. B: Lasers Opt. **107** (2012) 1087–1096. URL `http://dx.doi.org/10.1007/s00340-011-4808-5`.

[113] V. Bagnoud et al. *Commissioning and early experiments of the PHELIX facility.* Appl. Phys. B: Lasers Opt. **100** (2010) 137–150. URL `http://dx.doi.org/10.1007/s00340-009-3855-7`.

[114] C. Gaspar and M. Dönszelmann. *DIM : a distributed information management system for the DELPHI experiment at CERN.* In: D. A. Axen and R. Poutissou (eds.), *Proceedings of the 8th Conference on Real-Time Computer applications in Nuclear, Particle and Plasma Physics*, 156–158. Vancouver, Canada (1993). URL `http://cdsweb.cern.ch/record/254799`.

[115] C. Gaspar, M. Dönszelmann, and P. Charpentier. *DIM, a portable, light weight package for information publishing, data transfer and inter-process communication.* Comput. Phys. Commun. **140** (2001) 102–109. URL `http://dx.doi.org/10.1016/S0010-4655(01)00260-0`.

[116] The ALICE Collaboration et al. *The ALICE experiment at the CERN LHC.* JINST **3** (2008) S08002. URL `http://dx.doi.org/10.1088/1748-0221/3/08/S08002`.

[117] The LHCb Collaboration et al. *The LHCb Detector at the LHC.* JINST **3** (2008) S08005. URL `http://dx.doi.org/10.1088/1748-0221/3/08/S08005`.

[118] D. Beck, H. Brand, and N. Kurz. *Die LabVIEW-DIM Schnittstelle: Das Tor zur standardisierten Kommunikation zwischen LabVIEW und einer Vielfalt von*

Programmiersprachen und Betriebssystemen. In: R. Jamal and H. Jaschinski (eds.), *Proc. "Virtuelle Instrumente in der Praxis 2005"*, 20–26. Fürstenfeldbruck, Germany (2005). URL `http://wiki.gsi.de/cgi-bin/view/CSframework/CSDocuments`. ISBN 3-7785-2947-1.

[119] LabVIEW-DIM Interface Homepage (2012). URL `http://wiki.gsi.de/cgi-bin/view/CSframework/LVDimInterface`.

[120] LabVIEW Homepage (2012). URL `http://www.ni.com/labview`.

[121] DMS Homepage (2012). URL `http://wiki.gsi.de/cgi-bin/view/CSframework/DomainManagementSystem`.

[122] Nodemon Homepage (2012). URL `http://wiki.gsi.de/cgi-bin/view/CSframework/NodeMon`.

[123] SQLServer Homepage (2012). URL `http://wiki.gsi.de/cgi-bin/view/CSframework/CSSqlServer`.

[124] C. Yazidjian et al. *Commissioning and first on-line test of the new ISOLTRAP control system.* Eur. Phys. J. A **25** (2005) 67–68. URL `http://dx.doi.org/10.1140/epjad/i2005-06-096-x`.

[125] D. H. Beck et al. *A Pulse-Pattern Generator Using LabVIEW FPGA.* In: *Proceedings of ICALEPCS2009*, 215–217. Kobe, Japan (2009). URL `http://epaper.kek.jp/icalepcs2009/papers/tup058.pdf`. ISBN 978-4-9905391-0-8.

[126] F. Ziegler et al. *A new Pulse-Pattern Generator based on LabVIEW FPGA.* Nucl. Instrum. Methods Phys. Res. A **679** (2012) 1–6. URL `http://dx.doi.org/10.1016/j.nima.2012.03.010`.

[127] R. N. Wolf et al. *In preparation* (2012).

[128] I. Deloose. *New management system for NICE.* CERN Computer Newsletter No. 2006-003 (2006). URL `http://cerncourier.com/cws/article/cnl/25028`.

[129] S. Lüders. *Update on the CERN Computing and Network Infrastructure for Control (CNIC).* In: *Proceedings of ICALEPCS07*. Knoxville, Tennessee, USA (2007). URL `http://accelconf.web.cern.ch/accelconf/ica07/PAPERS/WPPB38.PDF`.

[130] Subversion Homepage (2012). URL `http://subversion.apache.org/`.

[131] D. Beck et al. *Einsatz von FPGAs bei LabVIEW basierten Experimentsteuerungen.* In: F. Wulf (ed.), *Bericht der Frühjahrstagung der Studiengruppe für Elektronische Instrumentierung*. Helmholtz-Zentrum Berlin für Materialien und Energie GmbH, Berlin (2009). URL `http://www.helmholtz-berlin.de/media/media/spezial/events/sei/FZJ09/beck_fzj09.pdf`.

[132] D. Beck. *Massenbestimmung instabiler Isotope der Seltenen Erden um 146 Gd mit dem ISOLTRAP-Spektrometer.* Ph.D. thesis, Johannes Gutenberg-Universität, Mainz, Germany (1997).

[133] T. Eronen. *High precision QEC value measurements of superallowed 0+ ! 0+ beta decays with JYFLTRAP.* Ph.D. thesis, University of Jyväskylä, Finland (2008). URL `http://urn.fi/URN:ISBN:978-951-39-3405-7`.

[134] S. Ettenauer. *First mass measurements of highly charged, short-lived nuclides in a Penning trap and the mass of Rb-74.* Ph.D. thesis, University of British Columbia, Canada (2012). URL `http://hdl.handle.net/2429/42333`.

[135] G. Bollen et al. *Resolution of nuclear ground and isomeric states by a Penning trap mass spectrometer.* Phys. Rev. C **46** (1992) R2140–R2143. URL `http://dx.doi.org/10.1103/PhysRevC.46.R2140`.

[136] A. Kellerbauer. *A Study of the Accuray of the Penning Trap Mass Spectrometer ISOLTRAP and Standard-Model Tests With Superallowed Beta Decays.* Ph.D. thesis, Ruprecht-Karls-Universität Heidelberg, Germany (2002).

[137] A. Kellerbauer et al. *From direct to absolute mass measurements: A study of the accuracy of ISOLTRAP.* Eur. Phys. J. D **22** (2003) 53–64. URL `http://dx.doi.org/10.1140/epjd/e2002-00222-0`.

[138] P. W. Anderson. *Theory of Flux Creep in Hard Superconductors.* Phys. Rev. Lett. **9** (1962) 309–311. URL `http://dx.doi.org/10.1103/PhysRevLett.9.309`.

[139] P. W. Anderson and Y. B. Kim. *Hard Superconductivity: Theory of the Motion of Abrikosov Flux Lines.* Rev. Mod. Phys. **36** (1964) 39–43. URL `http://dx.doi.org/10.1103/RevModPhys.36.39`.

[140] R. J. Barlow. *Statistics: A Guide to the Use of Statistical Methods in the Physical Sciences (Manchester Physics Series).* John Wiley & Sons Ltd (1989).

[141] A. T. Gallant et al. *Highly charged ions in Penning traps: A new tool for resolving low-lying isomeric states.* Phys. Rev. C **85** (2012) 044311. URL `http://dx.doi.org/10.1103/PhysRevC.85.044311`.

[142] K. Nakamura and Particle Data Group. *Review of Particle Physics.* J. Phys. G: Nucl. Part. Phys. **37** (2010) 075021. URL `http://dx.doi.org/10.1088/0954-3899/37/7A/075021`.

[143] GNU Octave Homepage (2012). URL `http://www.gnu.org/software/octave/`.

[144] A. H. Wapstra, G. Audi, and C. Thibault. *The AME2003 atomic mass evaluation: (I). Evaluation of input data, adjustment procedures.* Nucl. Phys. A **729** (2003) 129–336. URL `http://dx.doi.org/10.1016/j.nuclphysa.2003.11.002`.

[145] D. Beck et al. *Accurate masses of unstable rare-earth isotopes by ISOLTRAP.* Eur. Phys. J. A **8** (2000) 307–329. URL `http://dx.doi.org/10.1007/s100500070085`.

[146] G. Audi and W. Meng. Private Communication (2009).

[147] G. Audi and W. Meng. Private Communication (2012).

[148] K.-L. Kratz et al. *Nuclear structure studies at ISOLDE and their impact on the astrophysical r-process.* Hyperfine Interact. **129** (2000) 185–221. URL `http://dx.doi.org/10.1023/A:1012694723985`.

[149] B. Sun et al. *Nuclear structure studies of short-lived neutron-rich nuclei with the novel large-scale isochronous mass spectrometry at the FRS-ESR facility.* Nucl. Phys. A **812** (2008) 1–12. URL `http://dx.doi.org/10.1016/j.nuclphysa.2008.08.013`.

[150] K. Valli, E. K. Hyde, and W. Treytl. *Alpha decay of neutron-deficient francium isotopes.* J. Inorg. Nucl. Chem. **29** (1967) 2503–2514. URL `http://dx.doi.org/10.1016/0022-1902(67)80176-3`.

[151] P. Hornshøj, P. G. Hansen, and B. Jonson. *Alpha-decay widths of neutron-deficient francium and astatine isotopes.* Nucl. Phys. A **230** (1974) 380–392. URL `http://dx.doi.org/10.1016/0375-9474(74)90144-4`.

[152] B. G. Ritchie et al. *Alpha-decay properties of* ^{205,206,207,208}Fr*: Identification of* ^{206}Fr^{m}. Phys. Rev. C **23** (1981) 2342–2344. URL `http://dx.doi.org/10.1103/PhysRevC.23.2342`.

[153] M. Epherre et al. *Direct mass measurements on francium isotopes and deduced masses for odd-z neighbouring elements.* Nucl. Phys. A **340** (1980) 1–12. URL `http://dx.doi.org/10.1016/0375-9474(80)90319-X`.

[154] G. Audi et al. *Masses of Rb, Cs and Fr isotopes.* Nucl. Phys. A **378** (1982) 443–460. URL `http://dx.doi.org/10.1016/0375-9474(82)90459-6`.

[155] B. Grennberg and A. Rytz. *Absolute Measurements of α-ray Energies.* Metrologia **7** (1971) 65. URL `http://dx.doi.org/10.1088/0026-1394/7/2/005`.

[156] E. Rapisarda. Private Communication (2012).

[157] K. S. Toth et al. *Observation of α-decay in thallium nuclei, including the new isotopes 184Tl and 185Tl.* Phys. Lett. B **63** (1976) 150–153. URL `http://dx.doi.org/10.1016/0370-2693(76)90636-5`.

[158] U. J. Schrewe et al. *Alpha decay of neutron-deficient isotopes with $78 \leq Z \leq 83$ including the new isotopes 183, 184Pb and 188Bi.* Phys. Lett. B **91** (1980) 46–50. URL `http://dx.doi.org/10.1016/0370-2693(80)90659-0`.

[159] P. Van Duppen et al. *Intruder states in odd-odd Tl nuclei populated in the α-decay of odd-odd Bi isotopes.* Nucl. Phys. A **529** (1991) 268–288. URL `http://dx.doi.org/10.1016/0375-9474(91)90796-9`.

[160] C. Weber et al. *Atomic mass measurements of short-lived nuclides around the doubly-magic 208Pb.* Nucl. Phys. A **803** (2008) 1–29. URL `http://dx.doi.org/10.1016/j.nuclphysa.2007.12.014`.

[161] J. Stanja. Ph.D. thesis, Technische Universität Dresden (2012). In preparation.

[162] T. Radon et al. *Schottky mass measurements of stored and cooled neutron-deficient projectile fragments in the element range of* $57 \leq Z \leq 84$. Nucl. Phys. A **677** (2000) 75–99. URL `http://dx.doi.org/10.1016/S0375-9474(00)00304-3`.

[163] G. Audi et al. *Atomic Mass Evaluation: the Mass Tables.* J. Korean Phys. Soc. **59** (2011) 1318–1321. URL `http://dx.doi.org/10.3938/jkps.59.1318`.

[164] J. Dobaczewski et al. *Odd-even staggering of binding energies as a consequence of pairing and mean-field effects.* Phys. Rev. C **63** (2001) 024308. URL `http://dx.doi.org/10.1103/PhysRevC.63.024308`.

[165] J. Hakala et al. *Precision Mass Measurements beyond* ^{132}Sn*: Anomalous Behavior of Odd-Even Staggering of Binding Energies.* Phys. Rev. Lett. **109** (2012) 032501. URL `http://dx.doi.org/10.1103/PhysRevLett.109.032501`.

[166] T. Kühl et al. *Nuclear Shape Staggering in Very Neutron-Deficient Hg Isotopes Detected by Laser Spectroscopy.* Phys. Rev. Lett. **39** (1977) 180–183. URL `http://dx.doi.org/10.1103/PhysRevLett.39.180`.

[167] Ch. Böhm. Ph.D. thesis, Ruprecht-Karls-Universität, Heidelberg, Germany (2013). In preparation.

[168] J. Billowes et al. *Collinear resonant ionization laser spectroscopy of rare francium isotopes.* Proposal to the INTC. CERN-INTC-2008-010. INTC-P-240, CERN, Geneva (2008). URL `http://cdsweb.cern.ch/record/1080361`.

[169] K. T. Flanagan et al. *Collinear resonant ionization laser spectroscopy of rare francium isotopes: IS471.* Status report to the INTC. CERN-INTC-2012-021. INTC-SR-024, CERN, Geneva (2012). URL `http://cdsweb.cern.ch/record/1411597`.

[170] T. Procter. Ph.D. thesis, University of Manchester, United Kingdom (2013). In preparation.

[171] K. Lynch. Ph.D. thesis, University of Manchester, United Kingdom (2013). In preparation.

[172] A. Andreyev et al. *Shape coexistence in the lightest Tl isotopes studied by laser spectroscopy.* Proposal to the INTC. CERN-INTC-2011-005. INTC-P-291, CERN, Geneva (2011). URL `http://cdsweb.cern.ch/record/1319031`.

[173] S. Schwarz. Private Communication (2012).

[174] R. N. Wolf et al. *On-line separation of short-lived nuclei by a multi-reflection time-of-flight device.* Nucl. Instrum. Methods Phys. Res. A **686** (2012) 82–90. URL `http://dx.doi.org/10.1016/j.nima.2012.05.067`.

Own Publications

The following articles have been published in the framework of this thesis.

[1] *Surveying the $N = 40$ island of inversion with new manganese masses.*
S. Naimi, G. Audi, D. Beck, K. Blaum, Ch. Böhm, Ch. Borgmann, M. Breitenfeldt, S. George, F. Herfurth, A. Herlert, A. Kellerbauer, M. Kowalska, D. Lunney, E. Minaya Ramirez, D. Neidherr, M. Rosenbusch, L. Schweikhard, R. N. Wolf, and K. Zuber.
Phys. Rev. C **86** (2012) 014325.
URL `http://dx.doi.org/10.1103/PhysRevC.86.014325`.

[2] *Buffer-gas-free mass-selective ion centering in Penning traps by simultaneous dipolar excitation of magnetron motion and quadrupolar excitation for interconversion between magnetron and cyclotron motion.*
M. Rosenbusch, K. Blaum, Ch. Borgmann, S. Kreim, M. Kretzschmar, D. Lunney, L. Schweikhard, F. Wienholtz, and R. N. Wolf.
Int. J. Mass Spectrom. **325–327** (2012) 51–57.
URL `http://dx.doi.org/10.1016/j.ijms.2012.06.008`.

[3] *Trap-assisted decay spectroscopy with ISOLTRAP.*
M. Kowalska, S. Naimi, J. Agramunt, A. Algora, D. Beck, B. Blank, K. Blaum, Ch. Böhm, Ch. Borgmann, M. Breitenfeldt, L. M. Fraile, S. George, F. Herfurth, A. Herlert, S. Kreim, D. Lunney, E. Minaya-Ramirez, D. Neidherr, M. Rosenbusch, B. Rubio, L. Schweikhard, J. Stanja, and K. Zuber.
Nucl. Instrum. Methods Phys. Res. A **689** (2012) 102–107.
URL `http://dx.doi.org/10.1016/j.nima.2012.04.059`.

[4] *On-line separation of short-lived nuclei by a multi-reflection time-of-flight device.*
R. N. Wolf, D. Beck, K. Blaum, Ch. Böhm, Ch. Borgmann, M. Breitenfeldt, F. Herfurth, A. Herlert, M. Kowalska, S. Kreim, D. Lunney, S. Naimi, D. Neidherr, M. Rosenbusch, L. Schweikhard, J. Stanja, F. Wienholtz, and K. Zuber.
Nucl. Instrum. Methods Phys. Res. A **686** (2012) 82–90.
URL `http://dx.doi.org/10.1016/j.nima.2012.05.067`.

[5] *Q Value and Half-Lives for the Double-β-Decay Nuclide* ^{110}Pd.
D. Fink, J. Barea, D. Beck, K. Blaum, Ch. Böhm, Ch. Borgmann, M. Breitenfeldt, F. Herfurth, A. Herlert, J. Kotila, M. Kowalska, S. Kreim, D. Lunney, S. Naimi, M. Rosenbusch, S. Schwarz, L. Schweikhard, F. Šimkovic, J. Stanja, and K. Zuber.
Phys. Rev. Lett. **108** (2012) 062502.
URL `http://dx.doi.org/10.1103/PhysRevLett.108.062502`.

[6] *A study of octupolar excitation for mass-selective centering in Penning traps.*
M. Rosenbusch, Ch. Böhm, Ch. Borgmann, M. Breitenfeldt, A. Herlert, M. Kowalska, S. Kreim, G. Marx, S. Naimi, D. Neidherr, R. Schneider, and L. Schweikhard.
Int. J. Mass Spectrom. **314** (2012) 6–12.
URL `http://dx.doi.org/10.1016/j.ijms.2012.01.002`.

[7] *Cadmium mass measurements between the neutron shell closures at $N = 50$ and 82.*
Ch. Borgmann, M. Breitenfeldt, G. Audi, S. Baruah, D. Beck, K. Blaum, Ch. Böhm, R. B. Cakirli, R. F. Casten, P. Delahaye, M. Dworschak, S. George, F. Herfurth, A. Herlert, A. Kellerbauer, M. Kowalska, S. Kreim, D. Lunney, E. Minaya-Ramirez, S. Naimi, D. Neidherr, M. Rosenbusch, R. Savreux, S. Schwarz, L. Schweikhard, and C. Yazidjian.
AIP Conf. Proc. **1377** (2011) 332–334.
URL `http://dx.doi.org/10.1063/1.3628403`.

[8] *Mass measurements of short-lived nuclides using the ISOLTRAP preparation Penning trap.*
S. Naimi, M. Rosenbusch, G. Audi, K. Blaum, Ch. Böhm, Ch. Borgmann, M. Breitenfeldt, S. George, F. Herfurth, A. Herlert, M. Kowalska, S. Kreim, D. Lunney, E. Minaya-Ramirez, D. Neidherr, L. Schweikhard, and M. Wang.
Hyperfine Interact. **199** (2011) 231–240.
URL `http://dx.doi.org/10.1007/s10751-011-0318-4`.

[9] *Effects of space charge on the mass purification in Penning traps.*
A. Herlert, Ch. Borgmann, D. Fink, Ch. Holm Christensen, M. Kowalska, and S. Naimi.
Hyperfine Interact. **199** (2011) 211–220.
URL `http://dx.doi.org/10.1007/s10751-011-0316-6`.

[10] *Nuclear structure studies with the ISOLTRAP Penning trap mass spectrometer.*
Ch. Borgmann, G. Audi, D. Beck, K. Blaum, Ch. Böhm, M. Breitenfeldt, R. B. Cakirli, R. F. Casten, S. Eliseev, D. Fink, S. George, F. Herfurth, A. Herlert, A. Kellerbauer, H.-J. Kluge, M. Kowalska, S. Kreim, D. Lunney, E. Minaya-Ramirez, S. Naimi, D. Neidherr, Yu. Novikov, M. Rosenbusch, S. Schwarz, L. Schweikhard, and K. Zuber.
In: K. Große (ed.), *GSI Scientific Report 2009.* GSI Helmholtzzentrum für Schwerionenforschung GmbH, Darmstadt, Germany (2010).

[11] *Critical-Point Boundary for the Nuclear Quantum Phase Transition Near $A = 100$ from Mass Measurements of* ^{96,97}Kr.
S. Naimi, G. Audi, D. Beck, K. Blaum, Ch. Böhm, Ch. Borgmann, M. Breitenfeldt, S. George, F. Herfurth, A. Herlert, M. Kowalska, S. Kreim, D. Lunney, D. Neidherr, M. Rosenbusch, S. Schwarz, L. Schweikhard, and K. Zuber.
Phys. Rev. Lett. **105** (2010) 032502.
URL `http://dx.doi.org/10.1103/PhysRevLett.105.032502`.

[12] *Approaching the $N = 82$ shell closure with mass measurements of Ag and Cd isotopes.*
M. Breitenfeldt, Ch. Borgmann, G. Audi, S. Baruah, D. Beck, K. Blaum, Ch. Böhm, R. B. Cakirli, R. F. Casten, P. Delahaye, M. Dworschak, S. George, F. Herfurth, A. Herlert, A. Kellerbauer, M. Kowalska, D. Lunney, E. Minaya-Ramirez, S. Naimi, D. Neidherr, M. Rosenbusch, R. Savreux, S. Schwarz, L. Schweikhard, and C. Yazidjian.
Phys. Rev. C **81** (2010) 034313.
URL `http://dx.doi.org/10.1103/PhysRevC.81.034313`.

[13] *ISOLTRAP results 2006–2009.*
M. Kowalska for the ISOLTRAP Collaboration.
Hyperfine Interact. **196** (2010) 199–203.
URL `http://dx.doi.org/10.1007/s10751-009-0140-4`.

[14] *Neutron Drip-Line Topography.*
E. Minaya Ramirez, G. Audi, D. Beck, K. Blaum, Ch. Böhm, Ch. Borgmann, M. Breitenfeldt, N. Chamel, S. George, S. Goriely, F. Herfurth, A. Herlert, A. Kellerbauer, M. Kowalska, D. Lunney, S. Naimi, D. Neidherr, J. M. Pearson, M. Rosenbusch, S. Schwarz, and L. Schweikhard.
AIP Conf. Proc. **1165** (2009) 94–97.
URL `http://dx.doi.org/10.1063/1.3232162`.

Acknowledgments

On my arrival at CERN, I did not plan to stay for more than six month. The fact that I did was due to several nice people I met and who supported me during the last years. Therefore, I would like to take the opportunity to thank them:

First of all, I would like to thank my supervisor Klaus Blaum for offering me the possibility to come to (and stay at) such a great place and for his constant support and advice during the whole time, although Heidelberg is not just around the corner.

Furthermore, thanks to Susanne Kreim for her continuous support, many fruitful discussions, a lot of good suggestions and valuable comments on the manuscript. Thanks as well for the numerous invitations (thanks also to Kim) and the nice atmosphere. It was nice working with you!

I would like to thank the ISOLTRAP collaboration for supporting the experiment. Thanks to the "old" ISOLTRAP team consisting of Dennis Neidherr, Sarah Naimi, Martin Breitenfeldt, Alexander Herlert, and Magda Kowalska for introducing me to the experiment and teaching me how to operate it. Thanks as well to the "current" ISOLTRAP crew consisting of Susanne Kreim, Frank Wienholtz (aka François Viennebois), Vladimir Manea, Marco Rosenbusch, and Robert Wolf for the discussions, the nice time in the lab, and the breaks in between. Furthermore, I would like to thank Thomas Cocolios, Juliane Stanja, and Magda Kowalska for many discussions about the decay-spectroscopy results. Thanks to Christine Böhm: For many interesting discussion (not only work related), the really quick responses in the final stage of this thesis and the warm and friendly atmosphere she creates around her.

Thanks to Dietrich Beck and Holger Brand for introducing me into the mysterious world of the CS framework. I learned a lot!

I would like to thank Georges Audi, Meng Wang, and Dave Lunney for the possibility to come to Paris to discuss the data and for explaining the secrets of the AME to me.

Thanks to Yorick Blumenfeld and the whole ISOLDE group as well as the technical team for all their efforts to keep ISOLDE online! Thanks to Henry Stroke for proofreading parts of the manuscript.

Silke: Ich habe verzweifelt nach passenden Worten des Dankes gesucht, aber ich befürchte, es gibt sie einfach nicht, nicht einmal auf Deutsch. Danke für alles!

Abschließend danke ich meinen Eltern: Danke für eure Mühen und eure Unterstützung zu jeder Zeit!